EXEP3D

TALLINNA TEHNIKAKÕRGKOOL
TTK UNIVERSITY OF APPLIED SCIENCES

TECHNISCHE UNIVERSITÄT DRESDEN

TU/e EINDHOVEN UNIVERSITY OF TECHNOLOGY

ABSTRACT

This Deliverable 2.1, prepared under Work Package 2 (*Knowledge Exchange and Innovation Transfer*) of the EXEP3D project, presents the outcomes of hands-on knowledge transfer in 3D concrete printing formwork, process control, and quality assurance carried out through staff study visits, seminars, and training activities coordinated by TU/e. It consolidates the content and results of these activities into structured teaching materials on 3DCP formwork and related methods.

Author

Eindhoven University of Technology (TU/e)

DELIVERABLE REPORT

WP2 – D2.1

Teaching Materials on Minimum Formwork using 3DCP

This project has received funding from the European Union's Horizon Europe research and innovation programme under Grant Agreement No. 101158492 — EXEP3D — HORIZON-WIDERA-2023-ACCESS-02.

Delivery Title:	Teaching Materials on Minimum Formwork using 3DCP
Delivery Number:	D2.1
Lead beneficiary:	Eindhoven University of Technology (TU/e)
Type:	Report
Work Package Title:	Knowledge Exchange and Innovation Transfer
Work Package Number:	WP2
Dissemination level:	Public
Due Date:	31 December 2025

Revision History:

Version	Date	Author (Partner)	Remarks
Draft v0.1	09/12/2025	Lauri Hass (TU/e) Karsten Nefs (TU/e)	First draft
v0.2	28/12/2025	Lauri Hass (TU/e) Karsten Nefs (TU/e)	Revised structure and figures

Contents

Preface

About the EXEP3D Project and Twinning Partners

The EXEP3D project — Innovation Excellence in Construction Engineering: Novel 3D Concrete Printing Technologies and Sustainable Mixtures — is a Horizon Europe Twinning initiative (Grant Agreement No. 101158492, Call: HORIZON-WIDERA-2023-ACCESS-02-01). The project aims to strengthen scientific excellence, innovation transfer, and research management capacity in the field of construction engineering through focused collaboration on 3D concrete printing (3DCP).

Led by Tallinn University of Applied Sciences (TTK UAS, Estonia) in partnership with Technische Universiteit Eindhoven (TU/e, Netherlands) and Technische Universität Dresden (TUD, Germany), the three-year initiative focuses on enhancing skills, knowledge, and research infrastructure to position TTK as a leading competence centre for 3D concrete printing and printable mixtures in Estonia and Eastern Europe.

The Twinning collaboration combines complementary expertise: TU/e's world-class research and facilities on 3D concrete printing formwork and robotic production, TUD's advanced competence in printable mixtures and digital concrete, and TTK's strong applied research base and industrial outreach in the Estonian construction sector. Together, the partners form a strategic link between widening and advanced countries, accelerating knowledge transfer, strengthening applied research capacity, and promoting innovation in sustainable and automated concrete construction across Europe.

Purpose of this teaching material

This teaching material has been developed within Work Package 2 — Knowledge Exchange and Innovation Transfer — of the EXEP3D project. It serves as both a training and reference resource for students, researchers, and professionals interested in 3D concrete printing and its role in sustainable construction.

The content consolidates the knowledge and experiences gained through staff study visits, joint seminars, research workshops, and pilot studies among the Twinning partners. It aligns with the project's capacity-building objectives by providing structured, open-access material to support future teaching, experimentation, and research in digital and low-carbon concrete construction.

A central research theme within EXEP3D is the development of *minimum formwork* concepts enabled by 3D Concrete Printing (3DCP). In this context, "minimum" refers not only to reducing the volume of conventional formwork but also to streamlining production processes, improving material efficiency, and enabling geometries that support structural optimisation. This teaching material introduces the foundational principles of 3DCP with a particular emphasis on how digital fabrication can contribute to such minimum-formwork construction approaches.

The content is organised around the core topics necessary to understand 3DCP as

both a material process and a design methodology. These include: the motivation for digital construction; the behaviour of cementitious materials during printing; fresh-state and hardened-state characterisation; digital workflows and modelling tools; and reinforcement strategies suitable for printed or printed-cast hybrid systems. The selected case studies further illustrate how these methods are applied in real projects.

The learning objectives are therefore aligned with these themes:

- Understanding the fundamentals and motivation of 3D concrete printing within the broader context of digital construction.
- Recognising how process parameters and material behaviour interact during printing, and how these influence fresh-state and hardened-state performance.
- Becoming familiar with experimental methods for characterising printable materials and understanding their relevance for quality control.
- Exploring digital design tools, early-age modelling approaches, and workflows used to generate printable geometries and minimum-formwork elements.
- Identifying the different reinforcement strategies compatible with 3DCP, including post-installed, pre-installed, and process-integrated solutions.
- Examining realised projects to understand practical implementation, design decision-making, and lessons learned.

Through this structure, the teaching material contributes to the broader goal of EXEP3D: strengthening capacity in automated, knowledge-driven construction by translating research developments in 3D concrete printing into accessible educational resources.

The authors of this teaching material aim to consistently acknowledge and reference the original research on which it builds. This document serves solely as a vehicle for disseminating existing knowledge and insights, and does not claim authorship of the underlying work.

Structure of the Teaching Materials

The teaching material is organized into 4 main chapters, illustrated on Figure 1, that together provide an overview of 3D Concrete Printing (3DCP) and its application to *minimum formwork* strategies. Each chapter tries to combine theoretical content with laboratory-oriented modules that guide the learner from fundamental principles to applied experimentation and system-level understanding.

Chapters 1–2: Introduction to 3D Concrete Printing and Material Foundations. Chapters 1 and 2 introduce the broader context and material basis of 3D Concrete Printing. Chapter 1 outlines the motivation for digital construction with cementitious materials, linking 3DCP to challenges in productivity, labour, and embodied emissions. It explains why concrete remains a central construction material, discusses

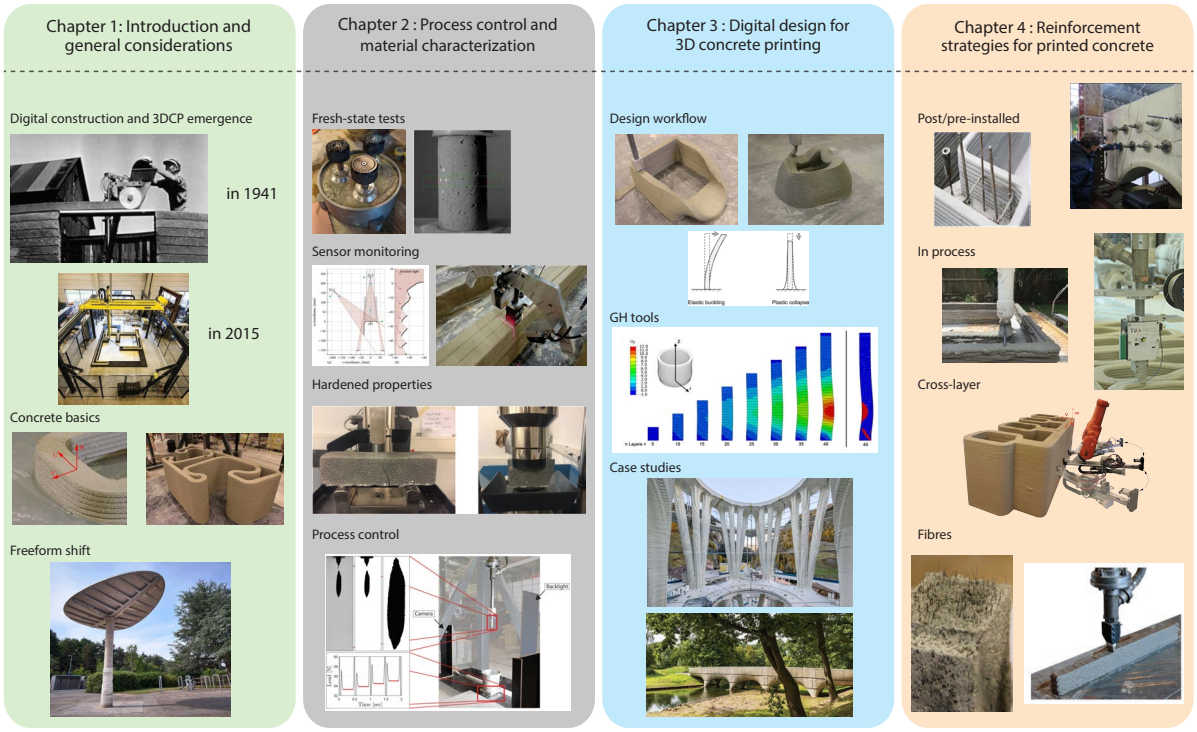

Figure 1: Overview of the teaching material layout.

the environmental implications of cement production, and highlights how digital fabrication can improve material efficiency by reducing formwork use and enabling geometry that follows structural demand. The chapter concludes with an overview of key digital fabrication methods with concrete, with extrusion-based 3DCP as the main focus.

Chapter 2 shifts to the material and process perspective, addressing how printable concretes behave throughout the 3DCP workflow. It introduces the concept of first-time-right manufacturing and describes the main stages of mixing, pumping, extrusion, and early-age build-up, emphasising how temporal, spatial, and thermal variations influence print quality. The chapter presents essential fresh-state properties (such as yield stress, thixotropy, pumpability and buildability) and outlines representative test methods for both fresh and hardened states, including process monitoring techniques that link material behaviour to printing conditions. Together, these chapters provide the conceptual and experimental foundations needed for the subsequent chapters on digital design, process modelling, reinforcement strategies, and realised projects.

Chapters 3–4: Digital Design Workflows and Reinforcement Strategies for 3DCP. Chapter 3 introduces digital design for 3D concrete printing, focusing on how parametric and rule-based modelling workflows translate design intent into printable geometries and fabrication data. It outlines the shift from formwork-driven to print-driven design, discusses the implications of geometric freedom for cost and complexity, and presents Rhinoceros + Grasshopper as the central modelling environment. Within this framework, plug-ins such as Salad Slicer, Robot Components, and Karamba3D are introduced to illustrate how slicing, robot path generation, and ba-

sic structural analysis can be integrated into a single workflow. The chapter concludes with a series of realised projects—including the Gemert and Nijmegen bridges, Project Milestone, Tor Alva, and the Canopy—that exemplify different design strategies and practical applications of 3DCP.

Chapter 4 focuses on reinforcement strategies for printed concrete and the challenges of combining layered fabrication with structural requirements. It introduces the main categories of reinforcement concepts—post-installed, pre-installed, and process-integrated techniques—and discusses their respective advantages, limitations, and Technology Readiness Levels. Particular attention is given to anisotropy, multi-directional reinforcement needs, and the interaction between reinforcement systems and thin-walled printed geometries. Examples such as helical (screw-type) reinforcement combined with strain-hardening cementitious composites (SHCC) or plain mortar highlight how bond, confinement, and material choice govern structural performance. Together, these chapters link digital design workflows to the emerging toolbox of reinforcement strategies needed for structurally efficient printed and printed–cast hybrid systems.

Declaration on the use of AI-assisted technologies
During the preparation of this work, the authors used ChatGPT and related AI-assisted proofreading tools to improve the readability of the text by correcting grammar and spelling. These tools were employed exclusively to enhance clarity and linguistic consistency; no new scientific content or data were generated through their use. The authors have carefully reviewed and edited all resulting material and take full responsibility for the integrity, accuracy, and originality of the final text.

Acknowledgements

The authors gratefully acknowledge the financial support of the European Union's Horizon Europe research and innovation programme under Grant Agreement No. 101158492 — EXEP3D — HORIZON-WIDERA-2023-ACCESS-02.

Sincere thanks are extended to the academic and administrative staff, researchers, and students of the partner institutions for their active participation in study visits, seminars, and joint research activities that provided the foundation for this material. Their dedication to advancing excellence in construction engineering and digital concrete fabrication has been instrumental in the preparation of this publication.

The authors also wish to express their appreciation to the 3D Concrete Printing Group at Eindhoven University of Technology (TU/e), whose extensive body of research underpins the concepts, methods, and examples presented throughout these chapters. The material draws broadly on the group's collective work in fresh- and hardened-state characterisation, digital design, reinforcement development, and modelling strategies. In particular, advances in process monitoring and quality control—led by Derk Bos and Jelle Versteege—form a crucial foundation for the discussions on first-time-right manufacturing and process reliability presented in this material. Specific developments such as the Grasshopper plug-ins *Robot Components* and related digital fabrication tools have been made possible through the software development of Arjen Deetman and have significantly enriched the

design workflows introduced here.

The authors further express their gratitude to Theo Salet, Rob Wolfs, and Sandra Lucas for their continuous guidance, support, and commitment to advancing the field of 3D concrete printing at TU/e. Special acknowledgement is also given to the Structural Engineering and Design (SED) laboratory for providing the technical facilities and collaborative environment that have enabled both research progress and the preparation of this teaching material.

Finally, the authors gratefully acknowledge the broader international 3D printing research community—across academia and industry—whose pioneering studies, open knowledge exchange, and practical innovations form an essential foundation for the work referenced throughout this material. Their collective contributions continue to drive progress in digital concrete fabrication and inspire ongoing collaboration and innovation.

Chapter 1

Introduction and General Considerations

1.1 Motivation for Digital Construction

Buildings, infrastructure, and urban systems define modern life, and their scale is growing rapidly. Global floor area is expected to double by 2060, adding more than 230 billion m^2 of new buildings [1]. The construction sector already represents around 9 % of the EU GDP and employs over 18 million people, yet faces persistent challenges: stagnant productivity, labour shortages, and tightening environmental regulations [2, 1]. Demographic growth further amplifies these pressures—Africa's population alone is projected to triple by 2100, requiring massive investments in housing, transport, and energy infrastructure [3].

Despite its economic significance, construction remains one of the least productive industries. Global productivity has risen only 0.4 % annually over the past two decades—compared to about 3 % in manufacturing [4]. Each project effectively rebuilds its own temporary production setup, limiting learning, automation, and standardization. In contrast, manufacturing achieves scale and efficiency through repeatable, feedback-controlled processes (Figure 1.1).

At the same time, the sector's environmental footprint is immense. Construction accounts for roughly 36 % of global energy-related CO_2 emissions, while cement production alone contributes about 7 % [2]. These pressures make the transformation toward low-carbon and resource-efficient construction unavoidable.

Digital and automated fabrication offer a way forward. By connecting design directly to production, digital construction methods integrate material behaviour, robotic control, and data feedback in one workflow. They promise higher productivity, reduced waste, and new opportunities for material efficiency. The following sections outline how these technologies—particularly digital fabrication with concrete (DFC) and 3D concrete printing (3DCP)—are reshaping the way we build.

Figure 1.1: Manufacturing has transformed production into a controlled industrial process, whereas construction still relies on temporary, project-based workflows that must be set up anew for each site. Images from [5, 6]

1.2 Emergence of 3D Concrete Printing

3D Concrete Printing (3DCP) has become the most developed and widely adopted branch of Digital Fabrication with Concrete (DFC)—a family of automated methods in which cementitious materials are deposited layer by layer under digital control [7, 8]. The process replaces traditional casting in formwork with direct material placement along prescribed toolpaths, merging design, material, and production into a single data-driven workflow.

Extrusion-based 3DCP relies on three interlinked subsystems: (i) a mechanical system—robotic arm or gantry—that controls nozzle position; (ii) a material system for mixing, pumping, and extrusion; and (iii) a digital control system managing slicing, toolpaths, and process feedback [9]. Printable materials are fine-grained mortars with tailored rheology: fluid enough to pump yet stiff enough to retain their shape immediately after deposition. Both single-component (1K) and dual-component (2K) systems exist, with 2K methods adding an accelerator near the printhead for rapid setting.

Historically, 3DCP evolved from early research in the 1990s—Pegna's *Solid Freeform Construction*, Khoshnevis's *Contour Crafting*, and Dini's *D-Shape*—toward today's industrial-scale gantry and robotic systems capable of printing entire building shells and bridge components. In the Netherlands, this maturation is reflected in the CROW-CUR Richtlijn 5:2023 – 3D-betonprinten [9], which consolidates national practice for design, production, and verification. The guideline defines requirements for material characterization, process control, testing, and life-cycle assessment, formally recognising 3DCP as a compliant method for both non-structural and structural applications.

Current research focuses on increasing process reliability and quality control. Feedback-driven systems use in-line pressure, flow, and rheology measurements to monitor yield stress and stiffness during printing, supporting the "first-time-right" manufacturing principle [10]. These methods bridge digital design and physical production, enabling reproducible fabrication of optimized, formwork-free structures described in the following sections.

1.3 Concrete as a Global Material

Concrete is the most widely used man-made material in the world—second only to water. Its strength, durability, and the availability of its raw materials have made it the backbone of modern infrastructure. However, this ubiquity means that how we design and produce concrete has a major impact on global sustainability [11].

Over the past century, the development of concrete has centred on achieving reliability and uniform performance. Standardisation through national and international codes has ensured safety but also entrenched production methods based on casting and formwork. Most concrete elements are still designed as straight, overdimensioned members that are easy to build rather than materially efficient. This approach favours robustness on site but leads to unnecessary material use and high embodied carbon.

Cement—the binder in concrete—is responsible for roughly 7 % of global CO_2 emissions [2]. Emissions stem from both the calcination of limestone and the fossil fuels used in kilns. While innovations in low-carbon binders and renewable energy sources are advancing, the United Nations Environment Programme highlights that *material efficiency*—using less material for the same function—is among the fastest ways to reduce emissions [11].

Improving material efficiency requires rethinking not only what concrete is made of but how it is shaped and used. Advanced design and fabrication methods allow the material to follow structural needs more closely, minimizing waste and embodied energy. This shift, further explored in Section 1.4, positions digital fabrication as a key enabler of low-carbon construction.

1.4 From Formwork to Freeform Construction

Concrete's widespread use has always depended on temporary molds. Formwork defines both the geometry and much of the cost, logistics, and environmental impact of construction. Transitioning from formwork-based casting to digital, formwork-free fabrication represents a fundamental change in how concrete is designed and built.

In traditional construction, formwork accounts for 30–50 % of structural cost and schedule. Molds must be fabricated, assembled, coated, cleaned, and dismantled for each casting cycle. These labour-intensive steps form a "temporary factory" on every site, limiting scalability and automation. Geometry is often simplified for convenience—flat slabs and orthogonal walls dominate because they are easier to mould, not because they are optimal. Reusable steel or aluminum formwork improves efficiency only for repetitive elements, while unique or curved shapes remain costly and wasteful [9, 4].

Formwork also constrains material efficiency. Reinforcement layouts and concrete placement follow the mold geometry, leading to thicker sections and higher cement use. Additional processes such as vibration and curing add to energy demand. Overall, formwork dictates the rules of construction rather than the design itself.

Digital fabrication with concrete (DFC) breaks this dependency by placing material directly where needed, eliminating temporary molds and associated waste. Additive placement shortens construction time, reduces manual labour, and allows continuous quality monitoring. Printed formwork can even serve as a permanent protective layer or integrate surface functionalities such as texture, colour, or coatings through material grading.

Removing formwork decouples geometric complexity from cost. Curved surfaces, shells, and variable-depth elements become feasible without expensive molds. Real-time monitoring of layer geometry and rheology supports accurate, "first-time-right" production [10].

Coupling additive fabrication with topology optimisation enables designers to remove redundant material and align shapes with stress paths. Studies in digital concrete [8, 12] show that optimized printed geometries can achieve equivalent stiffness and strength with up to 50 % less material than conventional cast components.

The move from formwork to freeform construction thus redefines concrete technology. Material is placed precisely where needed, production becomes automated and data-driven, and design freedom increases without environmental cost. Reinforcement strategies compatible with these processes—such as helical or embedded systems—are discussed in Chapter 4.

1.5 Overview of Digital Fabrication Methods with Cementitious Materials

Digital Fabrication with Concrete (DFC) encompasses multiple approaches that integrate computational design, automated actuation, and advanced materials. While extrusion-based 3D Concrete Printing (3DCP) dominates current research and industry adoption, several complementary processes address different needs and scales.

Extrusion-based 3D Printing. Fresh mortar is pumped through a hose to a controlled nozzle that deposits filaments layer by layer, forming the desired geometry without traditional molds. The balance between pumpability and buildability is critical and is achieved through rheology control and real-time process feedback [9, 10]. 3DCP offers speed and scalability but faces challenges in reinforcement integration and anisotropic strength.

Formwork Printing and Hybrid Casting. Instead of printing the load-bearing concrete, this method prints reusable or sacrificial molds directly from digital models. Thin polymer or cementitious shells can serve as permanent or temporary formwork for casting, enabling complex geometries with minimal waste. The technique bridges digital precision and conventional reinforcement strategies.

Slipforming and Continuous Extrusion. Building on a long tradition of continuous casting, digital slipforming adds robotic control and adaptive geometry. Concrete is extruded beneath a moving formwork, ideal for tall or linear structures such as pylons, walls, and facades. When paired with sensors and adaptive algorithms, this approach can achieve high throughput with consistent quality.

Particle-Bed and Binder-Jet Printing. In these processes, a granular material (such as sand or cement powder) is selectively bonded layer by layer using a liquid binder. Although slower and less scalable, they provide high precision and surface quality, suitable for intricate components, molds, or architectural elements.

Each method balances trade-offs between speed, resolution, material properties, and reinforcement potential. In practice, hybrid workflows are emerging—combining printed molds, robotic reinforcement, and controlled extrusion—to exploit the strengths of each system.

Chapter 2

Process control and material characterisation in 3DCP

Achieving first-time-right manufacturing is a central ambition in digital fabrication with concrete. It implies that every printed element meets its intended quality on the very first attempt, without misprints, rework, or repeated calibration cycles. This ambition is directly linked to productivity and sustainability: every failed print consumes additional material, energy, and labour, whereas consistent first-time-right production reduces all three. Crucially, this capability depends on process control: only when pumping, rheology, extrusion, and deposition are continuously monitored and kept within tight tolerances can the printing system reliably produce first-time-right elements. As a result, when printing processes become sufficiently predictable and controlled, the structural safety factors associated with material uncertainty can gradually be reduced in the future, because the behaviour of the material is monitored and verified in real time.

Reaching such reliability requires understanding the entire printing workflow. By the moment extrusion begins, most quality-defining conditions have already been determined. A first level of quality assurance lies upstream, in the sourcing, storage, and dosing of dry constituents (binders, fillers, and admixtures). The uniformity established at this stage governs the consistency and robustness of the fresh mix. The more complex the formulation, the higher the sensitivity to dosing errors, incompatibilities, and unexplained defects. Although this upstream stage is essential for overall process stability, it lies outside the primary scope of this chapter.

What is central here is in-process quality control during mixing, pumping, and extrusion; the stages where the material interacts directly with the digital fabrication system. Evaluating these stages is crucial for three reasons. First, the material evolves significantly from deposition to the hardened state; its rheological and structural properties change continuously, and each stage imposes different mechanical and environmental conditions. Second, digital fabrication with concrete systems, including extrusion-based 3DCP, are inherently more sensitive to process variations than traditional casting. Small deviations in flow rate, shear history, or timing can strongly influence layer geometry, interlayer bonding, and structural build-up. Third, many printable cementitious systems are highly sensitive to processing conditions: shear, temperature, mixing energy, and residence time can all

alter their performance.

For these reasons, controlling the fabrication process is not merely a matter of print quality, it directly affects long-term structural performance and durability. Robust monitoring allows immediate intervention when an anomaly is detected, minimising defects and material waste while ensuring consistent layer deposition and structural integrity. The following sections therefore examine a typical process chain for extrusion-based 3D concrete printing and highlight representative aspects that influence print quality. In parallel, they introduce measurement approaches that can be used to assess and enhance process control across the entire printing workflow, supporting first-time-right manufacturing and enabling greater material efficiency.

2.1 Different stages and key properties during production

Printable cementitious materials behave as visco-plastic Bingham materials, meaning they remain solid-like and do not flow until the applied stress exceeds a critical yield stress τ_c , after which they deform and begin to flow.

In the process of 3D concrete printing, understanding the different stages of material handling is essential for controlling the behaviour of the printable mix. Each stage imposes specific mechanical, thermal, and geometric conditions on the material, and the relevance of different material properties shifts as the mix progresses through the system. The process is therefore inherently time-dependent, with the evolving state of the concrete governed not only by physical manipulation and chemical change but also by three overarching classes of quality variations: temporal, spatial, and temperature-related effects [10]. These act simultaneously throughout all stages of the workflow.

2.1.1 Different stages in 3DCP workflow

The workflow can be divided into four main stages:

1. Mixing Stage – Dry materials and water are combined and transformed into a fresh mortar. Sub-steps include the initial wetting, where hydration begins and dry pockets are eliminated, followed by secondary blending to achieve a uniform, pumpable mixture. At this point, thixotropy is not yet critical; the main objective is homogeneity and proper water–binder distribution. The residence time distribution (RTD, a probability function that describes how long different particles are likely to remain inside a system) of the mixer is essential here: insufficient residence time yields inhomogeneous material, whereas excessive residence time induces early structuration or hydration. The material strategy (i.e., 1K (mono-component) or 2K (bi-component)) also shapes this stage, as 2K systems may introduce accelerators later in the process, relaxing early-age mixing constraints.

2. Pumping and Transport Stage – The material is conveyed through hoses and pipes under steady shear. Here, the mix must remain sufficiently fluid and stable to avoid segregation, dead zones, or clogging. Beyond simple pumpability, this stage is strongly affected by spatial inhomogeneities, especially flow-induced particle

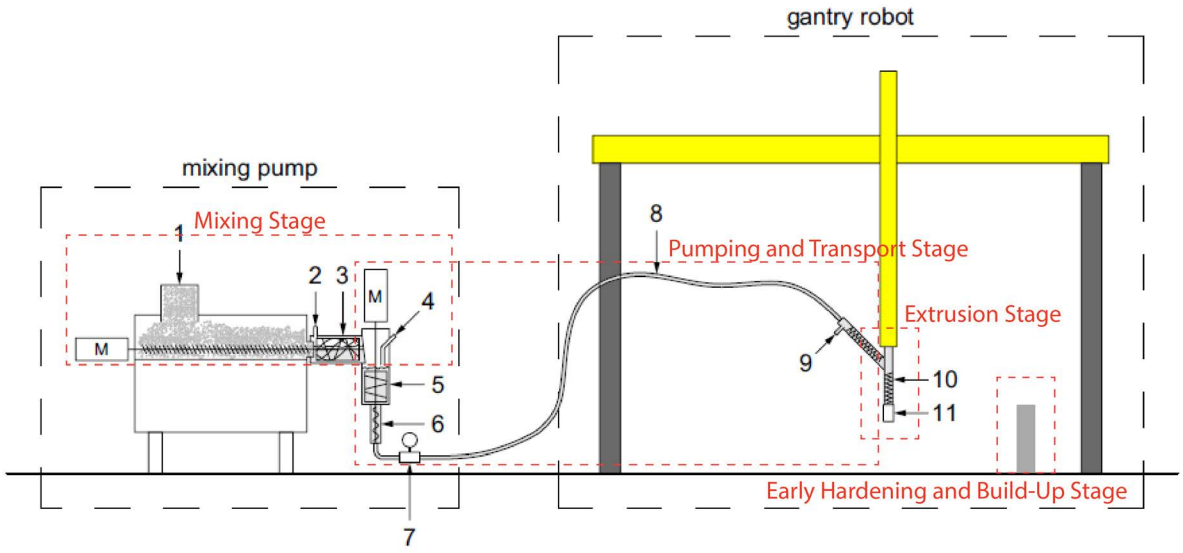

Figure 2.1: Schematic overview of the 3D concrete printing system with the mixing pump and gantry robot. (1) Inlet for the dry premix. (2) Water inlet. (3) Horizontal mixing chamber. (4) Tracer injection port A. (5) Vertical mixing chamber. (6) Progressive cavity pump. (7) Mortar pressure sensor. (8) 10 m-long hose. (9) Tracer injection port B. (10) Helical static mixing elements. (11) Nozzle with the detection device (see Fig. 2). Taken from [13]

migration. As the velocity profile develops, a lubrication layer typically forms at the wall, while a stiffer plug may arise in the core. The extent of this migration depends on inertia, viscosity, and yield stress, and affects the uniformity of the material arriving at the nozzle. The RTD of hoses also contributes to temporal variations: parcels that rest in plug regions experience structural build-up, while sheared parcels do not. For 1K systems, build-up during pumping is often undesirable; for 2K systems, structuration mainly occurs after accelerator injection.

3. Extrusion Stage – The mixture experiences a strong shear pulse as it passes through the nozzle and transitions from internal flow to layer-by-layer deposition. Thixotropy becomes essential: the material must switch rapidly from a flowable state to a self-supporting state. Nozzle geometry acts as a local reactor with its own short but non-negligible RTD. The shear pulse also partially resets the structuration state (particularly the static yield stress), after which rebuilding begins immediately once shear ceases. Flow-regime transitions, such as collapse of the lubrication layer or recompression of migrated particles, can affect filament surface quality and interlayer bonding.

4. Early Hardening and Build-Up Stage – After deposition, the concrete must regain stiffness and strength rapidly to support subsequent layers. This stage is increasingly governed by hydration, particularly in 2K mixes where the chemical reaction is intentionally accelerated near the nozzle. The balance between thixotropic recovery (which controls early structural stability) and hydration (which governs long-term stiffening) determines the buildability limits. Spatial inhomogeneities inherited from pumping (e.g. lubrication layer) can influence surface porosity, layer bonding, and durability.

As the material moves through these stages, its behaviour is shaped jointly by material properties, processing conditions, and systemic variations. The primary process factors, residence time, mixing energy, shear history, temperature rise, and process variations such as stop–start cycles, define the mechanical and thermal environment in which the concrete evolves.

Among these, the residence time distribution is one of the most critical descriptors: it determines how long each parcel experiences mixing, shear, rest, or elevated temperature, and thereby contributes both to desired homogenisation and to undesired variations in structuration or hydration.

The internal evolution of the material is governed by two key mechanisms:

- Thixotropy, the reversible breakdown and rebuilding of the particle network. Under shear, the structure breaks down and the dynamic yield stress decreases; at rest, the structure rebuilds and the static yield stress increases.

  Hydration, an irreversible chemical reaction that forms hydrates and progressively increases stiffness, strength, and sensitivity to time and temperature.

The interaction between these mechanisms (superimposed on different shear histories imposed by mixers, pumps, hoses, and the nozzle) controls the transition from a pumpable paste to a load-bearing structure. Their combined effects are strongly modulated by system temperature, which increases due to mechanical energy dissipation and can accelerate both evaporation and hydration.

At any moment within the process, the state of the material is expressed through its rheological properties, which quantify how the material begins to flow, how it deforms, and how it stabilises once deposited. These properties manifest differently across the system:

- inside the mixer and pump, where fluidity and sufficient de-structuring are required for homogeneous feeding;
- in the hose, where steady shear, plug flow, or particle migration may occur;
- at the nozzle, where a high shear pulse resets structural state;
- after deposition, where structural build-up must be rapid and spatially consistent.

In practice, three principal rheological parameters characterise printable concrete:

- Flowability – Governs ease of movement under pressure. High flowability aids pumping and extrusion, but excessive flowability can promote segregation, excessive lubrication layers, or geometric deformation.
- Yield stress – The stress required to initiate flow. Its static and dynamic values dictate layer stability, pumping pressure, and interlayer bonding.
- Plastic viscosity – The resistance to continued deformation once flow begins. Lower viscosity favours pumping; higher viscosity stabilises the extruded filament.

These parameters are the measurable outcomes of thixotropy and hydration, mediated by process conditions such as RTD, shear history, particle migration, and temperature rise. Their time evolution determines whether the mix behaves as a stable, controllable material or drifts toward inhomogeneity, blockage, or loss of print fidelity. Deviations (caused by inaccuracies in dosing, suboptimal mixing, sudden flow-rate changes, or thermal effects) manifest as poor surface quality, inconsistent layer shape, weakened interlayer bonding, or geometric distortion.

In summary, the four material-handling stages describe where and how the material is transformed; the temporal, spatial, and thermal variations describe the mechanisms through which quality issues arise; process factors such as residence time and shear history define the environment for this evolution; thixotropy and hydration explain the internal structural changes; and rheology quantifies the resulting flow behaviour that ultimately governs printability and build quality. Mastery of these interacting factors is essential for achieving stable, first-time-right manufacturing in extrusion-based 3D concrete printing.

2.2 Fresh-state

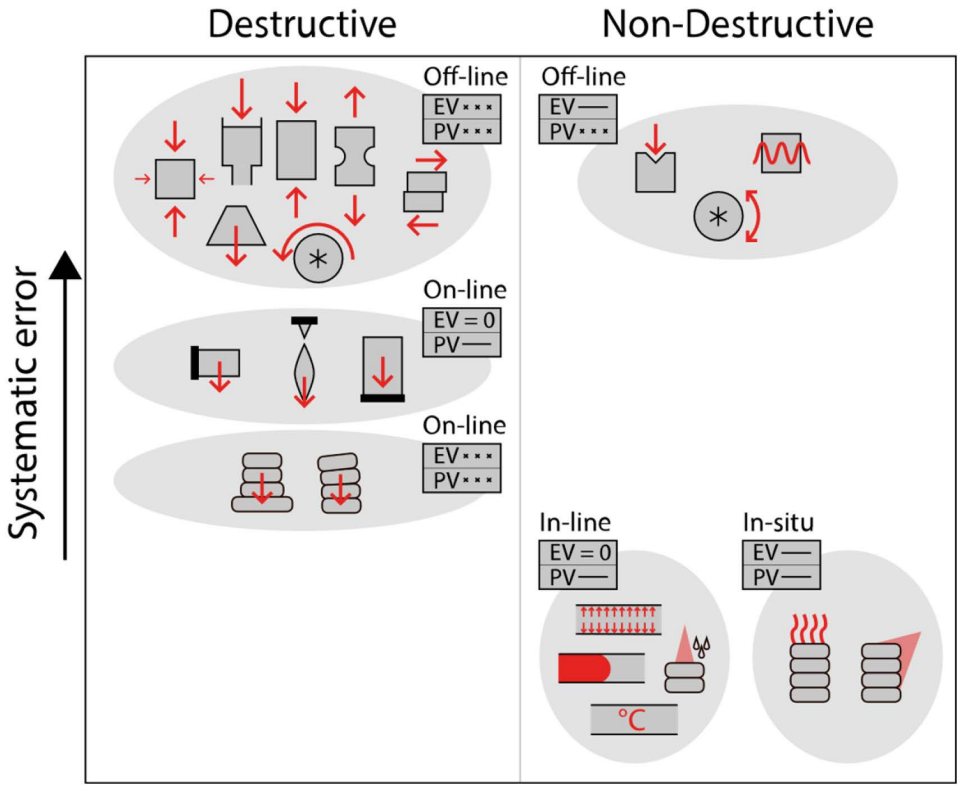

Figure 2.2: Framework for quality control as presented by Bos and Wolfs [14]. Taken from [15].

Unlike conventional casting, where formwork supports the material until it hardens, digital fabrication exposes fresh concrete immediately after deposition. Its shape stability and surface quality therefore depend on continuously evolving mechanical

properties and tightly controlled processing conditions. The study argues that future 3DCP systems will need real-time monitoring, feedback, and data integration—far beyond the sampling-based quality checks used for traditional concrete. Bos and Wolfs [14] provide a systematic overview of how quality should be monitored in digitally fabricated concrete processes.

The authors propose a categorization framework that classifies quality-control methods according to (i) whether they are destructive or non-destructive, (ii) their systematic error compared with real process conditions, and (iii) the location of measurement relative to the fabrication process: off-line, on-line, in-line, or in-situ. They apply this framework to the fresh-state mechanical performance of printed concrete, mapping common test methods, from rheometers and penetration tests to near-nozzle and sensor-based approaches, according to how well they capture material evolution and process variations. The result is a roadmap linking each type of experiment or sensor to the specific information it provides during printing.

The paper concludes that digital fabrication requires an integrated, hierarchical approach to quality control, combining destructive laboratory tests with in-line sensors and computer-vision-based monitoring. Standardized test protocols and inter-laboratory correlations are identified as key research needs for moving from bespoke academic experiments toward industrial certification.

The paper creates a good overview of the potential tests and thus in this teaching material we will follow this framework and try to give an overvview of some of the testing methods. Below we list some of the fresh state measurement options, for further detail look at work by Bos and Wolfs [14], also for different potential strategies for quality control.

2.2.1 Fresh state destructive testing

Uniaxial unconfined compression test

The uniaxial unconfined compression test (UUCT) provides a direct measure of the early-age compressive strength and deformation behaviour of fresh or weakly hardened printable concretes. A similar procedure has been applied in previous 3DCP research by Wolfs et al. [16], and the present description follows the same methodological principles, as shown on Figure 2.3. Cylindrical specimens are prepared in accordance with ASTM D2166, using moulds sized to minimise particle-size effects (typically $d = 70$ mm and $h = 140$ mm, maintaining $h/d = 2$ to promote a diagonal shear failure mode). The fresh material is placed in Teflon-lined steel moulds and compacted on a vibration table to ensure homogeneous density. Prior to testing, the cylinder is demoulded and positioned between two steel loading platens of matching diameter, with double Teflon sheets on each interface to approximate frictionless boundary conditions. The tests are performed in displacement control using an electromechanical testing machine (e.g., an INSTRON equipped with a 5 kN load cell), typically at a loading rate of 30 mm/min to replicate printing-induced deformation rates while limiting thixotropic stiffening during the test. Load, displacement, and deformation fields are recorded throughout loading. Because the low stiffness and large deformations of fresh material hinder the use of physical extensometers, non-contact optical measurement systems are employed to track vertical and

lateral strain via surface markers. In cases where local shear bands disrupt local strain measurements, global deformation is obtained from high-resolution images processed with vision-analysis software. Together, these measurements yield reliable stress–strain curves and strength values for quality assessment and process monitoring.

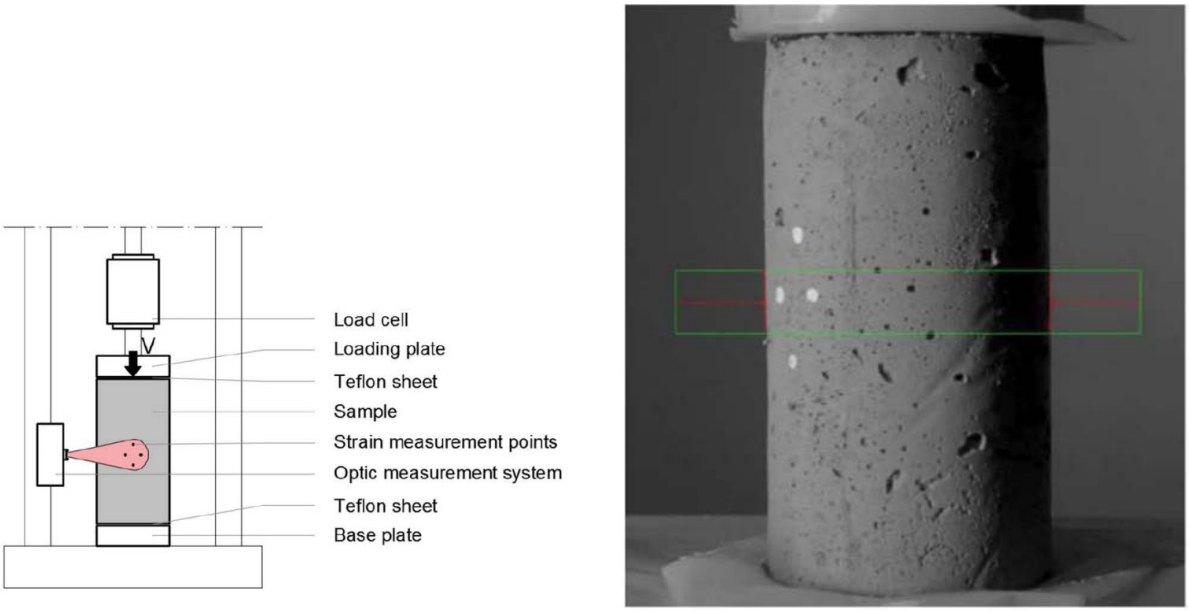

Figure 2.3: Schematic presentation of test setup of Uniaxial Unconfined Compression Test. Taken from [16].

Squeeze Flow

The squeeze flow test is commonly used to characterise the uniaxial compression behaviour of firm, low-deformation printable concretes and is closely linked to the assessment of buildability, i.e. the ability of early layers to sustain the self-weight of subsequent layers, as shown by Jacquet [17] and seen on Figure 2.4. In this test, a cylindrical specimen with a typical aspect ratio of 2:1 is placed between two parallel, well-lubricated steel plates and compressed at a controlled displacement rate to ensure quasi-static loading conditions. The chosen slenderness helps minimise particle-size effects and promotes the development of a diagonal shear failure plane. During testing, the lateral expansion of the material may become significant; therefore, the instantaneous diameter of the specimen can be updated to compute the compression stress more accurately. The compression yield stress, or uniaxial compressive strength $\sigma_{c,u}$, is defined as the ratio between the maximum applied force and the updated cross-sectional area of the deformed sample. This method provides a direct measure of the material's compressive resistance in the fresh state and supports the prediction of plastic collapse in early-age printed structures.

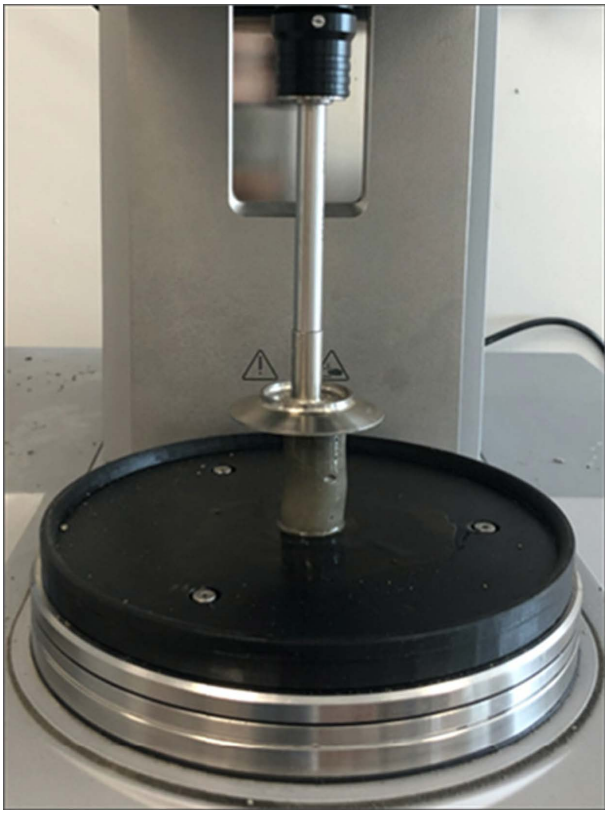

Figure 2.4: Squeeze flow test, taken from [17].

Flow Table Test

The flow table test is a standardized method used to quantify the flowability of fresh mortar by measuring its spread after controlled jolting. In accordance with NEN-EN 1015-3 [18], the test uses a stainless-steel truncated cone mould positioned centrally on a smooth steel disc mounted on a hinged flow table, illustrated on Figure 2.5. The mould is filled in two layers, each compacted with a prescribed number of tamping strokes to ensure uniform consolidation. After surplus mortar is removed and the mould is lifted vertically, the table is dropped fifteen times at a controlled frequency using a mechanical lifting cam. The mortar spreads across the disc, and the resulting flow diameter is measured in two perpendicular directions; the mean of these measurements represents the flow value. To ensure reliability, the test is repeated on the same batch, and deviations larger than 10% require preparing a new specimen. As a destructive test on fresh-state material, the flow table test provides a direct assessment of mix workability and consistency prior to pumping or printing.

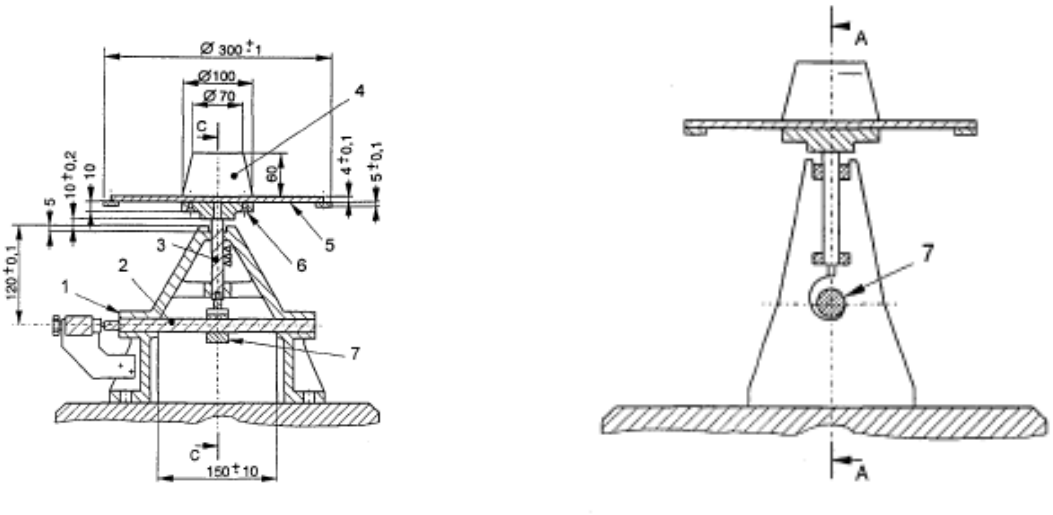

Figure 2.5: Schematic presentation of test setup of flow table test. Taken from [18].

Triaxial compression test

A triaxial compression test (TCT) was developed to characterise the early-age mechanical behaviour of fresh printable concrete under axisymmetric loading conditions, following the methodology of Wolfs et al. [19]. In contrast to traditional soil testing, TCTs on fresh concrete must be performed quickly to minimise the influence of structural build-up and hydration during preparation. Cylindrical specimens were cast in Teflon-lined steel moulds without external compaction, providing a closer representation of the in-situ printed material. The samples had a diameter of $d = 25$ mm and height $h = 50$ mm, maintaining $h/d = 2$ as recommended in ASTM D2850 to promote a diagonal shear failure mode. During testing, the specimens were placed between lubricated steel plates inside a sealed acrylic chamber and subjected to a confining air pressure σ_c while a vertical load was applied through a displacement-controlled ram. The resulting principal stresses satisfied $\sigma_1 = \sigma_p + \sigma_c$ and $\sigma_2 = \sigma_3 = \sigma_c$, as illustrated schematically in Fig. 2.6. Tests were conducted for several confining pressures, ranging from unconfined conditions up to twice the expected uniaxial strength, enabling the derivation of Mohr–Coulomb strength parameters. Because of the low stiffness and large deformations of the fresh material, physical extensometers could not be used; instead, lateral deformation was captured through high-resolution images taken through transparent chamber walls and evaluated in real time using optical tracking software. For each concrete age and confining pressure, multiple specimens were tested, allowing the evolution of strength and deformation behaviour to be quantified over the first 90 minutes after extrusion. This test provides essential data for constitutive modelling and numerical simulation of layer-by-layer build-up in 3D concrete printing, described in [19].

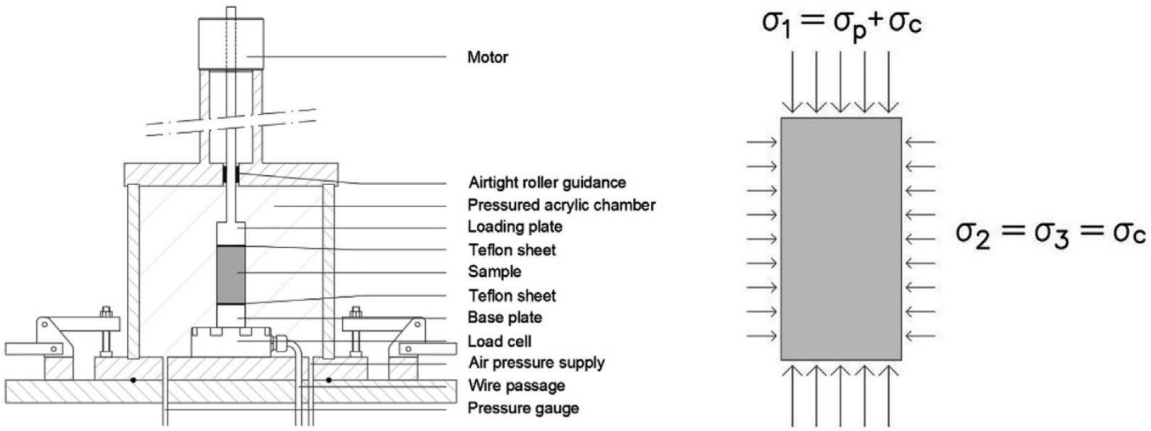

Figure 2.6: Schematic of the triaxial compression test set-up (left) and corresponding axisymmetric stress conditions (right), adapted from Wolfs et al. [19].

Tensile tests on fresh state concrete

A variety of tensile testing methods have been developed to characterize the early-age tensile behaviour of fresh cement-based and printable materials, each addressing the practical challenges associated with testing low-strength, time-dependent, non-clampable specimens. Mettler et al. [20] introduced a notched tensile test in which fresh self-consolidating concrete is cast into a two-part mould equipped with lateral pins to ensure shear transfer. The specimen is split horizontally at constant velocity, enabling tensile failure to be induced in a controlled manner despite the material's inability to sustain clamping forces. Jacquet et al. [17] proposed the Double Dumbbell Device, in which self-standing, firm printable materials are cast in a symmetric dumbbell-shaped geometry and pulled in tension using a rheometer-operated load cell, seen on Figure 2.7. This configuration enables a direct determination of tensile yield stress for materials with sufficiently high structural build-up to maintain stability during specimen handling, thereby avoiding drainage or segregation.

Figure 2.7: Double Dumbbell device filled with mortar and in the testing equipment. Taken from [17].

Direct shear tests

The direct shear test (DST) was used to evaluate the early-age shear strength parameters of fresh printable concrete, following the general principles of ASTM D3080 and the setup described by Wolfs et al. [16]. Cylindrical specimens with a diameter of $d = 70$ mm and height $h = 40$ mm were prepared in a two-part shear box by filling and compacting the fresh material in three layers to obtain a homogeneous density. The shear box consisted of two horizontal plates with aligned circular openings, forming a well-defined shear plane at mid-height of the specimen. During testing, a Schenck RM100 frame equipped with a 100 kN load cell translated the vertical displacement of the ram into a constant horizontal displacement of 15 mm/min via a pulley–cable mechanism, imposing shear deformation on the upper half of the specimen (Figure 2.8). External normal loads of 0, 10, and 20 N were applied using steel weights, which, together with the self-weight of the upper concrete half, produced nominal normal stresses of 1.5, 11.5, and 21.5 N on the shear plane. These loading combinations enabled determination of the time-dependent cohesion $C(t)$ and internal friction angle $\varphi(t)$. To minimise friction within the shear box, machined grooves in both plates accommodated four steel balls acting as rollers, reducing system friction to approximately 6% of the weakest sample's failure load. Each test lasted approximately 1.2 minutes, sufficiently short to limit thixotropic stiffening during loading, and five replicates were performed for each age–load combination.

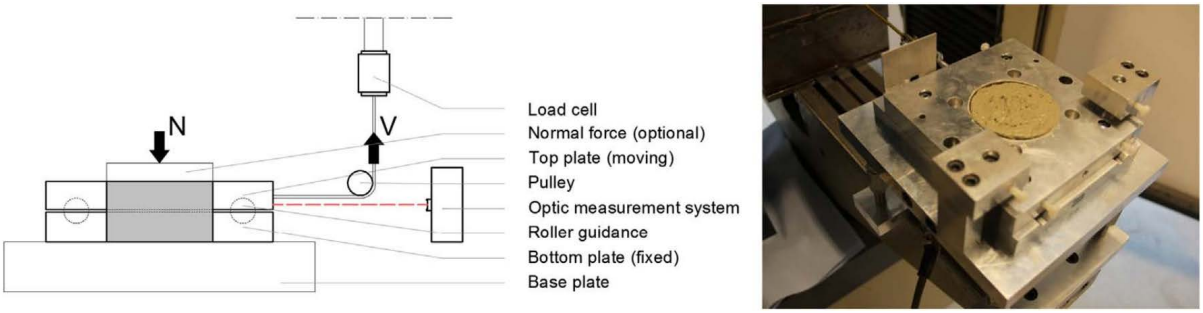

Figure 2.8: Schematic of direct shear test (left) and photograph of the setup without a normal load applied (right). Taken from [16].

Vane test

The vane test (or scissometer) is a classical method for determining the shear yield stress of cohesive materials by applying a torque to an immersed vane until the material reaches its yield point ($\tau = \tau_c$). The test generates an almost ideal shear stress field and has long been standardised for fine-grained cohesive soils [21]. In cementitious materials, vane-type devices have been used to quantify both shear yield stress [22] and early-age structuration behaviour [23], with results shown to correlate well with controlled-stress rheometry [24]. However, conventional scissometers require relatively large sample volumes, limiting their practicality for 3D concrete printing (3DCP).

A smaller variant, the *pocket vane* (or Torvane), provides a compact and rapid alternative, seen on Figure 2.9. Instead of being fully immersed, the device is placed directly onto the surface of the specimen, engaging only the top $\sim$5 mm of material. Originally developed for in-situ testing of fine-grained soils [25], the pocket vane has recently been adapted for printable mortars used in digital fabrication. It enables fast and affordable measurements of early-age structuration relevant to 3DCP, as demonstrated by Demont et al. [26].

Figure 2.9: A pocket shear vane HumboldtH-4212MH, images taken from [26].

The critical torque T_{cr} applied during testing results from two shear contributions: (1) the lateral cylindrical surface and (2) the horizontal bottom surface of the engaged material volume. Based on the classical analysis of Cadling and Odenstad [25], the torque is given by

$$T_{cr} = \frac{\pi D^3 \tau_{cr}}{12}\left(1 + \frac{6H}{D}\right), \tag{2.1}$$

where D is the vane (or loaded cylinder) diameter, H its height, and τ_{cr} the shear strength at rupture. Interchangeable vane heads can be selected depending on the strength range of the tested material.

In Demont et al. [26], a dedicated testing protocol is proposed for 3DCP applications. The authors demonstrate two modes: (i) *off-line* testing on cylindrical specimens filled directly from the print extruder, allowing repeatable sets of measurements (Fig. 7a–b), and (ii) *on-line* testing performed directly on freshly printed layers (Fig. 7c). These approaches offer a practical, non-destructive way to monitor structural build-up during printing, making pocket-vane methods an accessible component of real-time quality control strategies.

The present explanation is adapted from the discussion originally provided in [27].

Constant shear rheometry

Constant-shear rheometry is used to characterise the time-dependent structural build-up and flow behaviour of cementitious materials by subjecting a fresh sample to a controlled, constant shear rate and monitoring the resulting shear stress response. After an initial conditioning step, typically achieved through small-amplitude oscillatory shear to establish a reproducible initial state within the linear viscoelastic regime, the material is sheared at a fixed rotational velocity or nominal shear rate. The evolution of shear stress under this constant loading provides the static or structural yield stress, revealing how rapidly the internal microstructure rebuilds when the material is at rest. By repeating the test at different ages, the method captures thixotropy, structuration kinetics, and deviations from ideal plasticity criteria. When combined with complementary shear-rate sweeps, the data allow determination of rheological parameters such as the Bingham or Herschel–Bulkley constants, enabling comparison across mix designs and quantification of how composition, rest time, and particle characteristics influence printability-relevant properties such as consistency, yield stress, and early structuration. For example Viskomat XL could be used for this purpose, seen on Fig. 2.10. More detailed overview of these tests are given in [17, 28].

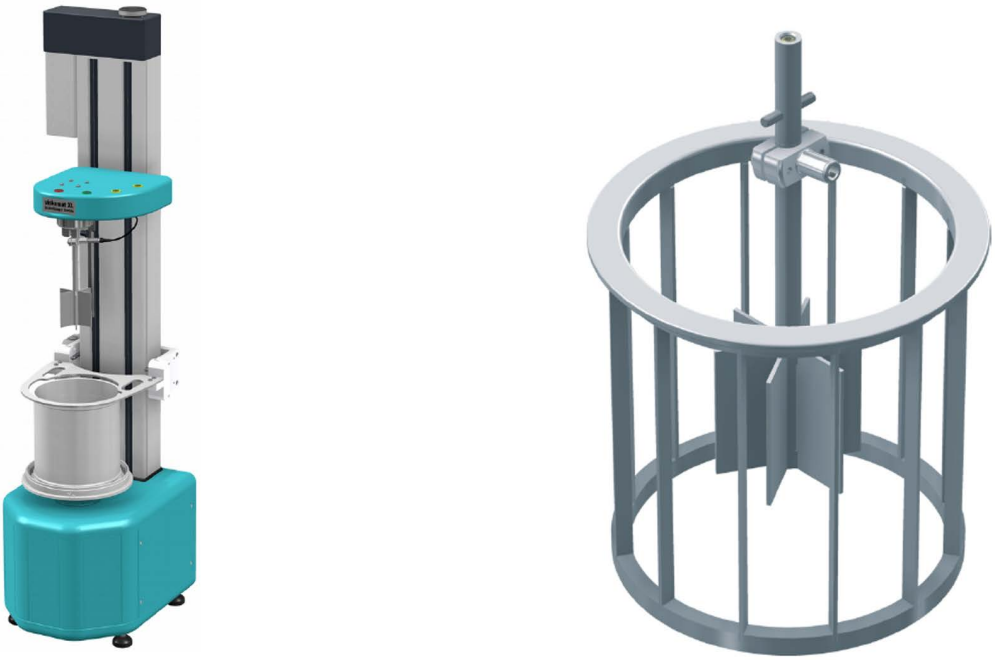

Figure 2.10: Representation of Viskomat XL, taken from [29]

RAM Extruder

The ram extrusion test, illustrated on Figure 2.11, is used to characterise the extrusion behaviour of frictional–plastic, cement-based materials and to identify the physical mechanisms governing their forming process. In this test, a cylindrical barrel is filled with a fresh cementitious paste, and a piston (ram) pushes the material through a die at a controlled displacement rate.

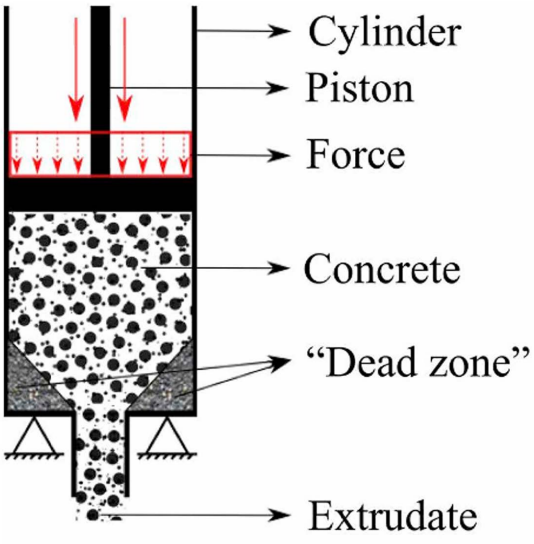

Figure 2.11: A sketch of the ram extruder, taken from [30].

As the material flows, it typically exhibits plug flow, with the bulk moving as a

quasi-rigid body while slipping with friction along the extruder walls. The total extrusion force represents the combination of (i) the shaping force required to deform the material through the die entry, and (ii) the wall-friction force acting in the plug-flow zone. Because cement-based pastes behave as high-yield-stress, heterogeneous granular suspensions, the pressure gradient induced during extrusion can cause liquid filtration, promoting consolidation of the granular skeleton and a time-dependent increase in yield stress and wall friction. As a result, the extrusion force generally rises during the test rather than reaching a constant plateau, reflecting the evolving material state. From the measured force–displacement curve, the ram extrusion test enables the determination of plastic deformation resistance, wall friction stress, apparent yield stress, consolidation behaviour, and extrudability limits of the material. These properties can be interpreted using soil-mechanics–based models (e.g., Coulomb or Drucker–Prager) and tribological relations (e.g., Janssen theory) to link the developing axial and normal stresses within the paste to its frictional plastic response. The test therefore provides a powerful means of predicting extrusion forces for different combinations of paste rheology and extruder geometry, assessing process stability, and identifying conditions that may lead to filtration, blockage, or non-uniform filament formation in extrusion-based 3D concrete printing. More detailed overview of these tests are given in [31, 30].

Slump test

Although slump is the conventional workability indicator used for traditional concrete, it is not necessarily an appropriate or sufficient measure for 3D concrete printing (3DCP). Nevertheless, slump-based tests can still provide a preliminary indication of flow behaviour. As noted in [32], the slump test itself does not yield a physical rheological parameter and cannot be expressed directly in rheological units. Despite this limitation, it has historically proven useful for classifying concretes by their castability, for instance through the well-known ASTM Abrams cone [33] or paste-cone variants[34].

In conventional concrete production, slump has traditionally been the sole parameter used to monitor and control fresh-state quality [35]. By contrast, 3DCP requires a far more detailed and multi-parameter quality-control approach, as numerous process-sensitive features govern printability, buildability, and final product performance [36]. Rheological measurements, especially yield stress, structuration rate, and thixotropy, are therefore essential.

Slump-type tests are still used in research when adapted for higher-precision rheological evaluation. For example, in the smart dynamic casting work of Szabo et al. [37], a Hagerman mini-slump cone (60–70–100 mm) was used to assess workability both before and after acceleration. The accelerated mixes were tested at controlled times to simulate the interval between activation and deposition in a slip-casting setup. Importantly, the authors did not treat slump solely as an empirical indicator; instead, they calculated the yield stress from the slump-flow diameter using the analytical model developed by Roussel and Coussot in the “fifty-cent rheometer” framework [32]. This demonstrates how modified slump-flow tests, when combined with appropriate modelling, can serve as a low-cost but physically interpretable method for estimating yield stress in cementitious systems relevant to 3DCP.

Slugs test

In extrusion-based 3D printing, the behaviour of the material as it exits the nozzle provides valuable information about its rheological state, particularly the yield stress and flow stability that govern extrusion continuity and print quality. Bos and Wolfs [38] introduced an early and influential step toward automated, high-frequency quality monitoring in digital concrete fabrication. Conventional testing methods typically rely on manual or off-line measurements, which are too slow and disruptive for real-time process control. This research proposed a method to observe the same parameters automatically and in real time by analysing the formation of small droplets or "slugs" near the nozzle.

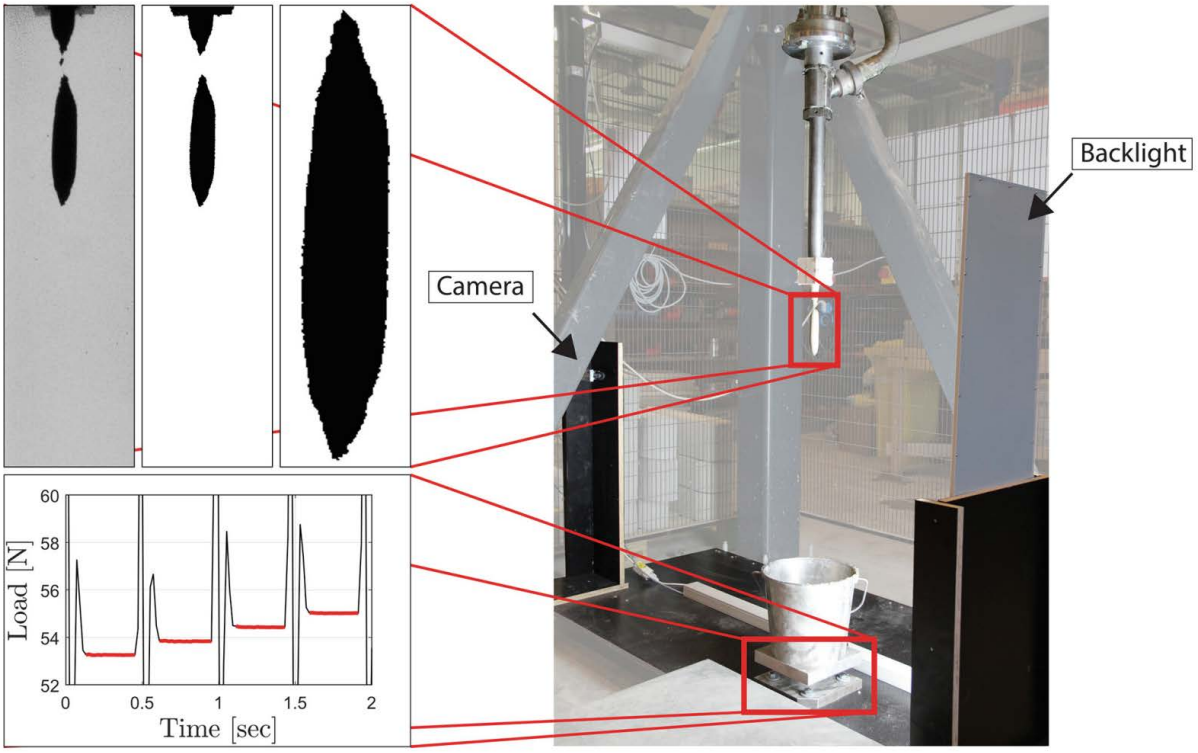

Figure 2.12: Typical visual measurement (top left) and load cell measurement (bottom left), test setup (right) with the camera and load cell highlighted. A backlight is applied to improve contrast, taken from [38].

The approach integrates two synchronized measurement systems: a load cell placed below the nozzle to measure the mass of the falling droplets and a high-speed camera that records their geometry. Using backlighting and automated image analysis, the camera reconstructs the droplet's three-dimensional volume, enabling machine-vision-based estimation of density and rheological behaviour. By comparing mass and volume across different water contents and flow rates, the study quantified how printing conditions influence material performance. Additional analyses addressed measurement uncertainties (such as droplet rotation or camera alignment) demonstrating that the system achieves high accuracy using a single-camera setup.

The results show that automated visual inspection extends the applicability of near-nozzle droplet analysis to materials and flow conditions typical of industrial-scale 3D printing. This enables reliable monitoring even at high extrusion speeds where

conventional mass-based tests fail. The method demonstrates that integrating vision systems directly into the printing process can support on-line quality control, providing fast feedback on material consistency and early detection of process instabilities.

Inverse slugs test

Understanding the material's behaviour directly after extrusion is essential for predicting the stability of printed layers. Most early on-line tests in 3D concrete printing have focused on the tensile yield stress (such as the slugs test), yet in practice, freshly deposited concrete primarily experiences compressive loading as it supports its own weight and additional layers. To address this gap, Bos [15] developed the Inverse Slugs Test, seen on Figure 2.13, an on-line gravity-induced compression experiment that measures the Young's modulus and yield stress of fresh printable concrete under compression. The method allows evaluation of the material's stiffness and strength in real time, providing insight into how rapidly the material gains structural capacity after extrusion.

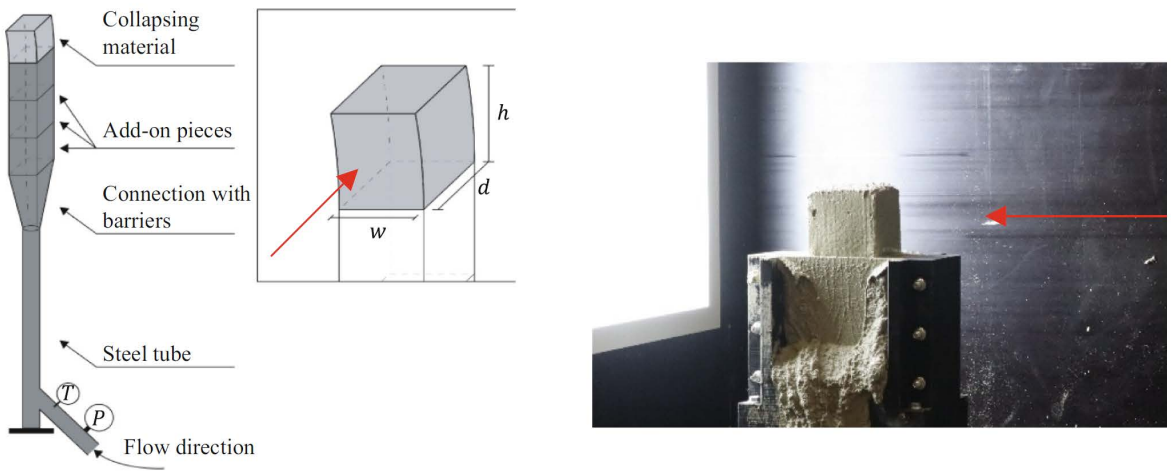

Figure 2.13: Schematic of the test setup (left) and in reality (right) with the camera viewing direction indicated by the red arrow, taken from [15].

In this test, the material is extruded vertically upward through a rectangular nozzle until the column collapses by buckling or plastic compression failure. The collapse height is recorded with a camera, and the measured deformation behaviour is compared to analytical predictions. By varying the nozzle width and length, the researchers examined how structuration time (the time between the last shear event and load bearing) affects stiffness development. The study found that the material's stiffness stabilizes within the first four seconds after extrusion, and that the failure mode transitions from buckling to plastic collapse with increasing nozzle width. The results confirmed that stiffness, rather than strength, often governs the maximum achievable layer height in extrusion-based printing.

Although the Inverse Slugs Test is relatively labor-intensive and better suited for research than continuous monitoring, it provides a validated way to quantify compressive stiffness development during printing. This information supports nozzle

design optimization and helps to calibrate process models linking material rheology, extrusion parameters, and buildability. The method complements tensile-based assessments, contributing to a more complete understanding of early-age structural behaviour in 3D-printed concrete. A more detailed discussion can be found in [15].

Production trials

Another practical approach for characterising material behaviour during 3D concrete printing is to perform production trials directly on the print bed. In these tests, a wall or simple geometry is printed until either deformation or structural failure occurs. From the recorded response, the relevant material properties can be back-calculated using appropriate structural or numerical models. This reverse-engineering approach depends on an accurate representation of the printed geometry, boundary conditions, and process parameters. The deformation and failure behaviour of printed elements (whether governed by plastic collapse or elastic buckling) is strongly influenced by the evolving material strength and stiffness during printing [39, 40, 16, 19].

When designed carefully, such production trials provide valuable insight into these evolving properties. This methodology was demonstrated in [40], where a series of straight wall elements of varying size were printed up to failure. Using a set of cameras, the progressive deformation of each wall was monitored as layers accumulated, enabling precise identification of the structural height (or number of layers) and the corresponding failure mode. By combining these observed responses with known process parameters (such as printing speed, material flow rate, and nozzle trajectory) and substituting them into established mechanistic or numerical models for extrusion-based printing, it is possible to infer the material strength, stiffness, and their structuration rate throughout the experiment. Because these tests employ exactly the same material, equipment, and process settings used during actual printing, they yield material properties that are highly representative of in-situ printing behaviour.

However, this approach is inherently destructive, performed at a low sampling rate, and can require large quantities of material, particularly when the relevant structuration time is long. If the structuration rate is very high (e.g. for accelerated (2K) systems) the element may stabilise before collapse occurs, preventing failure-based characterisation. A non-destructive variant is also possible in which the printed object is not loaded until collapse. Instead, the (elastic) deformations during printing are measured and used to infer the evolution of stiffness parameters. While this provides valuable information on rigidity development, it does not give direct insight into strength properties. This rewritten section is based on the explanation originally presented in Wolfs et al. (2024) [27]. The mechanistic model developed by Suiker [39] and the procedure [40] is described in more detail in Chapter 3.

2.2.2 Fresh state non-destructive testing

Penetration tests

Penetration (indentation) tests form a broad family of methods originally developed to monitor setting of cement-based materials, starting from the Vicat needle and extending to penetrometers, Proctor needles and Hilti needle guns [35]. In all cases, a

probe (needle, cone, sphere) is driven into the material at a prescribed velocity while the penetration force is recorded as a function of time or depth. From this force, an effective stress can be computed and related to yield stress, provided the probing geometry is known and the effective contact area remains well defined (e.g. by ensuring the gap above the tip does not close in more liquid systems) [35, 41]. Depending on the tip shape and speed, either simple force/area estimates or more advanced analytical solutions (e.g. soil-mechanics–based bearing capacity factors or falling-sphere analogies) are used to derive yield stress and, in some regimes, plastic viscosity [36, 41].

For printable cement-based materials, penetration tests have been adapted to capture the time-evolving yield stress and consistency over the entire setting range. A key parameter is the penetration velocity: at very low velocities, the test probes visco-elastic "solid" or creep-like behaviour below the yield stress; at very high velocities, viscous contributions may contaminate the signal; and at intermediate velocities, the measured force becomes approximately velocity-independent and scales primarily with yield stress [41]. Both fast (discontinuous) penetration tests and slow (continuous) penetration tests have been developed. Fast tests (single insertions at selected times, often on printed layers) are well suited for on-site quality control in 3D printing, where structuration rates are high. Slow tests, performed at extremely low velocities with fully submerged tips, allow continuous tracking of the exponential strength gain over several hours and show good agreement with complementary methods such as vane rheometry and uniaxial compression, confirming that penetration force is a robust proxy for yield stress.[36]

Practical aspects such as container diameter, wall slip and probe size relative to particle size are critical to obtaining reliable data [35, 36]. For example, Reiter showed that penetration forces scale with contact area and are influenced by container diameter through wall slip, leading to recommended minimum container sizes and depth-correction factors for conical tips [36]. Overall, penetration tests provide a versatile bridge between traditional setting-time assessments and rheological characterisation of printable concretes, offering high potential for inline or near-inline quality control in extrusion-based 3D printing [41].

A recent extension of this family of methods shifts from penetration-type yield-stress tests toward a mechanics-based indentation approach, in which the full load–depth response is interpreted rather than a single penetration force. In this framework the test is placed in non-destructive section, however in this specific case the specimen is destroyed (however next developments along these lines could change this). Nontheless, in this method, a rigid indenter is pressed into the fresh material and the measured force–displacement curve is analysed using an analytical cavity-expansion model governed by the Mohr–Coulomb failure criterion. The initial part of the response reflects predominantly elastic behaviour and is used to determine the elastic modulus, while continued indentation induces progressive elastic–plastic deformation from which cohesion and internal friction angle are identified. Importantly, the indentation response is elastic–plastic throughout, without a distinct purely plastic regime, and material parameters are extracted by fitting the full loading curve. By repeating the test at different times after mixing, the time-dependent evolution of these parameters due to hydration and structuration

can be quantified. The approach has been demonstrated on early-age cementitious materials developed for 3D concrete printing and provides a fast, minimally invasive alternative to multiple conventional tests; for a detailed theoretical formulation and experimental validation, the reader is referred to Deetman and Suiker [42].

Ultrasonic wave transmission

Ultrasonic pulse velocity (UPV) testing is commonly used to monitor the evolution of strength and to determine setting times in cementitious materials, as well as to identify internal defects. More recently, ultrasound techniques have also been adopted within digital fabrication and 3D concrete printing [43], seen on Figure 2.14. In this method, an ultrasonic pulse is transmitted into the material and either received by a transducer positioned on the opposite side of the specimen or reflected back to the emitting transducer. By measuring the travel distance and the corresponding time-of-flight, the ultrasonic velocity can be calculated. Recent studies have shown that this velocity, and particularly its evolution with material age, correlates strongly with the early-age development of stiffness modulus and compressive strength within the time frame relevant to 3D concrete printing [43]. Because the method is non-destructive, a single specimen is often sufficient to capture the full evolution of material behaviour. Owing to its automated and digital nature, UPV testing has strong potential for integration into 3D printing as an *in-line* monitoring tool.

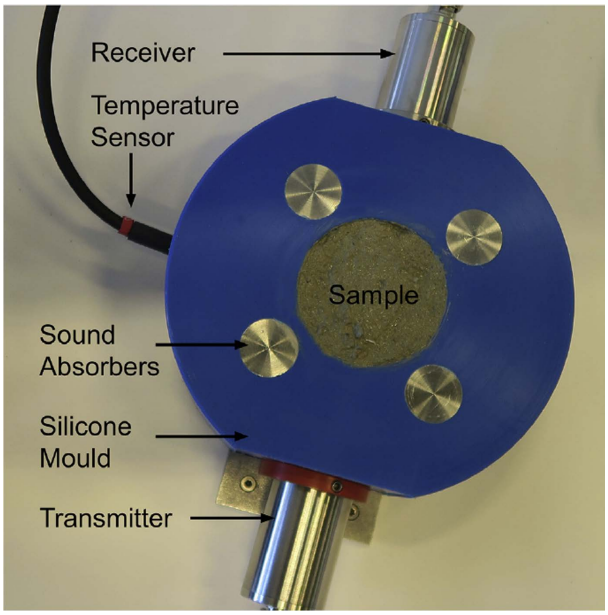

Figure 2.14: Ultrasonic pulse velocity testing equipment IP8, manufactured by Ultra-test GmbH, taken from [43].

This rewritten section is based on and adapts the original explanation presented in Wolfs et al. (2024) [27], with additional elaboration for clarity and completeness.

In-line geometric monitoring

In-line geometric monitoring has emerged as a key enabler for automated quality assessment in extrusion-based 3D concrete printing. Unlike traditional casting,

where formwork provides geometric confinement, 3DCP requires the printed filament to achieve dimensional accuracy and structural integrity without external support. Consequently, real-time measurement of the deposited geometry becomes essential for achieving "first-time-right" manufacturing and reducing process variability.

Recent work by Versteege [44] introduced a data-driven framework for continuous geometric monitoring of printed layers. Using two 2D laser triangulation scanners mounted directly behind the nozzle of TU/e's large-scale gantry printer, high-resolution profiles of the freshly extruded filament were captured in real time; one scanner measuring the top surface and the other the visible side surface (see Fig. 2.17). From these dense point clouds, the study derived a compact set of geometric features using knowledge-driven feature engineering (KDFE). Features were defined across multiple length scales: (i) single-layer descriptors such as layer width, height, and interface position; (ii) multi-layer characteristics including cross-sectional area, volumetric flow estimation, and progressive deformation; and (iii) surface-texture metrics such as roughness and fractal dimension. In total, 23 features were extracted from continuous measurements of two 2 m-long printed walls, with deliberate variations in nozzle speed and process interruptions clearly reflected in the feature evolution. This demonstrated the sensitivity of in-line sensing to real process fluctuations.

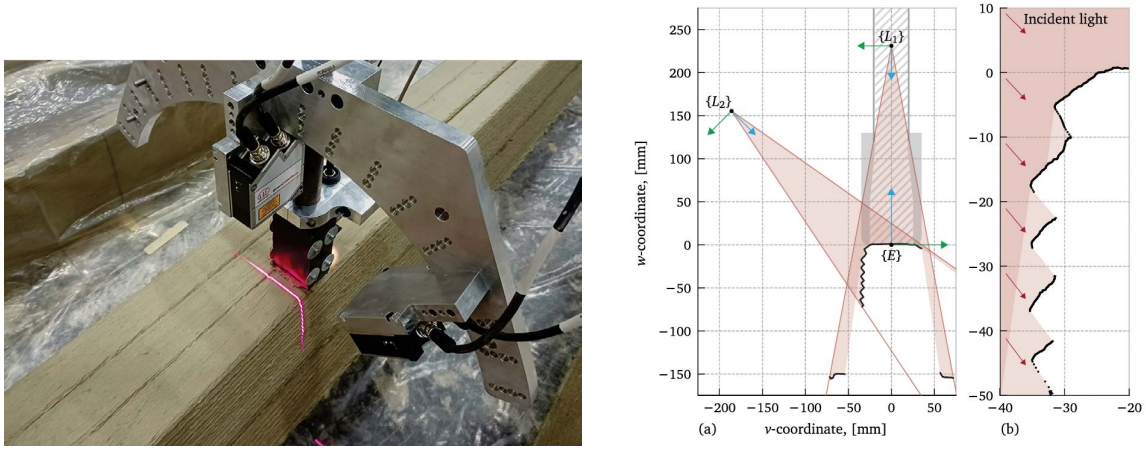

Figure 2.15: Setup of dual laser triangulation scanners mounted 40 mm behind the nozzle centreline, measuring the as-printed layer geometry as the nozzle moves from left to right. Images from [44].

As discussed in [27], the geometric conformity of a printed structure can be quantified across several scales, including:

- surface roughness and small-scale defects on the top or side of the filament,
- the initial width and height of a single deposited layer,
- the cross-sectional area of one or multiple layers,
- progressive deformation or lateral spreading of deposited layers,

- and the instantaneous distance between the nozzle and the previously printed layer.

These indicators can be extracted by post-processing continuous in-line sensor data obtained during printing. Beyond geometric conformity, such indicators can also serve to infer process- or material-related properties. For instance, combining the measured cross-sectional area with printing speed enables calculation of the volumetric flow rate, while monitoring the progressive deformation of an unsupported wall can yield indirect estimates of early-age material stiffness.

In-line process monitoring with non-destructive sensors

Beyond geometric monitoring of the printed filament, a broad range of non-destructive in-line sensors can be employed to characterise the *process* itself. These measurements target key quantities such as pressure, flow rate, material temperature, and motor torque or electrical power [30], as well as tracer concentration in the fresh concrete stream (discussed below). Together, these signals provide valuable insight into pumpability, extrudability, residence time and thermal history, forming an essential link between fresh-state material behaviour and the operation of the mechanical system.

Pressure, flow, and pump power

During extrusion, the material is transported and pressurised by a pump, typically a progressive cavity pump. In-line pressure sensors in the hose or at the pump outlet, combined with flow-rate measurements, provide direct information about the hydraulic loading of the system and the apparent resistance to flow. Nerella et al. [30] developed a dedicated 3D-printing extrudability test device (3DPTD) equipped with a progressive cavity pump driven by an asynchronous motor and frequency converter. The rotational speed of the pump was synchronised with the printhead velocity using dimensionless control parameters, while the electrical power consumption was recorded as a function of pump speed and operating conditions. From these measurements, a *unit extrusion energy* (UEE) was defined as the electrical energy consumed per unit volume of extruded material. UEE provides a quantitative measure of extrudability: lower UEE values indicate easier extrusion at a given flow rate. The authors demonstrated that two mixes with similar yield stresses nonetheless exhibited markedly different UEE values, underscoring both the sensitivity of the approach and the importance of system-specific characterisation. In-line monitoring of pressure, flow, torque and power therefore offers a practical means to detect variations in material consistency, pump wear, blockages or suboptimal operating conditions, and can be integrated into feedback or alarm systems.

Residence time and tracer experiments

For digitally fabricated concretes, the material properties at the nozzle are determined not only by the mix design but also by the *path* taken through the system: mixing, pumping, shearing, waiting and possible acceleration. This coupling between material and process can be quantified using the *residence time distribution* (RTD), which describes the frequency distribution of times that material elements spend

inside the system [13, 45]. RTD provides a powerful metric for comparing pump–hose–nozzle configurations, understanding why certain material–system combinations perform well, and supporting scale-up from laboratory systems to industrial equipment. Because RTD is often difficult to predict analytically, tracer experiments are commonly used. A tracer (radiotracer, pigment or dye) is injected at a known time and location in the system, and its concentration is monitored at the outlet [46]. The resulting time-resolved tracer signal yields the RTD. Earlier demonstrations used radiotracer techniques or offline pigment analysis, but these methods are either costly, labour-intensive or have low sampling rates. To address these limitations, Deetman et al. [13] developed an in-line dye tracer experiment for concrete processing using a low-cost industrial camera and digital image processing. This approach enables high sampling rates with minimal manual effort, lowering the barrier to widespread adoption. Although the method primarily traces the water phase and requires homogenisation of the filament before detection, it demonstrates that RTD can be measured in-line at high temporal resolution, making it suitable for integration into automated workflows for process and quality control.

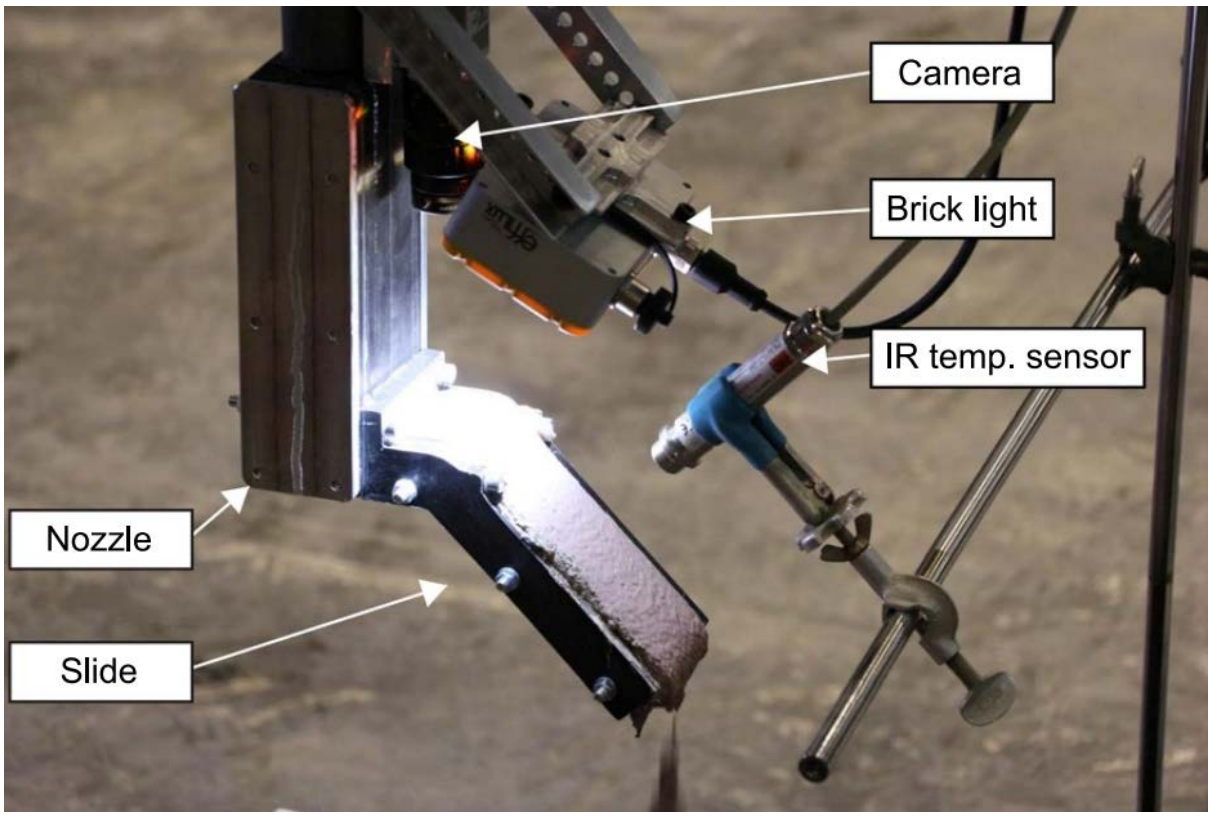

Figure 2.16: Polarized camera, polarized brick light, infrared temperature sensor and nozzle with slide mounted at the printhead, taken from [13].

Temperature and thermal history

The temperature evolution of printed concrete strongly influences hydration kinetics, stiffness development and early-age strength. Non-contact infrared (IR) thermography provides a means to estimate the surface temperature of printed elements by interpreting radiated energy through Planck's law, assuming appropriate emissivity and reflectivity. As described by Wolfs et al. [27], IR thermography can

be used to derive a maturity index. Such information is valuable for estimating the structural readiness of printed components—for example, determining when an element can be handled, moved or loaded.

Experimental work suggests that thermography is particularly suitable for thin concrete members in controlled environmental conditions, and may reduce the need for invasive thermocouples [27]. However, maturity concepts were originally developed for longer timescales (days to months), and their applicability within the time frame of 3DCP (minutes to hours), especially for accelerated 1K or 2K systems, must be evaluated carefully on a case-by-case basis.

Moreover, recent work by Versteege et al. [47] demonstrates that combining IR thermography with additional in-line sensors, for example, near-infrared (NIR) spectroscopy for moisture detection and environmental sensors for ambient conditions, significantly enhances the reliability of print-site monitoring. By integrating thermal and moisture data, the system can detect both surface temperature evolution and surface dehydration during and immediately after printing; variables strongly correlated with interlayer bond strength and early-age hydration.

Figure 2.17: Near-infrared (NIR) camera on the left, and thermal camera on the right. Images from [47].

2.3 Hardened state

Hardened-state mechanical testing of 3D printed concrete requires adapted procedures that explicitly account for anisotropy, interlayer interfaces, and process-dependent material behaviour. The RILEM TC 304–ADC interlaboratory study (ILS) demonstrates that conventional test methods, scuh as compression, flexure, splitting tensile strength, and direct tensile strength, can be applied to 3D printed materials, provided that specimen extraction, loading orientation, and interface positioning are carefully controlled. The following subsections briefly introduce the relevant test methods and specimen preparation considerations, and also some of the main conclusion/consideration from the TC304 ADC ILS-mech. A more detailed overview is provided in [48, 49].

2.3.1 Compression tests

Compression tests for 3D printed concrete follow conventional cube or cylinder procedures, but specimen preparation is fundamentally different due to the layered architecture. Cubic specimens (typically 40×40×40 mm) or small cylinders are sawn from printed walls, ensuring regular geometry and parallel load-bearing faces. To capture anisotropy, specimens are loaded in all three principal directions (often refered to as u-, v-, and w-direction) corresponding to along-layer, across-layer, and through-layer loading. Importantly, the horizontal interlayer interface is positioned at mid-height of each specimen, as required in the RILEM study plan, enabling systematic evaluation of interface weakness. Because material properties vary with print height, three specimens from bottom, middle, and top of the print wall are tested to assess vertical variability. Results in the interlaboratory study show printed specimens generally achieved 80–90 % of cast compressive strength on average, with wide scatter linked to interface quality and printing system differences.

2.3.2 Flexural testing

Flexural behaviour is assessed through three-point or four-point bending on prismatic beams (40×40×160 mm). In printed concretes, flexure is highly sensitive to loading direction because different orientations introduce tension either within a filament, across filaments, or directly across interlayer interfaces. Therefore, RILEM requires testing in three configurations (v.u, u.w, and w.u) each aligning the tensile zone differently relative to the interlayers. Specimens are fully sawn to ensure straight edges and accurate spans. When the interlayer interface lies in the tensile zone (u.w orientation), flexural strength is significantly reduced, whereas orientations loading along filaments (v.u and w.u) often exceed cast-beam strength, sometimes reaching more than 120–140 % due to directional stiffening effects from extrusion. This demonstrates that flexural performance in printed materials is highly anisotropic and strongly governed by interface positioning.

2.3.3 Splitting tensile strength

Splitting tensile tests are performed on either cubes or cylinders, but unlike cast concrete, printed specimens require precise alignment of interfaces relative to the load line. The RILEM plan extends the standard orientation notation to three configurations to capture anisotropy in tension. Specimens are extracted by sawing or core-drilling, maintaining the horizontal interface at specimen mid-height when relevant. Because splitting tension induces tensile stresses perpendicular to the load, weak interlayers become dominant failure planes when aligned with the indirect tension direction. As in compression, three height levels in the printed object (bottom/middle/top) are tested to assess variability caused by different curing and loading histories during printing. Splitting tensile results show large scatter due to the sensitivity of this test to even small interface defects or misalignment during extraction.

2.3.4 Direct (uniaxial) tensile strength

Direct tensile tests provide the most fundamental measure of tensile capacity but are the most challenging experimentally. Prismatic or cylindrical specimens are gripped and loaded in tension in two orientations, u- and w-direction, chosen to test either along or across the layered structure. Because gripping introduces stress concentrations, specimen ends must be carefully sawn, aligned, and often surface-treated or capped to ensure uniform load transfer. As with other tests, the interlayer interface is positioned deliberately within the gauge length for the across-layer orientation. Failure typically localises at the interface when loaded across layers, revealing tensile adhesion properties; when loaded along layers, the intrinsic material cohesion dominates. Due to preparation complexity and alignment sensitivity, this test exhibited the highest variability in the ILS study done [48].

2.3.5 Elastic modulus

The elastic modulus is determined in compression following a modified EN 12390-13 procedure, using prismatic or cylindrical printed specimens with L/d between 2 and 4. Because stiffness is orientation-dependent, modulus is measured in both u- and w-directions, requiring careful alignment of interfaces and application of multiple load–unload cycles at controlled rates. Specimens must have precisely parallel end faces, typically achieved through grinding or capping, as E-modulus results are highly sensitive to misalignment and local crushing. At the end of the test, specimens are brought to failure, providing an additional compressive strength measurement. Across laboratories, printed specimens showed 86–91 % of the cast E-modulus depending on orientation, indicating that interlayer interfaces reduce stiffness even when not governing strength failure.

Chapter 3

Digital Design for 3D Concrete Printing

One of the major promises of 3D Concrete Printing (3DCP) lies in the design freedom it offers compared to traditional casting techniques. However, this expanded freedom also introduces new complexities in the design process. It requires a rethinking of how we approach the material, shifting from a reinforcement-first mindset applied in traditional concrete works to a concrete-first approach in initial 3D concrete printed projects, or perhaps finding a balance between the two. Although 3DCP unlocks unprecedented potential for form (i.e., geometric possibilities) and customization (i.e., variation between designs), realizing this potential effectively depends on the development of robust digital design and modeling tools. Parametric and rule-based modeling tools are essential in bridging this gap, allowing designers to systematically explore, control, and optimize the design potential of 3DCP.

3.1 Introduction to Digital Design in 3DCP

Digital design provides the foundation for 3D concrete printing (3DCP). Instead of designing for a (often rectangular) timber formwork, the designer creates a digital model that can be directly translated into fabrication data for the printer. The process links geometry, material, and process in a continuous digital chain, in which design intent, production parameters, and as-built information are increasingly treated as interdependent rather than sequential.

This digital approach fundamentally changes the design logic. Traditional casting relies on standardized formwork, which favors rectangular and repetitive shapes. In contrast, 3DCP removes this limitation and enables form freedom—that is, the ability to produce curved, irregular, or organic geometries without significant cost increases. However, this expanded freedom also introduces new challenges: designers must explicitly consider how geometry interacts with material behavior, printing parameters, and structural performance from the earliest design stages. To support this, structured data infrastructures are emerging that capture and link cross-disciplinary information on materials, equipment, and processing parameters across both fabrication and evolution phases. For example, Deetman et al. [50] propose an open database framework that systematically stores process- and time-dependent 3DCP data, improving reproducibility, quality control, and long-term performance

analysis while enriching digital product passports.

Digital fabrication and additive manufacturing further reshape the relationship between complexity, cost, and market volume. In conventional construction, the unit cost of a component increases sharply with geometric complexity because intricate shapes require wasteful, single-use formworks. In contrast, digital fabrication processes such as additive manufacturing exhibit a much flatter complexity–cost curve—often described as providing "complexity for free" (see Fig. 3.1). The intersection of these curves marks the break-even point at which digital fabrication becomes economically competitive with conventional methods. Ongoing research and technological development, including improved process monitoring and data-driven optimization, are expected to shift this break-even point toward lower complexity levels, enabling cost-effective production of a broader range of geometries.

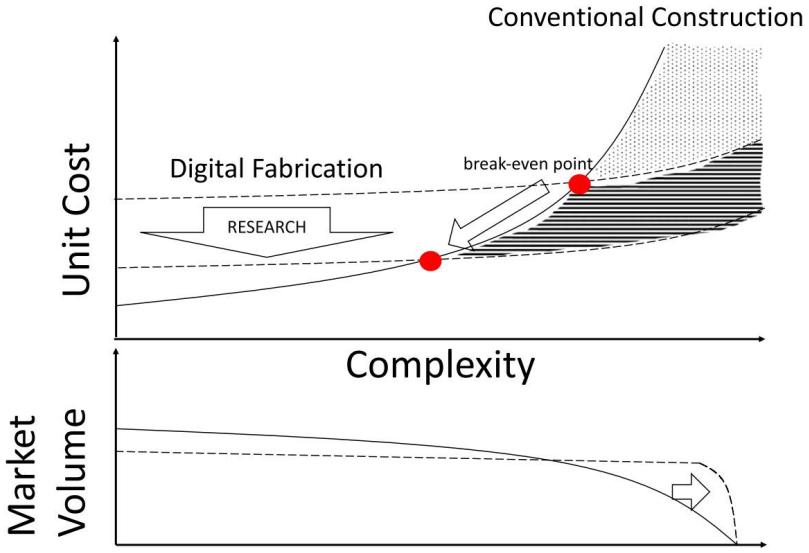

Figure 3.1: Schematic overview of the complexity-cost (top) and complexity-market volume (bottom) relationships for conventional construction (solid line) and digital fabrication (dashed line) methods. Taken from [7].

3.2 Different 3D Concrete Printing systems

The system architecture of extrusion-based 3DCP defines how material preparation, pumping, and robotic motion are coordinated into a single, controlled fabrication process. Two primary subsystems can be distinguished: the **material delivery system**, which prepares and pumps the printable mix from the silo or mixer to the nozzle under regulated pressure and flow rate; and the **motion control system**, which actuates the robotic mechanism (whether a Cartesian gantry, articulated arm, or hybrid configuration) to position the nozzle along the programmed toolpath with specified speed and orientation.

3DCP systems differ in their kinematic structure (number and type of motion axes) and their deployment mode (on-site versus factory-based printing). Specifically, cartesian gantries favor precision and scale, while robotic arms and hybrid systems

allow complex geometries and orientation control. The material-delivery subsystems are customized to the specific printable mix. For instance, progressive cavity pumps (rotor–stator pumps) and peristaltic pumps are both widely used, but each demands markedly different mix properties. Mixes with higher viscosity, coarse aggregates, or fibers require low-shear, high-pressure pumping to avoid clogging, segregation, or fiber alignment effects. Hose diameter, length, and pressure regulation strongly influence extrusion stability and layer uniformity.

Gantry type concrete printers — A widely used configuration in 3DCP is the Cartesian gantry system, which employs orthogonal X–Y–Z linear motion to position the printhead across a fixed build platform, as illustrated in Figure 3.2. Gantry printers, such as the Contour Crafting prototype and COBOD's BOD2, provide rigid, repeatable motion suitable for large-span, planar geometries. The COBOD BOD2, for example, can reach build dimensions of approximately 9 m in height and 12 m in width [51]. Such systems achieve millimeter positioning accuracy and high travel speeds, making them ideal for repetitive wall structures. However, their structural rigidity and size lead to high setup effort and limited geometric freedom—typically confined to near-vertical layer deposition. Gantries require stable, level foundations, which restricts their mobility.

Figure 3.2: Examples of Cartesian gantry-type 3D concrete printers. Left: a COBOD system configured for full-scale on-site printing [51]. Right: large-scale gantry at TU/e 3DCP research laboratory

Robotic Arm — Industrial robotic arms, seen on Figure 3.3 from manufacturers such as ABB and KUKA provide six or more degrees of freedom, enabling full spatial orientation of the print nozzle. They are well suited for producing curved, inclined, or overhanging geometries that are difficult to achieve with gantry systems. Theoretical workspace extends up to 360° around the base with a reach of approximately 2–3 m; however, effective coverage is constrained by hose and cable management requirements. While these systems offer superior geometric versatility and can integrate multi-tool operations—such as reinforcement placement or surface finishing—they are less efficient for large-scale structures, where the limited reach necessitates printing in smaller segments that are later assembled.

Figure 3.3: Left: ABB robotic arm mounted on a fixed base at Tallinn University of Applied Sciences used for educational and research-scale 3D concrete printing [52]. Right: KUKA robotic arm system at Hyperion Robotics in Finland used for automated fabrication of reinforced concrete elements [53].

Arm on Linear Track (7th Axis) — Mounting a 6-DOF robot on a linear track introduces an additional translational degree of freedom, seen on Figure 3.4, effectively extending the build envelope to tens of meters in one direction. This configuration combines the geometric freedom of an articulated arm with the reach of a gantry system. The approach allows continuous wall printing while maintaining flexible nozzle orientation.

Figure 3.4: Left: Robotic arm on linear track at Weber Beamix Print fabriek used for industrial-scale 3D concrete printing [54]. Right: Vertico print facility at TU/e featuring a KUKA robotic arm on a movable track for printing curved and overhanging geometries [55].

Hybrid Gantry + Arm or Rotary Table Systems — Some manufacturers have explored combining gantry with robotic arm dexterity, seen on Figure 3.5. In such systems, a gantry might carry a rotary platform beneath the nozzle, or a robotic arm might be mounted atop a mobile gantry frame. These hybrid architectures provide both extended reach and multi-axis motion, suitable for complex geometries that require varying print orientations. While they offer operational versatility, their mechanical complexity and higher control requirements increase cost and maintenance.

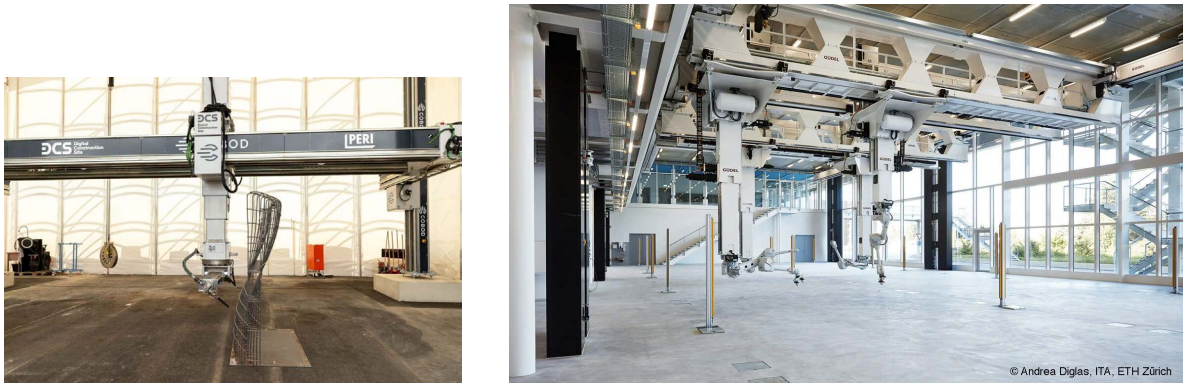

Figure 3.5: Left: COBOD BOD2 system at TU Braunschweig equipped with a vertical telescopic unit and rotating robotic arm enabling multifunctional printing and shotcrete (SC3DP) operations [56]. Right: ETH Zurich's Robotic Fabrication Laboratory (RFL) with an overhead gantry and four six-axis robots operating within a 43 × 16 × 8 m workspace [57].

Cable-Driven or Suspended Plotters — Cable-driven parallel robots (CDPRs) use multiple winches and tensioned cables to control the position and orientation of the printhead. This design drastically reduces moving mass, enabling large-scale and high-speed motion [58]. Tho and Thinh [58] demonstrated an eight-cable, six-DOF CDPR for house-scale printing, achieving high payload capacity and dynamic response. Earlier, Bosscher et al. proposed a "cable-suspended contour crafting" concept as a portable alternative to rigid gantries [59]. Despite their promise for scalability, CDPRs remain largely experimental; they demand precise cable-tension control and are sensitive to environmental disturbances such as wind.

Mobile or Vehicle-Mounted Printers — To enable on-site flexibility, several systems mount the printing module on a mobile base such as a skid, trailer, or truck. Notable examples include Putzmeister's truck-mounted KARLOS and Constructions-3D's mobile ABB-robot unit, capable of printing directly on construction sites without fixed support frames. Constructions-3D reports successful deployment over 2,500 m^2 of printed wall area at its French facility [60]. Mobile units are highly adaptable to uneven terrain and can be rapidly deployed, but they typically support smaller continuous build zones and require careful alignment and stabilization during operation.

Climbing or Rail-Attached Printers — Emerging "climbing" systems attach directly to the structure under construction, ascending layer by layer as the material cures. Some prototypes follow the "core-on-core" approach—printing within vertical shafts that act as their own support—while others use external rails. These concepts theoretically enable unlimited build height but remain in early research stages (low technology readiness level). The principal challenges involve maintaining geometric precision and dynamic stability while climbing.

Factory Cell (Off-site) vs. On-site Deployment — 3DCP can be implemented either within controlled factory environments or directly on construction sites. Factory-based (off-site) production enables consistent temperature and humidity, optimized material handling, and compact robotic cells that print smaller modules or façade panels. However, the resulting elements must be transported and assembled later. For example, COBOD notes that robotic-arm systems often fabricate panels off-site

due to workspace constraints, followed by mechanical joining [51]. In contrast, large gantry systems allow on-site printing of full-scale walls or buildings [51], eliminating joints but introducing environmental challenges such as wind or precipitation. The choice between off-site and on-site deployment thus depends on the balance between quality control, logistics, and architectural intent.

3.3 Design Considerations

This section outlines key design considerations for structures produced using extrusion-based 3D concrete printing (3DCP). The guidelines address geometric constraints, process-related limitations, physical boundaries, structural performance, and long-term durability. While specific printer capabilities and material properties may vary, the principles described here are broadly applicable to a wide range of 3D concrete printed structures, from small components to architectural-scale elements. It should be noted, however, that these considerations are intentionally generic and, in some cases, simplified; they may therefore require adaptation or refinement for specific applications, materials, or production setups.

3.3.1 Geometry and Printability

Self-supporting behavior during and after printing

All printed elements must be self-supporting throughout the entire printing process and after completion. Since 3DCP typically does not use conventional formwork, each layer must rely on the previously deposited layers for support. Geometries that require fresh concrete to span open air without support should be avoided. Ensuring continuous support prevents deformation under self-weight, reduces the risk of collapse during printing, and contributes to dimensional accuracy.

Overhangs and cantilevers

Large unsupported overhangs are generally not feasible in extrusion-based concrete printing. Limited overhangs can be achieved through gradual layer offsets, allowing short cantilevers to be formed incrementally. As a rule of thumb (for 1K systems), the inclination of an overhanging section should remain shallow (for example, within approximately 10-20 degrees from the vertical), and such sections should return to a supported geometry within a limited number of layers. Abrupt or extended cantilevers introduce high risk of slumping or collapse and should be avoided unless additional measures are taken, such as temporary supports.

Minimum wall thickness and feature size

The resolution of a 3D concrete printer is governed by nozzle diameter, layer height, and material rheology. Consequently, very thin walls, sharp edges, or delicate features are not printable. All load-bearing or functional elements should have a thickness at least equal to one continuous extrusion bead, and preferably multiple beads where structural capacity is required. As a general guideline, geometric details should be larger than both the nozzle diameter and the layer height. Very

small voids, narrow gaps, or thin projections are likely to be filled unintentionally or to fail during printing.

Continuous layer logic and build sequence

Designs should be conceived as a continuous, bottom-up construction process. Each layer must be fully supported by the previous one, and the toolpath typically follows closed or continuous trajectories. Openings and voids require particular attention: vertical openings can be printed by continuously routing layers around them, while horizontal closures are only possible if the geometry itself provides self-support (e.g., arches or vaults). Designers should carefully consider the printing sequence to ensure that every stage of the build is feasible (preferably without temporary supports).

Geometric resolution and detailing

The layer-based nature of 3DCP favors smooth, gradual transitions over sharp edges and abrupt geometric changes. External corners should be rounded, as the finite width of the extruded bead limits the achievable sharpness. A minimum fillet radius proportional to the layer width is recommended to ensure smooth toolpaths and consistent material deposition. Internal corners should also be slightly rounded to allow reliable nozzle movement. Designs that embrace curves and continuous surfaces generally align better with the strengths of 3D concrete printing.

3.3.2 Process Constraints

Automated printing without manual support

Once printing has started, the process is typically automated and should not rely on manual intervention to maintain stability or correct geometry. Designs must therefore remain stable at every intermediate stage of printing, without the need for external bracing, formwork, or manual correction. Slender, top-heavy, or highly unbalanced geometries may be prone to instability before sufficient material strength has developed and should be treated with caution.

Integration of reinforcement

In certain cases, reinforcement may be necessary to meet structural performance requirements, particularly for elements subjected to bending, tension, or torsion. The printing process may allow for planned pauses during which reinforcement such as steel bars or meshes can be inserted. If reinforcement is used, the design must include dedicated channels or cavities that respect required concrete cover and do not compromise printability. Pauses should be minimized to avoid weak interfaces between layers, and the reinforcement strategy should be integrated from the earliest design stages.

3.3.3 Physical and Practical Limitations

Printer workspace and modularization

All printed elements must fit within the operational envelope of the available printing system, including limits on footprint and height. If a structure exceeds these limits, it must be subdivided into smaller modules that can be printed separately and assembled afterward. In such cases, joint design, alignment features, tolerances, and assembly logic become critical aspects of the overall design. Additionally, the movement range of the printing system and potential collision risks must be considered when printing multiple elements within the same workspace.

Weight, handling, and transportation

The mass of printed components influences not only structural behavior but also handling, transportation, and assembly. Designs should account for safe lifting and positioning by considering the center of gravity and providing suitable lifting points or geometries compatible with slings, hooks, or forklift blades. An unbalanced center of gravity can lead to unsafe handling conditions or damage during transport, and should therefore be addressed explicitly in the design.

Height-to-print-path length relationship

The achievable height of a printed element is related to the total print path length and the resulting build time. Taller elements typically require longer, continuous print paths to ensure sufficient material buildup, interlayer bonding, and early-age stability. Designers should recognise that vertical slenderness and rapid height accumulation can compromise stability, and should adjust geometry or printing strategy accordingly. Section 3.5 shows detailed methods how to analyse this aspect, however, during brainstorming/design competitions, simple graphs such as shown in Fig. 3.6 can really be helpful for a broad first understanding.

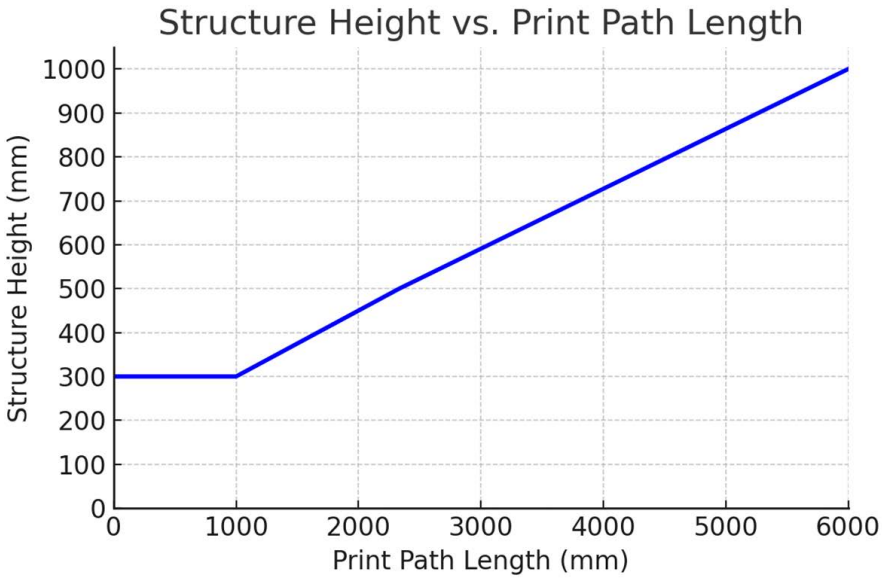

Figure 3.6: Exploratory height-to-print-path length relationship for brainstorming/ design competitions.

3.3.4 Structural Performance

3D concrete printed structures must be designed to safely resist all relevant loads throughout their intended service life. Particular attention should be given to regions subjected to tensile stresses, such as horizontal spans, cantilevers, or connections between elements. Geometry should promote efficient load paths and minimize stress concentrations. Where necessary, reinforcement or increased cross-sectional dimensions should be used to enhance load-bearing capacity. In applications subject to dynamic or accidental loads, such as impacts or vibrations, additional robustness is required to prevent brittle failure.

3.3.5 Durability and Long-Term Behavior

Durability is a critical consideration, especially for structures exposed to outdoor or variable environmental conditions. Moisture ingress, freeze-thaw cycles, thermal gradients, shrinkage, and differential curing can all lead to cracking or surface degradation. Designs should therefore encourage water drainage, avoid deep crevices, and maintain relatively consistent wall thicknesses. Smooth geometric transitions help reduce stress concentrations associated with thermal and shrinkage movements. By anticipating environmental exposure and material behavior over time, designers can ensure that 3D concrete printed structures maintain both structural integrity and aesthetic quality throughout their lifespan.

3.4 Design tools

There are many ways to design 3D concrete-printed structures, but because the technique enables the creation of complex and unique geometries, parametric design is often the preferred approach. One of the most widely used tools in this context

is Rhinoceros combined with Grasshopper. In-depth introductions and tutorials of Grasshopper can be found on [61].

This section highlights a selection of Grasshopper plug-ins that can significantly simplify the workflow or broaden the design possibilities. The list is by no means complete and should be viewed as a first glance at the available tools rather than a comprehensive overview.

3.4.1 Grasshopper

Grasshopper originated as a visual programming environment integrated into Rhinoceros, created to give designers a flexible, intuitive way to build parametric models without traditional coding. Over time it has evolved into a powerful ecosystem widely used in architecture, engineering, and digital fabrication, including 3D concrete printing. Its node-based workflow allows users to rapidly iterate, automate geometry generation, and link design directly to fabrication processes. Because of its open structure, a vast library of plug-ins has emerged, extending Grasshopper's capabilities far beyond its core tools. In the following section, we introduce three such plug-ins (i.e., Robot Components, Salad Slicer, and Karamba3D) that play an important role in bridging design and fabrication. Most plug-ins are available through the Food for Rhino marketplace at https://www.food4rhino.com/browse [62].

Grasshopper is supported by a large and active user community, resulting in a wide range of high-quality tutorials and learning resources available online. For this reason, this teaching material does not go into depth on Grasshopper fundamentals or general workflows. A practical starting point for finding tutorials that align with specific project goals and experience levels can be found through the official Rhino learning platform, which curates Grasshopper-related resources [63].

Salad Slicer

Summary
Salad Slicer [64] is an open-source plug-in for the Grasshopper environment inside Rhinoceros. It was originally created to prepare models for 3D concrete printing, but the same methods work just as well for other printable materials, including ceramics and polymers. The plugin introduces several tools that help you understand and control how a digital model is transformed into printable layers.

Salad Slicer can generate slices from simple 2D curves, producing a stack of flat layers in a process commonly referred to as 2.5D slicing. In this approach, the object gains thickness while each individual layer remains planar, making it ideal for straightforward fabrication tasks. When working with full 3D meshes, the plug-in can divide the geometry into a series of horizontal sections, forming the foundation for most layer-by-layer fabrication workflows. Beyond the built-in tools, Salad Slicer enables users to assemble custom slicers using components from the Geometry section, which helps in understanding the slicing algorithms and adapting them to special cases. Once the geometry is sliced, the software can translate the layers into numerical control (G-code) instructions that printers or CNC machines can follow.

Additionally, all slices can be converted into planar data for robotic workflows, allowing the creation of motion paths for industrial robots such as those from ABB or KUKA.

Functionality
The Salad Slicer plug-in is organised into eight tabs. An overview of these tabs is provided below:

- Code Generation
  The Program Generator is likely the most frequently used component in this category. It converts all slicer objects into executable robot or machine code. Currently, Sinumerik and Marlin formats are supported, with the option to add other formats as needed. Printer settings itself can also be configured in this tab with the 'printer settings' component, including the selection of either Sinumerik or Marlin as the target output.
- Deconstruct
  Deconstruct components allow users to unpack the generated slicing path from either the built-in slicers or any customized slicer setup.
- Geometry part 1
  Focuses on creating the geometric inputs that will later be processed by the slicer.
- geometry part 2
  Covers the specific parameters that influence how geometries are sliced, including control over features such as seam location and seam length during printing.
- Nozzles
  A selection of predefined parametric nozzles available for use in printing.
- Parameters
  Basic input parameters for Salad Slicer.
- Slicers
  This tab contains all slicers, with the most notable being: 'Closed Planar 2.5D Slicer', 'Closed Planar Mesh Slicer', 'Open Planar 2.5D Slicer', and 'Open Planar Mesh Slicer'. In which 'open' and 'closed' refers to the back-and-forward (e.g. single-layer wall) and continuous direction print path (e.g. circular shape), respectively.
- Utilities
  A handy set of utility tools, for example to convert units.

Example files
The example files for Salad Slicer can be found on [64], an overview of all example files of the current latest version (V0.5) is shown below:

```
Example Files
├── 01_Planar_2D_Slicer
├── 02_Planar_2D_Slicer_multiple_objects
├── 03_Planar_3D_Slicer
└── 04_Planar_2D_Slicer_FDM_printing
```

```
├── 05_Nozzles
└── Robot Components
    ├── RC_01_Planar_2D_slicer
    └── RC_02_Planar_2D_slicer_multiple_objects
```

License
The following license notice is provided by the developers of Salad Slicer [64]:

> Copyright (c) 2021-2025 3D Concrete Printing Research Group at Eindhoven University of Technology
>
> Salad Slicer is free software; you can redistribute it and/or modify it under the terms of the GNU General Public License version 3.0 as published by the Free Software Foundation.
>
> Salad Slicer is distributed in the hope that it will be useful, but WITHOUT ANY WARRANTY; without even the implied warranty of MERCHANTABILITY or FITNESS FOR A PARTICULAR PURPOSE. See the GNU General Public License for more details.
>
> You should have received a copy of the GNU General Public License along with Salad Slicer; If not, see http://www.gnu.org/licenses/.
>
> @license GPL-3.0 https://www.gnu.org/licenses/gpl-3.0.html

Robot Components

Summary
Robot Components [65] is a plug-in for the Grasshopper environment inside Rhinoceros, designed to introduce users to industrial robot programming in a visual, hands-on way. The plugin allows exploration of robot motion, path planning, and code generation without requiring prior expertise in robotics.

Robot Components provides a library of more than forty pre-configured robot models, giving an immediate starting point for experimentation with different sizes, reaches, and capabilities. For specialised scenarios, users can also import or create custom robot setups, bridging the gap between digital modelling and physical hardware. The software supports additional axes such as linear tracks and rotary tables, expanding the effective workspace of robot cells and allowing exploration of coordinated motion strategies.

Finally, Robot Components can connect to real ABB IRC5 and OmniCore controllers, enabling live testing and adjustment of programs on physical robots. The plugin thus provides a seamless path from geometric modelling in Grasshopper to executable robot programs, making it a versatile tool for both exploration and experimentation.

Functionality
The Robot Components plug-in is organised into eight tabs. An overview of these tabs is provided point-wisely below:

- Code Generation
  The RAPID program, containing all robot instructions such as target definitions and motion commands, is created with the 'RAPID Generator' component in this

tab, while specific movement actions can also be defined using other components in the same tab.

- Controller Utility
  The components in this tab link a physical ABB IRC5 robot controller to the virtual design environment.
- Deconstruct
  Deconstruct components allow users to unpack variables such as the robot tool and or a robot target back into their parameters.
- Definitions
  This tab contains components that allow users to select and preview the robot, define presets, set tools, and create work objects.
- Multi Move
  Extension of the Code generation tab with components specifcally needed for set-ups with mutliple moving robotic parts.
- Parameters
  Basic input parameters for Robot Components.
- Simulations
  Contains forward and inverse kinematic components and a component for visualisation purposes of the print path.
- Utility
  A handy set of utility tools, for example, to flip planes.

Example files
The example files for Robot Components can be found on [65], an overview of all example files of the current latest version (V3.2) is shown below:

```
Example Files
├── 0.Basic
│   ├── BASIC_01_Tool_mount_example
│   ├── BASIC_02_Move_along_curve
│   ├── BASIC_03_Simple movements
│   ├── BASIC_04_Setup_of_external_linear_axis
│   ├── BASIC_05_Setup_of_robot_info_IRB120
│   ├── BASIC_06_Circular_movements
│   └── BASIC_07_Casting_methods
├── 1.Advanced
│   ├── ADVANCED_01_Pick_and_place_general_example
│   ├── ADVANCED_02_Work_object_example
│   ├── ADVANCED_03_Override_external_axis_values_example
│   └── ADVANCED_04_Stationary_tool
├── 2.Expert
│   ├── EXPERT_01_Movable_work_object_example
│   └── EXPERT_02_Multi_move_with_synced_movements
└── 3.Calibration
    ├── CALIBRATION_01_Tool
    └── CALIBRATION_02_External_rotational_axis
```

```
    └── CALIBRATION_03_Multi_move_two_robots
└── 4.API programming
    ├── API_01_Python
    └── API_02_C#
```

License
The following license notice is provided by the developers of Robot Components [65]:

> Copyright (c) 2018-2020 EDEK Uni Kassel Copyright (c) 2020-2024 Arjen Deetman
>
> Robot Components is free software; you can redistribute it and/or modify it under the terms of the GNU General Public License version 3.0 as published by the Free Software Foundation.
>
> Robot Components is distributed in the hope that it will be useful, but WITHOUT ANY WARRANTY; without even the implied warranty of MERCHANTABILITY or FITNESS FOR A PARTICULAR PURPOSE. See the GNU General Public License for more details.
>
> You should have received a copy of the GNU General Public License along with Robot Components; If not, see http://www.gnu.org/licenses/.
>
> @license GPL-3.0 https://www.gnu.org/licenses/gpl-3.0.html

Karamba3D

Summary Karamba3D is a structural analysis plug-in for the Grasshopper environment inside Rhinoceros, designed to make structural behavior directly accessible within parametric modeling workflows. It enables users to study how digital geometry responds to forces, materials, and boundary conditions without leaving the visual programming environment.

Karamba3D allows loads such as self-weight, wind, and point forces to be applied directly to geometric models, providing immediate insight into how forces flow through structures. Users can define beams, shells, trusses, and hybrid systems, assign supports and materials, and explore how different design decisions affect stability, stiffness, and overall performance. The software visualizes deformation, displacement, and internal stresses through diagrams and color maps, revealing where structures bend, stretch, or concentrate stress.

Because it operates parametrically inside Grasshopper, Karamba3D encourages experimentation with thicknesses, cross-sections, material properties, and geometric variations. It also integrates seamlessly with optimization tools, enabling workflows for minimizing weight, maximizing stiffness, or improving structural efficiency. Real-world materials (such as steel, timber, concrete, or custom definitions) can be assigned to evaluate authentic structural behavior.

Karamba3D can export analysis results and geometry for engineering workflows, making it a versatile bridge between conceptual modeling, structural understanding, and professional documentation.

Functionality

The Robot Components plug-in is organised into ten tabs. An overview of these tabs is provided point-wisely below:

- Settings
  Contains a license information component.
- Params
  Basic input parameters for Karamba3D.
- 1.Model
  Components for building the structural model, including elements, supports, and assembling the analysis model.
- 2.Load
  Tools for defining loads on the structure, such as forces, moments, gravity, and load cases.
- 3.Cross Section
  Parametric tools for creating, modifying, and assigning cross sections to structural elements.
- 4.Joint
  Components for defining joints, releases, and connection behavior between structural elements.
- 5.Material
  Tools for selecting and defining materials, including steel, concrete, timber, and custom material properties.
- 6.Algorithms
  Advanced tools for optimization, form-finding, eigenvalue analysis, and other algorithmic processes.
- 7.Results
  Components for extracting, visualizing, and interpreting analysis results such as displacements, internal forces, stresses, and utilization.
- 8.Export
  Tools for exporting structural models and results to external formats.
- 9.Utilities
  General helper tools for data management, model inspection, conversion, and workflow support.

Example files
The example files for Karamba3D can be found on [**?**], an overview of the most relevant examples for 3DCP (i.e., examples that can help somewhere in the designing stage of 3D printed concrete) is listed below:

```
Example Files
└── Simple
    ├── Bracing Walls (SIMPLE)
    ├── Simple Shell (SIMPLE)
    ├── Optimize Cross Section Freeform Shell (SIMPLE)
    └── Cross Section Optimization Spline (SIMPLE)
```

- Principal Moments as Ribs (SIMPLE)
- Pointloads on a Shell (SIMPLE)
- Element Set with Shells (SIMPLE)
- Moving Pointload on a Cantilever (SIMPLE)
- Element Sets in a Beam Grid (SIMPLE)
- Simple Frame (SIMPLE)
- Shell Cross Section Optimization (SIMPLE)
- Optimization of Support Positions (SIMPLE)
- Input Surfaces and Analyse as a Shell (SIMPLE)
- Single Span Beam (SIMPLE)
- Simple Supported Beam (SIMPLE)
- Optimization of Truss Diagonals (SIMPLE)
- Simple Beam (SIMPLE)

Medium Simple

- Parametric Shell and Columns (MEDIUMSIMPLE)

Medium

- Principal Stress Lines To Curve (MEDIUM)
- Leaf Growing 2D Agents (MEDIUM)
- BESO on a 3D network of Lines (MEDIUM)
- 3D Objects to Shell (MEDIUM)
- CFD Cube (MEDIUM)
- Shell Ribs (MEDIUM)
- Temperature Load on Beams (MEDIUM)
- Simple Structure - Shells and Beams (MEDIUM)
- Principal stress Lines to Mesh (MEDIUM)
- Curved Glass (MEDIUM)
- Cross Section Optimization of Shells (MEDIUM)
- Beso Tower (MEDIUM)
- Membrane Form Finding (MEDIUM)
- Input Any Shell (MEDIUM)
- Shell and Beams (MEDIUM)
- Force Flow Lines (MEDIUM)
- Buckling Simulation for 3D Printing in Fresh Concrete (MEDIUM)
- Input Surface and Analyze Structure (MEDIUM)
- Input Curves and Analyze Structure (MEDIUM)
- Optimization of a Shell Bridge (MEDIUM)
- BESO of Bracing Wall (MEDIUM)
- Optimization of an Irregular structure (MEDIUM)
- Cross Section Heights from Moments (MEDIUM)
- High Rise Systems (MEDIUM)

Moderate

- Cross Section Optimization of Shell Patches (MODERATE)
- Modular Beso Spatial Truss (MODERATE)

Hard

- Find Material Distribution (HARD)
- Smooth Cross Section Heights from Moments (HARD)
- Set Smart modules (HARD)
- Optimization of Column Positions (HARD)

```
Large Deformation of a Shell (HARD)
projected Array of Lines (HARD)
projected Voronoi Pattern Gridshell (HARD)
Large Deformation of a triangular Grid (HARD)
Large Deformation of a Voronoi Gridshell (HARD)
Informed Geometry - Scale Openings by Inner Forces (HARD)
```

License
Karamba3D is a commercially available software [66], and there are also more affordable educational versions available for students and teaching purposes.

3.5 Printable design

In 3D concrete printing, the structure is built up layer by layer while the concrete is still in its fresh, workable state. Because of this, the behaviour of the object during printing can be very different from its performance once the concrete has hardened. The fresh material has low stiffness and strength, which means that failures such as elastic buckling and plastic collapse can occur before the object is even completed (see Fig. 3.7). Plastic collapse and elastic buckling occur because the fresh, low-stiffness material cannot carry the increasing loads during printing, causing it to fail either by losing stability (buckling) or by exceeding its strength capacity (plastic collapse) [39, 40, 16]. In this section, the mechanics-based parametric model developed by Suiker [39] is introduced, followed by a discussion of a Finite Element Modelling approach for these failure modes.

3.5.1 Suiker's model

The two failure modes, elastic buckling and plastic collapse, can be described using five dimensionless parameters. Dimensionless parameters are used to simplify complex physical problems by removing units, allowing us to compare different materials, scales, and conditions on a single universal basis. This makes results easier to generalise, interpret, and apply across a wide range of printing scenarios. The elastic buckling failure can be described using three dimensionless parameters: the

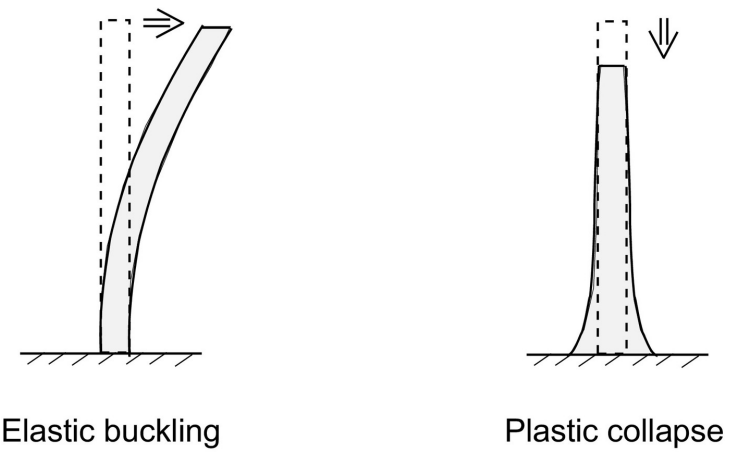

Figure 3.7: Elastic buckling (left) and plastic collapse (right). Taken from [40].

dimensionless critical buckling length ($\bar{l}_{cr}$), the dimensionless wall width ($\bar{b}$), and the dimensionless curing rate of the elastic stiffness ($\bar{\xi}_E$):

$$\bar{l}_{cr} = \left(\frac{\rho g h}{D_0}\right)^{1/3} l_{cr}, \tag{3.1}$$

$$\bar{b} = \left(\frac{\rho g h}{D_0}\right)^{1/3} b, \tag{3.2}$$

$$\bar{\xi}_E = \left(\frac{D_0}{\rho g h}\right)^{1/3} \frac{\xi_E}{\dot{l}}, \tag{3.3}$$

More detail about the background of these dimensionless parameters is described in the original work by Suiker [39] in which the entire derivation to achieve these dimensionless parameters is described. In a general sense the first dimensionless parameter, the dimensionless critical buckling length, provides information about the length (in the field of 3DCP often referred to as the 'height' of the wall) at which buckling failure will occur. Note that the l_{cr} gives the exact length (i.e., the 'height' of the wall in 3DCP context) at which elastic buckling takes place. The second dimensionless parameter, the dimensionless wall width, says something about the width (i.e., often referred to as the 'length' in 3DCP context) of the wall under investigation. The exact width (i.e., 'length') of the wall is given by b. The last dimensionless parameter related to the elastic buckling failure mode, the dimensionless curing rate of the elastic stiffness, is related to as the name already suggest the development of elastic stiffness over time. The real curing rate for the elastic stiffness (ξ_E), can be determined based on experimental test series of uniaxial compression tests with concrete experiencing different curing times, see also Chapter 2 for more information about the uniaxial compression test. Fig. 3.8 shows the resulting stiffness's obtained by doing uniaxial compression testing on Weber 3D 145–2 printable material tested at curing times of 5, 15, 30, and 60 minutes [40]. Based on these test results, a linear approximation of stiffness development over time can be made using the following Equation:

$$E(t) = E_0 + (E_0\,\xi_E)\,t, \tag{3.4}$$

in which the initial stiffness is given by E_0, which can be determined from the point at which the linear approximation crosses the vertical axis ($E_0 = 48.564$ [kPa] =). The curing rate for the elastic stiffness can then be calculated as follows:

$$\xi_E = \frac{E_0\,\xi_E}{E_0} = \frac{\text{slope}}{E_0} = \frac{2.609}{48.564}\ \text{min}^{-1} = 8.954 \times 10^{-4} s^{-1}.$$

Similarly, the plastic collapse failure can be described using two dimensionless parameters: the dimensionless collapse length ($\bar{l}_p$), and the dimensionless curing rate of the yield strength ($\bar{\xi}_\sigma$):

$$\bar{l}_p = \frac{\rho g}{|\sigma_{p,0}|}\, l_p, \tag{3.5}$$

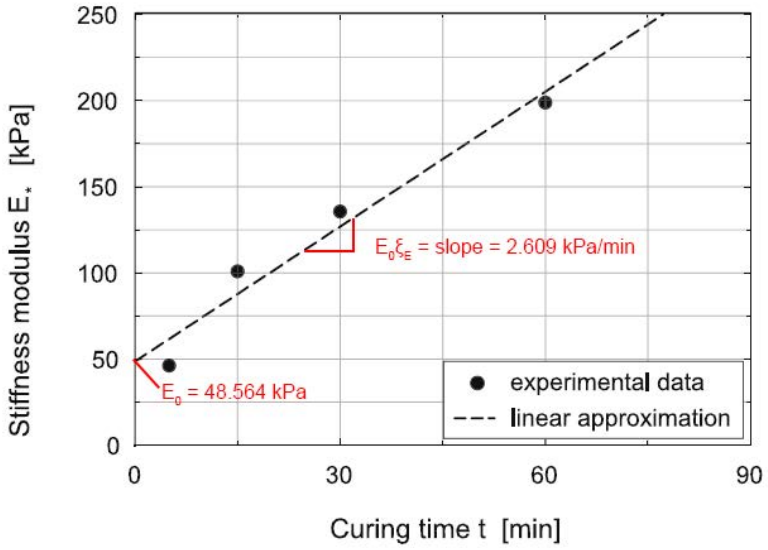

Figure 3.8: Stiffness modulus development for Weber 3D 145–2 printable mortar. Taken from [40].

$$\bar{\xi}_{\sigma}^{l} = \frac{|\sigma_{p,0}|}{\rho g \dot{l}} \xi_{\sigma}. \tag{3.6}$$

The first dimensionless parameter, the dimensionless collapse length, provides information about the length (i.e., often referred to as 'height' in 3DCP context) at which the wall will fail due to plastic collapse. The exact height at which this failure mechanism will take place is described with l_p. The second dimensionless parameter, the dimensionless curing rate of the yield strength, is related to the strength development that the freshly printed concrete will have over time. The real curing rate of the yield strength is given by ξ_{σ} and can be determined similarly as the stiffness curing rate, see Fig. 3.9 and Eq. 3.7.

$$\sigma_{p*}(t) = \sigma_{p,0} + (\sigma_{p,0}\,\xi_{\sigma})\,t \tag{3.7}$$

Resulting in the following calculation of the curing rate of the yield strength:

$$\xi_{\sigma} = \frac{\sigma_{p,0}\,\xi_{\sigma}}{\sigma_{p,0}} = \frac{\text{slope}}{\sigma_{p,0}} = \frac{0.329}{2.835}\ \text{min}^{-1} = 1.934 \times 10^{-3} s^{-1}.$$

Suiker's model can also be applied during the design phase of an element. Using this model, various design graphs have been developed for simply supported walls (see Fig. 3.10) and fully clamped walls (see Fig. 3.11). Note that both design graphs also include the results for a free-standing wall. These design graphs together with the dimensionless parameters can be used to determine the failure mechanism and failure length (i.e., 'height'). This will be shown with the example provided in [40] of two different-sized squares which were printed until failure occurred. The design of the squares can be seen in Fig. 3.12.

First, it is necessary to identify the relevant structural scheme for the object under investigation. In this case, the options are a free-standing wall (i.e., not laterally supported in any way), a simply supported wall, or a fully clamped wall (see Fig. 3.13).

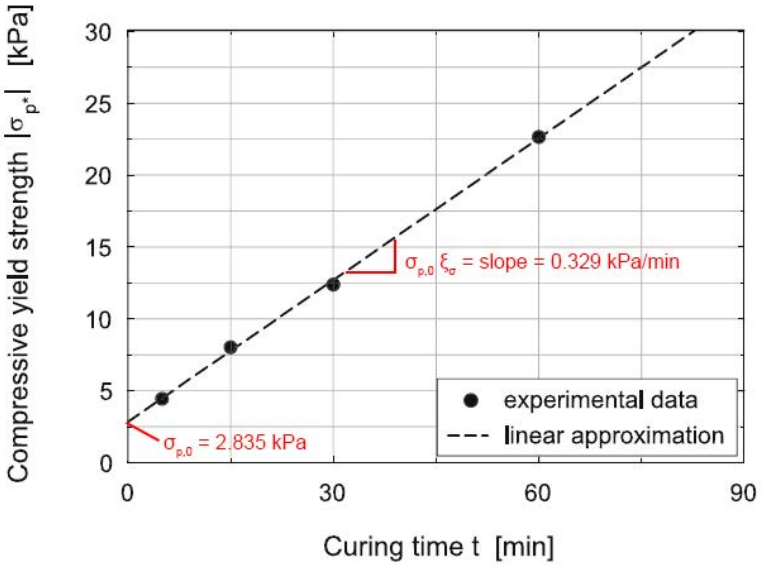

Figure 3.9: Compressive strength development for Weber 3D 145–2 printable mortar. Taken from [40].

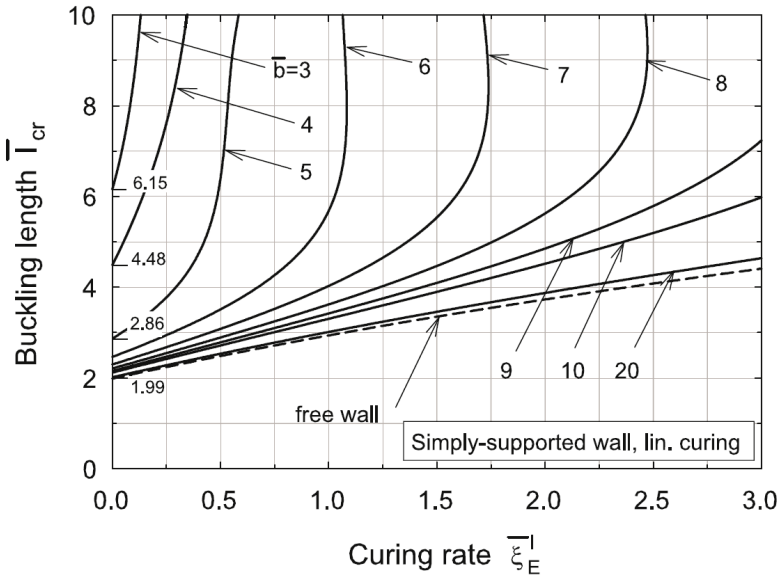

Figure 3.10: Design graph simply supported wall. Taken from [39].

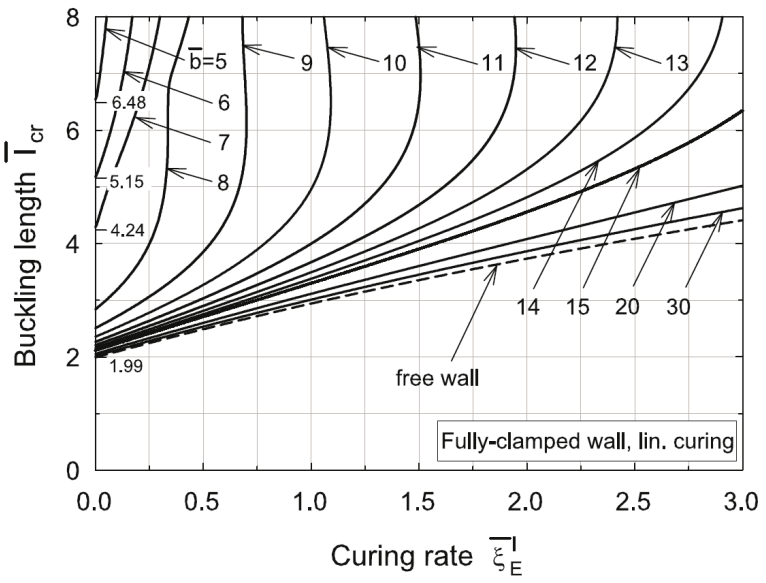

Figure 3.11: Design graph for a fully clapped wall. Taken from [39].

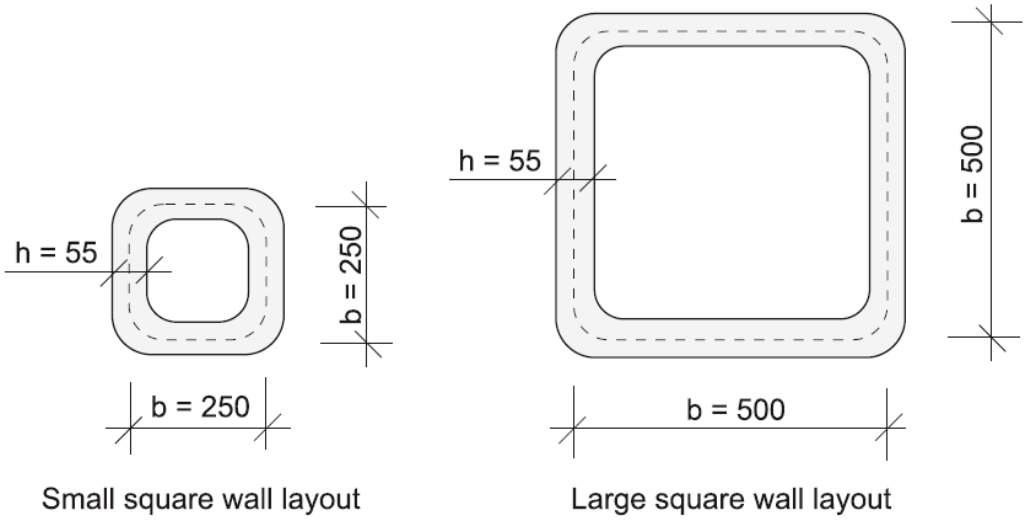

Figure 3.12: Geometries (small on the left and large on the right) of the squares printed as an example case, in which the straight side of each of the squares can be analysed using Suiker's model. Taken from [40].

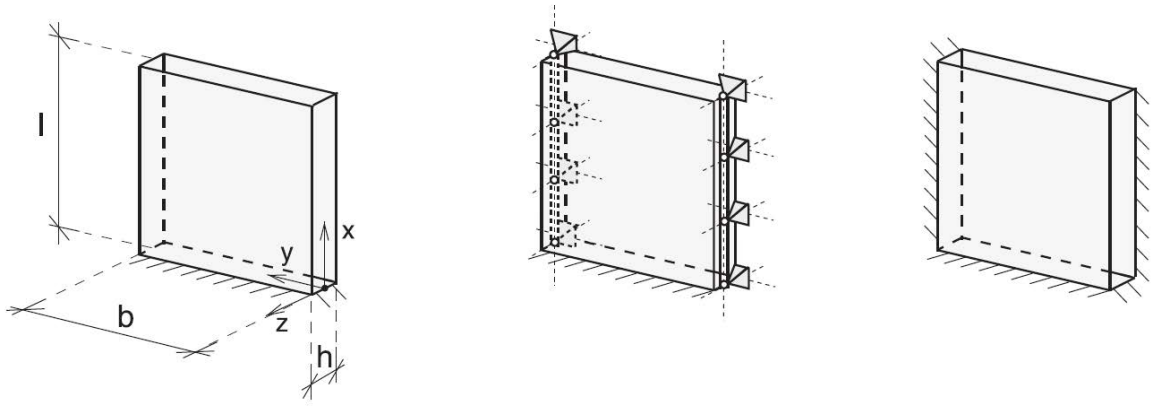

Figure 3.13: Free-standing wall (left), simply supported wall (middle), and fully clamped wall (right). Taken from [39].

Table 3.1: Known variables used for the calculations.

Design variables:

Variable	**Symbol**	**Value**	**Unit**
Layer width	h	55.0×10^{-3}	[m]
Layer height	t_l	9.5×10^{-3}	[m]
Print speed	ν_n	104.17×10^{-3}	[m/s]
Wall width (small square)	b_{small}	0.250	[m]
Wall width (large square)	b_{large}	0.500	[m]
Gravitational acceleration	g	9.81	[m/s^2]

Material variables:

Variable	**Symbol**	**Value**	**Unit**
Poisson factor	ν	0.3	[-]
Initial stiffness	$E_{p,0}$	48564	[N/m^2]
Initial strength	$\sigma_{p,0}$	2835	[N/m^2]
Density	ρ	2100	[kg/m^3]
curing rate for the elastic stiffness	ξ_E	8.954×10^{-4}	[s^{-1}]
Curing rate of the yield strength	ξ_σ	1.934×10^{-3}	[s^{-1}]

For the walls of the squares considered here, a simply supported scheme is appropriate. This is because the structure offers no resistance to bending: all sides of the square buckle simultaneously (i.e., global buckling), so the adjacent walls cannot provide any bending support to each other. The calculations for each of the sqaures can be seen in the grey boxes below, in which all known variables are grouped in Table 3.1.

Calculation for failure mode and length (i.e., 'height') for the small square
Step 1: Determine the dimensionless parameter $\bar{\xi}_E$

$$\bar{\xi}_E = \left(\frac{D_0}{\rho g h}\right)^{1/3} \frac{\xi_E}{\dot{l}}$$

Step 1a: Calculate D_0 (i.e., the initial bending stiffness of the wall)
$D_0 = \frac{E_0 h^3}{12(1-\nu^2)} = \frac{48564(55\times10^{-3})^3}{12(1-0.3^2)} = 0.740$ [Nm]

Step 1b: Calculate the wall growth velocity $\dot{l}$ (i.e., speed at which the wall grows in the vertical direction)
Initially, the time to print one layer (T_l) is calculated:
$T_l = \frac{4b_{small}}{\nu_n} = \frac{4\times0.250}{104.17\times10^{-3}} = 9.6$ [s]
$\dot{l} = \frac{t_l}{T_l} = \frac{9.5\times10^{-3}}{9.6} = 0.990 \times 10^{-3}$ [m/s]

Step 1c: Substituting previous result to calculate $\bar{\xi}_E$
$\bar{\xi}_E = \left(\frac{D_0}{\rho g h}\right)^{1/3} \frac{\xi_E}{\dot{l}} = \left(\frac{0.740}{2100\times9.81\times55\times10^{-3}}\right)^{1/3} \frac{8.954\times10^{-4}}{0.990\times10^{-3}} = 0.08$ [-]

Step 2: Determine the dimensionless parameter $\bar{b}$

$$\bar{b} = \left(\frac{\rho g h}{D_0}\right)^{1/3} b = \left(\frac{2100\times9.81\times55\times10^{-3}}{0.740}\right)^{1/3} 0.250 = 2.88 \text{ [-]}$$

Step 3: Determine the dimensionless parameter $\bar{l}_{cr}$ through design graph for simply supported structure

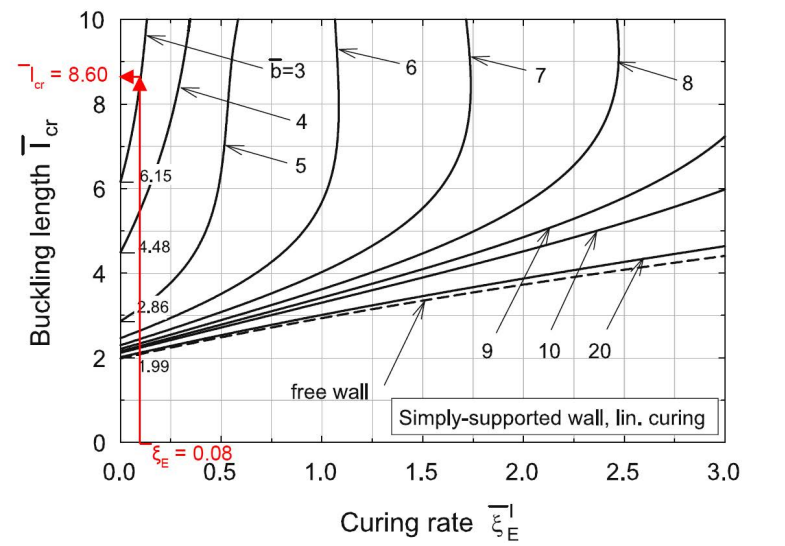

$\bar{l}_{cr} = 8.60$ [-]

Step 4: Determine the dimensionless parameter $\bar{\xi}_\sigma^l$

$$\bar{\xi}_\sigma^l = \frac{|\sigma_{p,0}|}{\rho g l} \xi_\sigma = \frac{|2835|}{2100\times9.81\times0.990\times10^{-3}} 1.934 \times 10^{-3} = 0.27 \text{ [-]}$$

Step 5: Determine the dimensionless parameter $\bar{l}_p$

$\bar{l}_p = \frac{\rho g}{|\sigma_{p,0}|} l_p = \frac{1}{1-\bar{\xi}_\sigma^l} = \frac{1}{1-0.27} = 1.37$ [-]

Step 6: Determine which failure mode is governing

Initially, we determine the dimensionless parameter $\overline{\Lambda}$
$\overline{\Lambda} = \left(\frac{h}{D_0}\right)^{\frac{1}{3}} \frac{|\sigma_{p,0}|}{(\rho g)^{\frac{2}{3}}} = \left(\frac{55.0\times10^{-3}}{0.740}\right)^{\frac{1}{3}} \frac{|2835|}{(2100\times9.81)^{\frac{2}{3}}}$ = 1.59 [-]

Then we determine the ratio $\bar{l}_{cr}/\bar{l}_p$
$\bar{l}_{cr}/\bar{l}_p = \frac{8.60}{1.37} = 6.29$ [-] (i.e., when the numbers are not rounded)

Determine failure mechanism based on:
$\frac{\bar{l}_{cr}}{\bar{l}_p} < \bar{\Lambda}$: elastic buckling,
$\frac{\bar{l}_{cr}}{\bar{l}_p} > \bar{\Lambda}$: plastic collapse.

$6.29 > 1.59$ □ Therefore plastic collapse is the governing failure mode.

Step 7: Determine the failure length l_p (i.e., 'height')

$\bar{l}_p = \frac{\rho g}{|\sigma_{p,0}|} l_p$ □ $l_p = \frac{\bar{l}_p}{\frac{\rho g}{|\sigma_{p,0}|}} = \frac{1.37}{\frac{2100\times9.81}{|2835|}} = 0.19$ [m]

Step 8: Determine expected failure layer n_p (rounded up to first integer)

$n_p = \frac{l_p}{t_l} + 1^* = \frac{0.19}{9.5\times10^{-3}} + 1^* = 21$ layers
* In case of first layer being kinematically constrained (i.e., first layer sticking to the printbed) the largest deformation will take place in the second layer [40].

Experimental result: Compare model result with experimental results

This small square has been printed twice and both times showed plastic collapse at the 23rd layer. The effective layer height just before failure was 9.0 mm instead of the theoretical 9.5 mm, explaining the difference of 2 layers with the theoretical model. A picture from the experiment taken from [40] is shown below:

Calculation for failure mode and length (i.e., 'height') for the large square
Step 1: Determine the dimensionless parameter $\bar{\xi}_E$

$$\bar{\xi}_E = \left(\frac{D_0}{\rho g h}\right)^{1/3} \frac{\xi_E}{\dot{l}}$$

Step 1a: Calculate D_0 (i.e., the initial bending stiffness of the wall)
$D_0 = \frac{E_0 h^3}{12(1-\nu^2)} = \frac{48564(55\times10^{-3})^3}{12(1-0.3^2)} = 0.740$ [Nm]

Step 1b: Calculate the wall growth velocity $\dot{l}$ (i.e., speed at which the wall grows in the vertical direction)
Initially, the time to print one layer (T_l) is calculated:
$T_l = \frac{4b_{small}}{\nu_n} = \frac{4\times0.500}{104.17\times10^{-3}} = 19.2$ [s]
$\dot{l} = \frac{t_l}{T_l} = \frac{9.5\times10^{-3}}{19.2} = 0.495 \times 10^{-3}$ [m/s]

Step 1c: Substituting previous result to calculate $\bar{\xi}_E$
$\bar{\xi}_E = \left(\frac{D_0}{\rho g h}\right)^{1/3} \frac{\xi_E}{\dot{l}} = \left(\frac{0.740}{2100\times9.81\times55\times10^{-3}}\right)^{1/3} \frac{8.954\times10^{-4}}{0.495\times10^{-3}} = 0.16$ [-]

Step 2: Determine the dimensionless parameter $\bar{b}$

$$\bar{b} = \left(\frac{\rho g h}{D_0}\right)^{1/3} b = \left(\frac{2100\times9.81\times55\times10^{-3}}{0.740}\right)^{1/3} 0.500 = 5.76 \text{ [-]}$$

Step 3: Determine the dimensionless parameter $\bar{l}_{cr}$ through design graph for simply supported structure

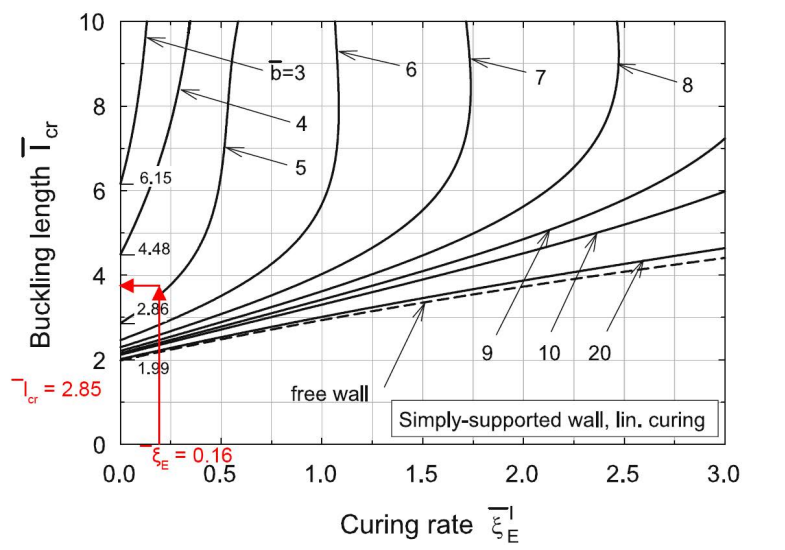

$\bar{l}_{cr} = 2.85$ [-]

Step 4: Determine the dimensionless parameter $\bar{\xi}_\sigma^{\bar{l}}$

$$\bar{\xi}_\sigma^{\bar{l}} = \frac{|\sigma_{p,0}|}{\rho g \dot{l}} \xi_\sigma = \frac{|2835|}{2100\times9.81\times0.495\times10^{-3}} 1.934 \times 10^{-3} = 0.54 \text{ [-]}$$

Step 5: Determine the dimensionless parameter $\bar{l}_p$

$\bar{l}_p = \frac{\rho g}{|\sigma_{p,0}|} l_p = \frac{1}{1-\bar{\xi}_\sigma^l} = \frac{1}{1-0.54} = 2.16$ [-] (i.e., when the numbers are not rounded)

Step 6: Determine which failure mode is governing

Initially, we determine the dimensionless parameter $\overline{\Lambda}$
$\overline{\Lambda} = \left(\frac{h}{D_0}\right)^{\frac{1}{3}} \frac{|\sigma_{p,0}|}{(\rho g)^{\frac{2}{3}}} = \left(\frac{55.0\times10^{-3}}{0.740}\right)^{\frac{1}{3}} \frac{|2835|}{(2100\times9.81)^{\frac{2}{3}}}$ = 1.59 [-]

Then we determine the ratio $\bar{l}_{cr}/\bar{l}_p$
$\bar{l}_{cr}/\bar{l}_p = \frac{2.85}{2.16} = 1.32$ [-]

Determine failure mechanism based on:
$\frac{\bar{l}_{cr}}{\bar{l}_p} < \bar{\Lambda}$: elastic buckling,
$\frac{\bar{l}_{cr}}{\bar{l}_p} > \bar{\Lambda}$: plastic collapse.

$1.32 < 1.59$ □ Therefore elastic buckling is the governing failure mode.

Step 7: Determine the failure length l_{cr} (i.e., 'height')

$\bar{l}_{cr} = \left(\frac{\rho g h}{D_0}\right)^{1/3} l_{cr}$ □ $l_{cr} = \frac{\bar{l}_{cr}}{\left(\frac{\rho g h}{D_0}\right)^{1/3}} = \frac{2.85}{\left(\frac{2100\times9.81\times55\times10^{-3}}{0.740}\right)^{1/3}} = 0.25$ [m]

Step 8: Determine expected failure layer n_e (rounded up to first integer)

$n_e = \frac{l_{cr}}{t_l} + 1^* = \frac{0.25}{9.5\times10^{-3}} = 27$ layers

Experimental result: Compare model result with experimental results

This large square has been printed twice, and both times showed elastic buckling as the failure mode at the 27th and 28th layer, respectively. A picture from the experiment taken from [40] is shown below:

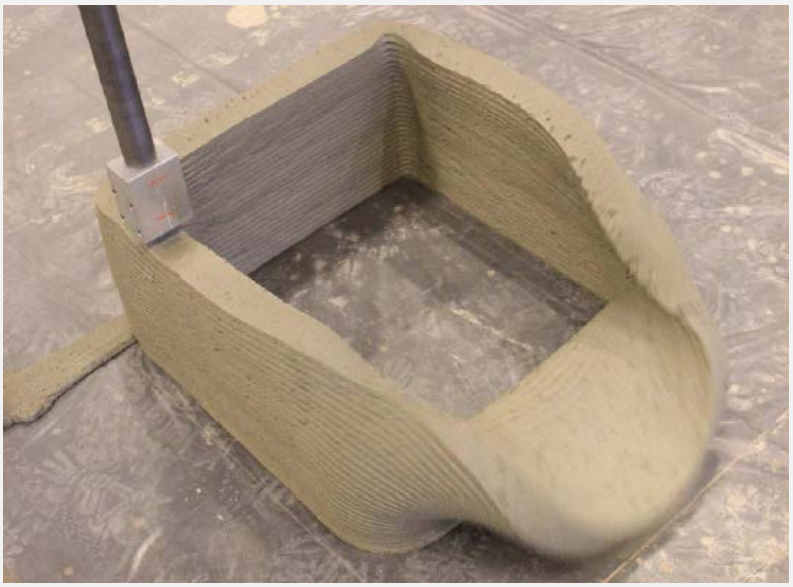

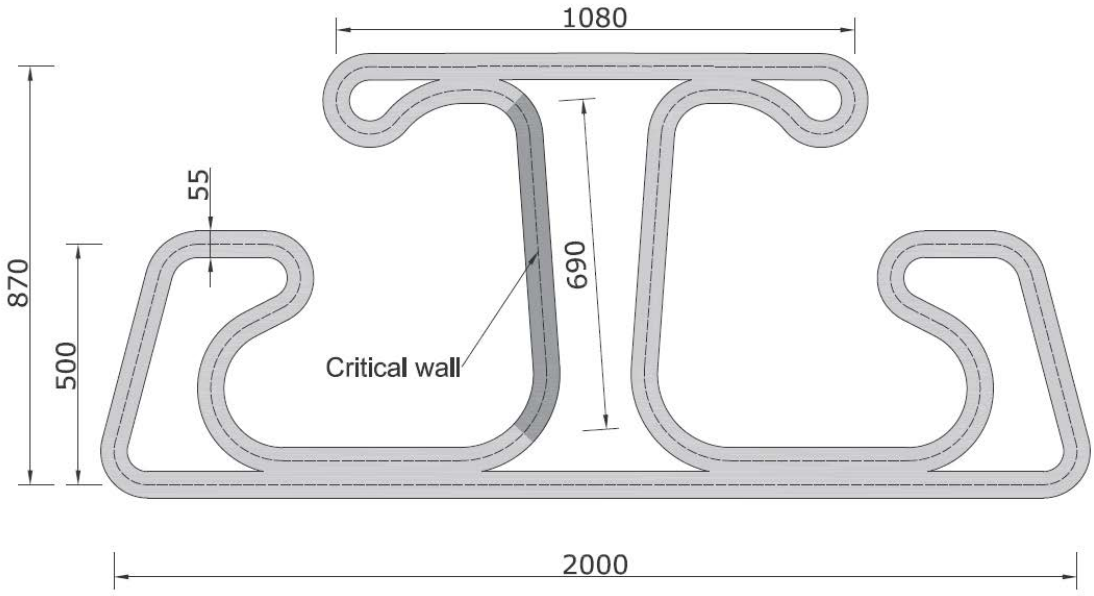

Figure 3.14: Picnic table design, with critical location for elastic buckling highlighted. Taken from [40].

To demonstrate the use of this theoretical mechanistic model, the example presented in [40] for a picnic table is also presented here in a step-by-step fashion (similar to the squares). The design of the picnic table can be seen in Fig. 3.14. The structure is designed with a desired height of 760 mm ($H = 0.760$ m), which will be achieved by printing 80 layers of 9.5 mm. The print path length for a single layer is 9167 mm ($C = 9.167$ m).

To ensure that the picnic table remains structurally sound during the 3D-printing process, two checks are required: (i) the structure must not undergo plastic collapse, and (ii) the most critical wall in the layout must remain stable against buckling [40]. The wall segment highlighted in Fig. 3.14 is most critical from the buckling perspective and has a width of $b = 690$ mm. This wall has a partial rotational constraint at the sides, by which it falls between a simply supported and a fully clamped wall. To be on the safe side, it will be assumed as if the wall is simply supported. Since we are designing for a specific height H, we can use the dimensionless structural height parameter $\bar{H}$, in a similar manner to how $\bar{l}_{cr}$ was calculated.

$$\bar{H} = \left(\frac{\rho g h}{D_0}\right)^{1/3} H, \tag{3.8}$$

This dimensionless parameter can then be compared to $\bar{l}_{cr}$ to assess whether buckling occurs. Buckling is avoided when $\bar{l}_{cr} < \bar{H}$. The material printed on the day of the picnic table had an initial elastic stiffness of $E_0 = 55000$ N/m^2 and a curing rate for the elastic stiffness of $\xi_E = 7.0 \times 10^{-3}$ s$^-1$. For the remaining parameters, the same variables as those listed in Table 3.1 are used.

Practical Example - Picnic Table

Step 1: Determine the dimensionless parameter $\bar{\xi}_E$

$$\bar{\xi}_E = \left(\frac{D_0}{\rho g h}\right)^{1/3} \frac{\xi_E}{\dot{l}}$$

Step 1a: Calculate D_0 (i.e., the initial bending stiffness of the wall)
$D_0 = \frac{E_0 h^3}{12(1-\nu^2)} = \frac{55000(55\times10^{-3})^3}{12(1-0.3^2)} = 0.838$ [Nm]

Step 1b: Calculate the wall growth velocity $\dot{l}$ (i.e., speed at which the wall grows in the vertical direction)
Initially, the time to print one layer (T_l) is calculated:
$T_l = \frac{C}{\nu_n} = \frac{9.167}{104.17\times10^{-3}} = 88.0$ [s]
$\dot{l} = \frac{t_l}{T_l} = \frac{9.5\times10^{-3}}{88.0} = 0.108 \times 10^{-3}$ [m/s]

Step 1c: Substituting previous result to calculate $\bar{\xi}_E$
$\bar{\xi}_E = \left(\frac{D_0}{\rho g h}\right)^{1/3} \frac{\xi_E}{\dot{l}} = \left(\frac{0.838}{2100\times9.81\times55\times10^{-3}}\right)^{1/3} \frac{7.0\times10^{-3}}{0.108\times10^{-3}} = 5.86$ [-]

Step 2: Determine the dimensionless parameter $\bar{b}$

$$\bar{b} = \left(\frac{\rho g h}{D_0}\right)^{1/3} b = \left(\frac{2100\times9.81\times55\times10^{-3}}{0.838}\right)^{1/3} 0.690 = 7.63 \text{ [-]}$$

Step 3: Determine the dimensionless parameter $\bar{l}_{cr}$ through design graph for simply supported structure

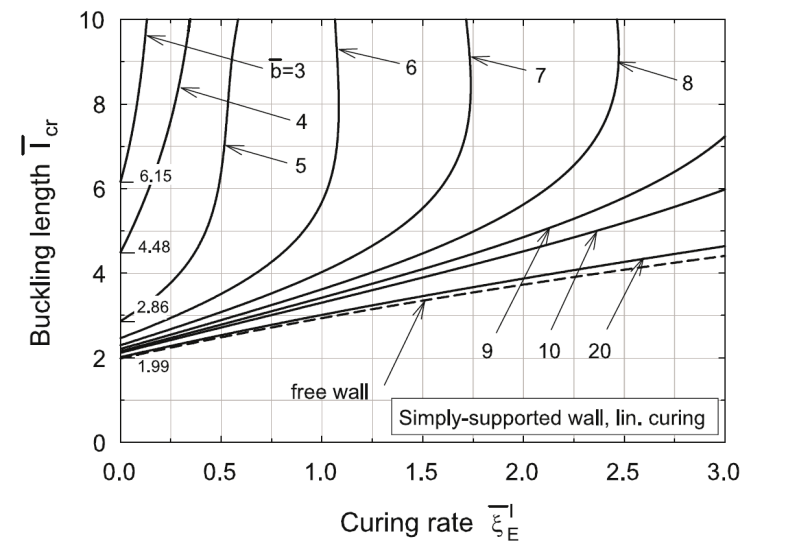

This will yield a value which you can't read from this graph, as the value for the dimensionless parameter $\bar{l}_{cr}$ will be much larger than the max shown 10.0.
$\bar{l}_{cr} >> 10.0$ [-]

Step 4: Determine the dimensionless parameter $\bar{H}$

$\bar{H} = \left(\frac{\rho g h}{D_0}\right)^{1/3} H = \left(\frac{2100 \times 9.81 \times 55 \times 10^{-3}}{0.838}\right)^{1/3} 0.760 = 8.40$ [-]

Step 5: Check if elastic buckling occurs ($\bar{l}_{cr}$ < $\bar{H}$)

$\bar{l}_{cr} >> 10.0$ **>** $\bar{H} = 8.40$, so no elastic buckling occurs.

Step 6: Determine the dimensionless parameter $\bar{\xi}^{l}_{\sigma}$

$\bar{\xi}^{l}_{\sigma} = \frac{|\sigma_{p,0}|}{\rho g l} \xi_{\sigma} = \frac{|2835|}{2100 \times 9.81 \times 0.108 \times 10^{-3}} 1.934 \times 10^{-3} = 2.46$ [-]

Step 7: Determine the dimensionless parameter $\bar{l}_p$

$\bar{l}_p = \frac{\rho g}{|\sigma_{p,0}|} l_p = \frac{1}{1 - \bar{\xi}^{l}_{\sigma}} = \frac{1}{1 - 2.46} = -0.68$ [-] (i.e., $\bar{l}_p \to \infty$)

As $\bar{l}_p$ goes to infinity, plastic collapse will never happen.

Experimental result: Confirmation of the printability of the object can be seen in the picture below.

3.5.2 Numerical Modelling of Early-Age 3D Printed Concrete

Suiker's model provides accurate estimates for simple geometries (e.g., free-standing walls, rectangular shapes, etc.) and can also be used to obtain lower-bound (i.e., conservative—estimates) for more complex structures, such as the picnic table presented in [40]. Furthermore, the model can be applied to reverse-engineer material properties based on experimental printing tests of free-standing walls or rectangular specimens in different configurations [39, 40, 16]. However, to accurately assess more complex geometries, numerical modeling of the structure is essential, and Wolfs [16] developed a custom FEM script in Abaqus for this purpose, which relies on understanding the material in its earliest phase, typically the first 0–90 minutes after extrusion. The mechanical behaviour is governed by parameters that evolve with time such as the compressive strength and stiffness (Young's

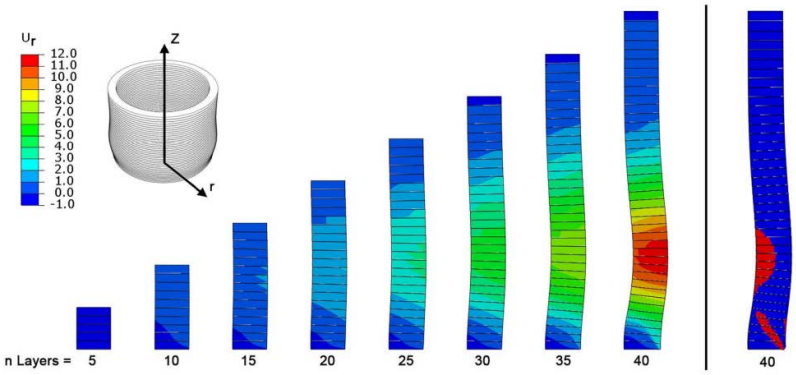

Figure 3.15: FEM (Finite Element Method) results of a cylinder being printed, showing deformation for an increasing number of layers. The image on the right highlights in red the regions where the yield stress is reached and plastic deformation begins. Taken from [16].

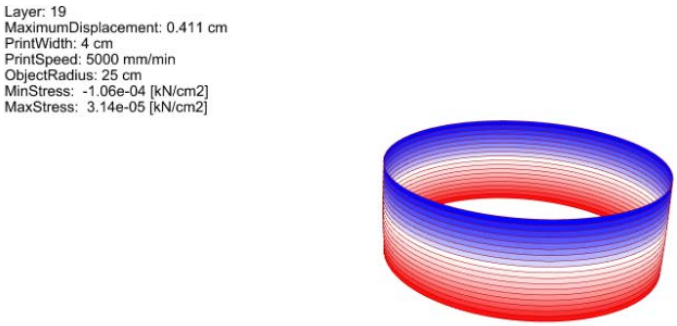

Figure 3.16: Screenshot from FEM tool made by Shaun Wu (working at Witteveen+Bos) in collaboration with Karama3D to simulate the printing process. (Tool license: CC BY-SA 4.0)

modulus), as discussed in the previous section. To obtain these results, the uniaxial compression tests and direct shear test have been used [16], see Chapter 2 for general explanation of these tests. These experimentally derived, time-dependent properties are implemented in the FEM model using a Mohr–Coulomb failure criterion. The printing process is simulated by adding layers sequentially, assigning each layer properties according to its age. This allows the model to realistically capture both material yielding and stability-related deformations such as buckling. An exmaple of a cylinder can bee seen in Fig. 3.15.

Such a model is highly valuable for assessing printability, optimizing printing speed, designing robust geometries, and improving material formulations. It functions as a virtual printing environment that enables engineers to predict and control the behaviour of printed structures before printing them physically. A practical implementation of this approach has been developed by Shaun Wu (Witteveen+Bos) within the Grasshopper–Rhinoceros environment, making use of the Karamba3D plug-in (see Fig. 3.16) [66].

3.6 Selection of Realized Projects

3.6.1 Gemert & Nijmegen Bridges (Netherlands)

Gemert Bridge

The 3D-printed bicycle bridge in Gemert, the Netherlands, was the world's first structurally certified 3D-printed concrete bridge intended for public use, Figure 3.17. The bridge's geometry was tailored to the capabilities of TU/e's 3D concrete printer. Instead of printing the 6.5 m span in one piece, the deck was designed as six hollow printed elements. These elements were later post-tensioned using Dywidag tendons to ensure the entire section remained in compression under service loads. Extensive material testing—compression, tensile, modulus, creep, and shrinkage—was performed on printed specimens in all three directions to account for anisotropy, as described in [67].

Figure 3.17: 3D concrete printed bridge in Gemert

Each element was printed using the reinforcement entrainment device (RED) with a hybrid down/back-flow nozzle that enabled embedding a continuous high-strength steel cable into the filament while maintaining good interlayer bonding. After printing, each element was lifted from the print bed, rotated, and placed into a wooden scaffold for precise alignment. A thin epoxy-based interface layer was applied between the elements to minimise local stress concentrations during prestress transfer. Sixteen prestress tendons were threaded through the hollow cores and tensioned to 150 kN to ensure a fully compression-only state. Once prestressed, the complete deck was hoisted onto the conventional abutments, as shown in Figure 3.18. The preceding scale-model testing had already validated the structural behaviour, demonstrating a bending-dominated failure mechanism and sufficient load capacity. Before the bridge was opened to the public, a final in-situ test was conducted

in which water-filled containers imposed a 57 kN load—equivalent to 100 % of the serviceability bending moment—without measurable deflection or visible damage. After applying the surface finish and installing the parapet, the bridge was officially opened in October 2017.

Figure 3.18: Gemert bridge assembly

Nijmegen Bridge (2022)

The Nijmegen pedestrian and cyclist bridge represents a major scale-up in 3D concrete printing: a 29-metre span, making it on of the largest 3D-printed concrete bridge produced by extrusion to date, seen on Figure 3.19. The project, funded by Rijkswaterstaat, used the bridge as a living laboratory to develop a complete design, testing, and validation framework for large-scale 3DCP structures.

Figure 3.19: Nijmegen bridge

The production of the bridge followed a structured framework consisting of design development, mock-up manufacturing, structural validation, and full-scale realization. The process began with a parametric conceptual design created to accommodate the technology-specific constraints of extrusion-based 3D concrete printing. Because the bridge geometry consists of a double-curved deck supported on tapered columns, the structural concept relied on subdividing the full span into five prestressed girders, seen on Figure 3.20, each composed of multiple printed segments joined through epoxy bonding and post-tensioning.

Figure 3.20: The five prestressed girders being assembled on site in Nijmegen

An example of the individual segements can be seen on Figure 3.21.The printed geometry was based on bottle-shaped void structures similar to the earlier Gemert bridge, allowing reduced material use while forming continuous ducts for prestressing tendons.

Figure 3.21: Nijmegen segments

In the production phase, a full-scale mock-up was manufactured to evaluate printability and structural performance. First, a representative column was printed to assess buildability of the highly curved, cantilevering geometry; initial failures led to geometric refinements before a successful print was achieved. Next, six girder segments were printed using 80 mm-wide filaments and a 60 × 12 mm back-flow nozzle. Because of the complex curvature, granular support material was manually placed to stabilize inward-cantilevering regions. Subsequently, conventional reinforced anchor blocks were cast in 3D-printed lost formwork to achieve consistent surface texture, seen on Figure 3.22.

Figure 3.22: Reinforced anchor blocks were cast in 3D-printed formwork, and post-tensioning of tendons.

Assembly of the mock-up followed procedures developed for the earlier Gemert bridge: printed segments were rotated 90°, placed on a curved temporary scaffold, bonded with epoxy at each interface, and post-tensioned with unbonded tendons arranged in two rows (nine at the top, six at the bottom). The assembled girder—approximately 5.9 m long—was then tested under two four-point bending configurations. Results demonstrated linear-elastic behaviour up to and beyond the ultimate limit state, with no cracking observed even at loads exceeding three times the design shear capacity. These successful outcomes validated the manufacturing strategy and allowed approval for full-scale production.

The final bridge was printed and assembled by industrial partners following the same protocols. Each girder was tested on site through diagnostic loading using water tanks filled in increments to 100% of the ultimate limit state load, seen on Figure 3.23. As with the mock-up, the full-scale girders exhibited minimal deflection and no detectable damage, confirming adequate stiffness and safety.

Figure 3.23: Assembly of individual girders on temporary formwork and loading to ULS, courtesy of courtesy De Gelderlander (Paul Rapp)

The bridge columns were constructed as conventional reinforced concrete elements but cast inside 3D-printed lost formwork. Structurally, they function exactly like standard RC columns—anchored to a pile foundation and reinforced in the usual manner. Because their behaviour does not differ from traditional practice, they were not included in the structural testing programme or further analysis, seen on Figure 3.24.

Figure 3.24: Assembly of printed formwork for bridge columns, with temporary supports, just before casting, courtesy De Gelderlander (Paul Rapp)

The bridge was subsequently placed on its foundation columns and abutments and prepared for public use.

Figure 3.25: Multiple girders assembled, courtesy De Gelderlander (Paul Rapp)

3.6.2 Project Milestone

Project Milestone is the first fully 3D printed, permanently inhabited concrete house in the Netherlands and represents a major step toward moving 3DCP from demonstration projects to structurally certified building applications. Developed through a collaboration between TU/e, the Municipality of Eindhoven, and industrial partners, the project required demonstrating compliance with conventional structural and safety standards despite the absence of formal 3DCP-specific regulations.

The first Milestone house, see on Figure 3.26, is a single-storey dwelling composed entirely of load-bearing 3D-printed concrete walls, featuring pronounced in- and out-of-plane curvatures to showcase material efficiency and geometric freedom. Two wall types were developed: Type A, with modest inclinations and a single outer shell, and Type B, with large inclinations requiring a double-leaf geometry and infill to maintain stability, seen on Figure 3.27. All elements were printed off-site as transportable modules, using a commercially available printable mortar with a small amount of PP fibres and steel connectors to ensure composite action with injected insulation.

Figure 3.26: The first house of project Milestone

A comprehensive mock-up testing program at TU/e validated both the manufacturability and structural performance of the elements. Full-scale walls were printed, cured, filled with insulation, and sawn into test specimens to evaluate vertical load resistance, bending response under eccentric loading, and potential buckling behaviour. Both bonded and unbonded configurations were assessed. The walls showed stable behaviour, limited deformations, and no visible damage under the applied loads, providing the basis for municipal approval and issuance of the building permit.

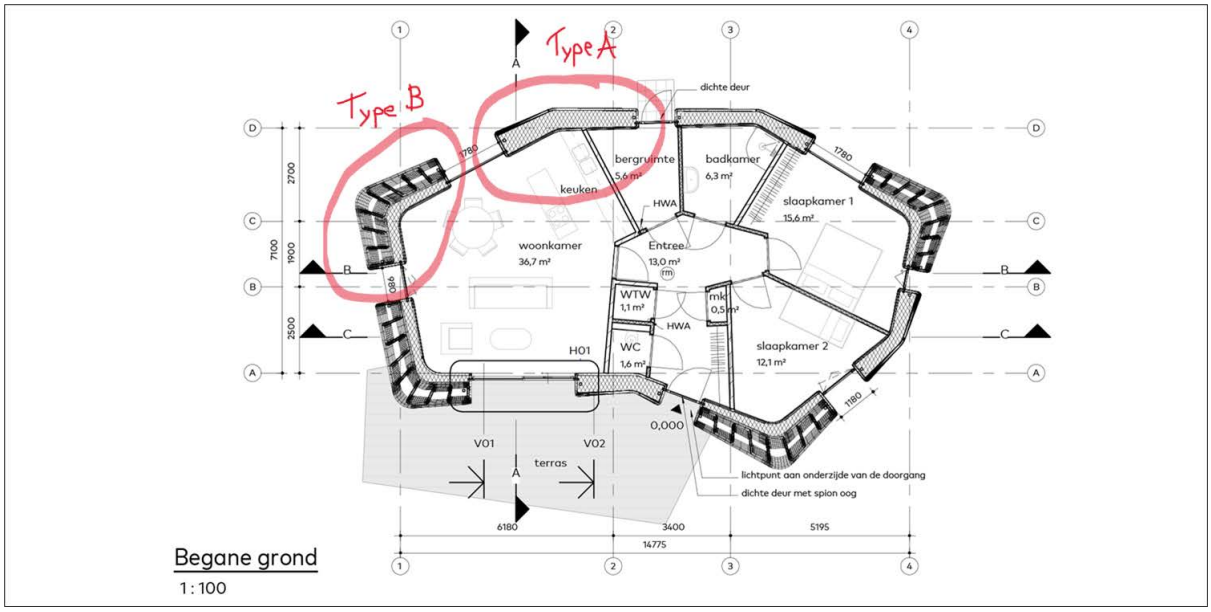

Figure 3.27: Floor plan of the first project Milestone house, with Type A and B highlighted

Following successful testing, all house components were printed off-site under controlled environmental conditions. Long printing durations (10–15 hours per element) posed challenges related to drying and interlayer bonding, requiring careful process control, curing compounds, and humidification. Elements were transported on integrated printed slabs due to uncertainties in anchorage behaviour. The lifting process can be seen on Figure 3.28.

Figure 3.28: The elements were lifted from the bottom and clamped during the top frame for stability

On-site assembly involved careful detailing of interfaces with conventional building components such as windows, roof connections, and foundations, especially to avoid thermal bridging. The house was coated for weather protection and designed for a minimum 50-year service life.

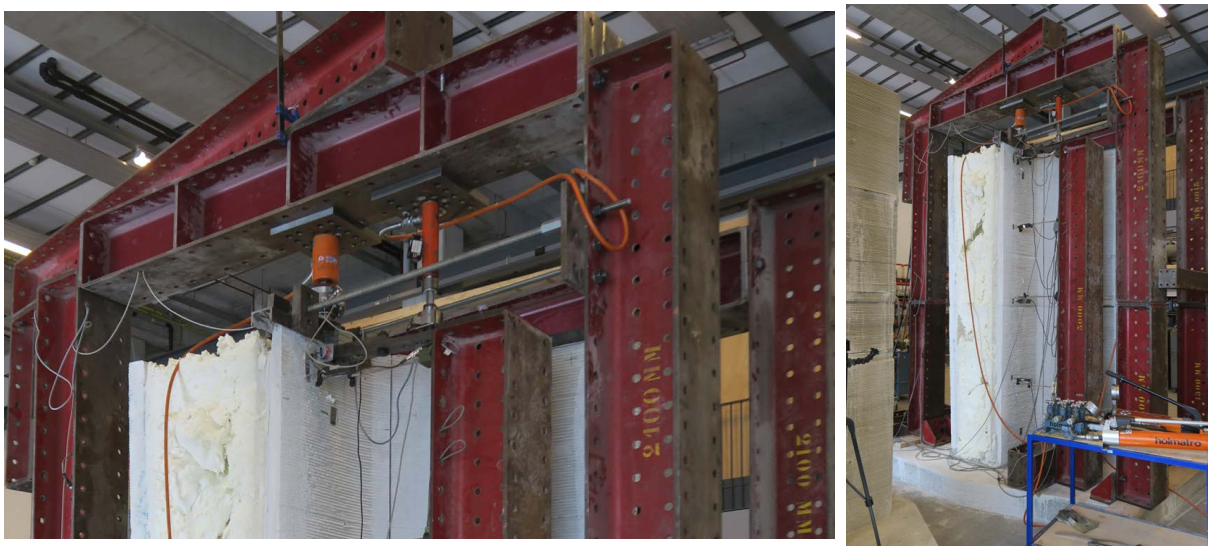

Figure 3.29: Testing of the project Milestone first house mock-up at TU Eindhoven

Two new house types have now been developed, both featuring multiple floors—unlike the first Milestone dwelling. These houses obtain their structural capacity entirely from the printed concrete itself. An illustrated image of the new designs are shown on Figure 3.30.

Figure 3.30: New house types planned to be built as part of project Milestone

3.6.3 Tor Alva

The Tor Alva project, documented in Fabricate 2024: Creating Resourceful Futures by Anton et al. [68], presents one of the most ambitious built applications of digi-

tal concrete fabrication to date. Tor Alva is a 30-metre-tall tower composed of bespoke 3D-printed concrete components, developed through a collaboration between ETH Zürich's Digital Building Technologies, the Physical Chemistry of Building Materials group, the Concrete Structures and Bridge Design group, and the Origen Foundation. As the first multi-storey building worldwide constructed with load-bearing 3D-printed reinforced concrete columns, the tower marks a significant milestone in demonstrating how digital fabrication can redefine both structural and architectural possibilities. Situated in the small Alpine village of Mulegns, Switzerland, the tower serves as a temporary cultural venue, supporting the Origen Foundation's mission to revive a rapidly depopulating region through artistic interventions. Beyond its architectural presence, Tor Alva is conceived as a long-term research platform: the structure will remain in place for five years, after which it will be fully dismantled and reassembled at a new location. This planned relocation directly tests principles of circularity, modularity, and reuse in digitally fabricated construction, illustrating how 3D concrete printing can support not only material innovation but also sustainable life-cycle strategies.

Tor Alva is constructed from 41 bespoke prefabricated components, each forming a branching column composed of three integrated parts: a precast base segment cast in 3D-printed formwork, a load-bearing 3D-printed concrete column segment (Figure 3.31), and a precast capital. As illustrated in Figures 1–4 of the original documentation, these elements are designed to interlock using dry shear-keyed connections, allowing precise alignment, structural continuity, and full reversibility for future disassembly [68]. The architectural expression of the tower emerges directly from the fabrication process: the 8 mm print-layer resolution produces a refined surface texture, while deliberately programmed overhangs create characteristic drip-formed ornamentation that visually unifies the modular components. Prefabrication plays a critical role in enabling this level of precision, as the tower requires tolerances far tighter than typical 3D printing can achieve on site, as well as components that can be transported from the robotic facility to the remote mountain location. To meet these stringent requirements, ETH Zürich developed match-casting–inspired fabrication methods, including printing directly onto precast elements or onto controlled substrates, achieving sub-millimetre accuracy essential for the reliability of the dry-connected system.

Figure 3.31: Production of one branch, taken from [68]

Structurally, Tor Alva departs from the typical vertical wall typology that characterises much of current 3D concrete printing. Instead, the tower employs branching columns whose inclined geometries enhance global performance by transferring lateral wind and seismic loads primarily through axial forces, thereby increasing stiffness and reducing the number of required supports. These columns are conceived as multi-layered structural elements: the outer layer provides the visible architectural texture; the middle layer incorporates shear reinforcement inserted between printed layers during fabrication; and the inner layer forms continuous hollow channels that accommodate longitudinal reinforcement bars, which are later grouted to establish structural bond and continuity [68]. Each component is further post-tensioned with stainless steel rods running through its core, ensuring the unity of its three segments, improving load transfer across printed filament layers, mitigating serviceability cracking, and facilitating safe transport and reassembly. The resulting system—combining printed concrete, conventional reinforcement, and post-tensioning—demonstrates that 3D concrete printing can function as a fully load-bearing structural method rather than merely as stay-in-place formwork.

Figure 3.32: Assembled

Prior to the final Tor Alva tower, ETH Zürich constructed a full-scale demonstrator comprising ten segmented columns assembled between two precast slabs. This prototype exposed several critical fabrication challenges. Most notably, early attempts revealed that unreinforced printed shells could not withstand the substantial hydrostatic pressures generated during the casting of self-compacting concrete, resulting in failures of the formwork [68]. This issue was ultimately resolved by adopting a staged casting process, restricting each pour to a maximum height of 80 cm. The demonstrator also highlighted the inefficiency of using 3D-printed elements solely as sacrificial formwork, underscoring the need to structurally activate the printed material itself—a requirement that led directly to Tor Alva's integrated reinforcement strategy and hollow-core post-tensioning system.

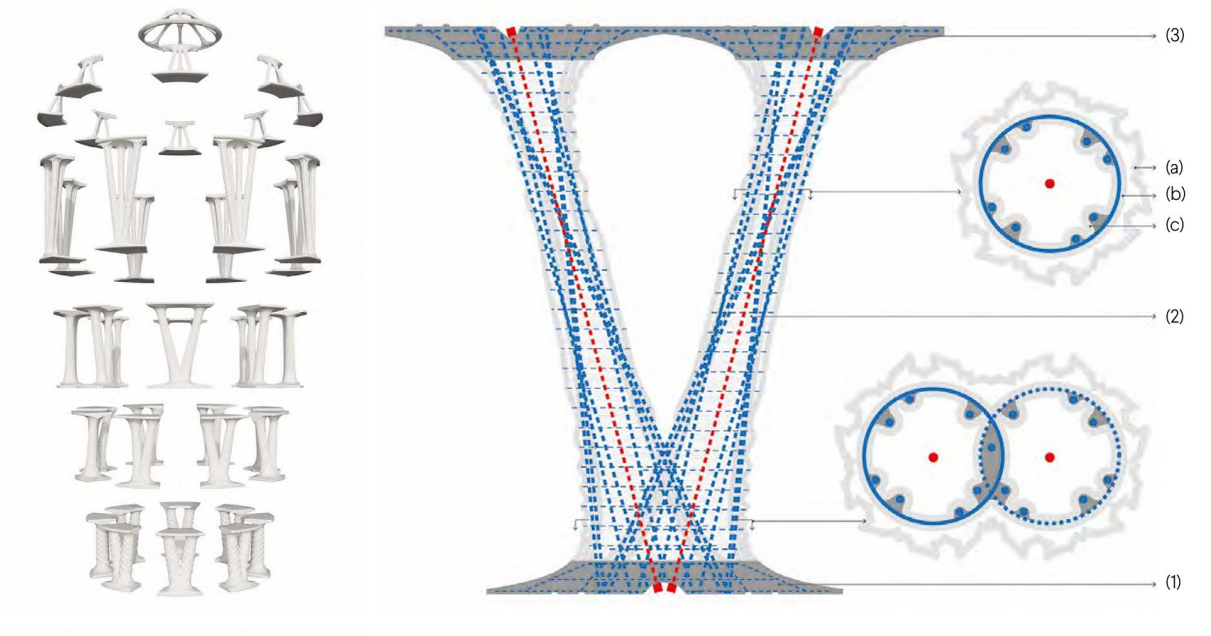

Figure 3.33: Left: Final design of Tor Alva composed of 41 bespoke components assembled using dry shear-keyed connections. Right: Diagram of a branching column component showing its three-part segmentation: (1) precast base segment; (2) load-bearing 3D-printed concrete column with (a) an outer layer providing ornamented texture, (b) a middle layer accommodating shear reinforcement, and (c) an inner layer forming hollow channels for longitudinal reinforcement; and (3) precast capital segment, taken from [68].

Further insights emerged regarding precision, reinforcement integration, and logistical constraints. Achieving dry shear-keyed connections required tolerances far beyond those of standard 3DCP, motivating the development of match-cast inspired methods, including reprinting directly onto precast or previously printed substrates to achieve sub-millimetre accuracy. Reinforcement integration also presented practical difficulties: while shear reinforcement could be manually inserted between layers during printing, vertical reinforcement and grouting still required careful post-processing, as full automation remains under development. Finally, the remote Alpine site and narrow access routes imposed strict limits on component size and geometry, necessitating modular segmentation strategies that shaped the overall form and assembly logic of the tower.

3.6.4 The Canopy

The Canopy, seen on Figure 3.34 project represents over five years of collaborative research between Loughborough University's School of Architecture, Building and Civil Engineering, Foster + Partners, and Cundall, supported by UK Research and Innovation. As the first full-scale architectural demonstrator constructed using hybrid 3D concrete printing (h-3DCP), it showcases a fabrication method that merges additive 3D concrete printing with subtractive CNC milling. This combined approach enables the production of highly accurate, doubly curved components directly from digital models. While the Canopy, like Tor Alva, serves both as a design prototype

and a research platform, its focus is distinct: it explicitly examines how manufacturing tolerances, material behaviour, and process constraints must inform digital design workflows to shift the field from digital crafting—heavily reliant on expert judgement—toward reproducible, scalable digital manufacturing [69, 70].

A central ambition of the project is to demonstrate the benefits of uniting deposition-based printing with high-resolution milling. The completed structure consists of five components—four interlocking roof panels and a hollow column—fabricated with precision that far exceeds what is typically achievable through 3D printing alone. CNC-milled dovetail joints, recessed interfaces, drainage features, and integrated service conduits exemplify how hybrid fabrication can embed functional and assembly-related details directly into the concrete geometry[69, 70]. This level of integration not only enhances structural and architectural performance but also supports modularity, disassembly, and reuse, aligning the Canopy with circular construction principles similar to those explored in Tor Alva's reversible connection strategy.

Figure 3.34: The Canopy, taken from [69].

Structurally, the Canopy advances digital fabrication into the domain of true load-bearing architecture through an integrated shell–column system. The roof panels

are strengthened with alkali-resistant glass-fibre textile mesh inserted mid-print, enabling their slender thin-shell geometry while ensuring adequate structural capacity. Each panel features variable shell thickness and tapered ribs that have been digitally shaped to follow the principal load paths. The overall mass distribution is also carefully calibrated so that the assembled canopy remains perfectly balanced over the supporting column, effectively eliminating self-weight–induced bending moments. As a consequence, the column is required to resist only environmental and accidental actions—an approach that parallels Tor Alva's pursuit of structurally efficient, digitally optimised geometries, seen on Figure 3.35.

The hollow printed column is designed to perform multiple functions within a highly constrained form. Its slender oval cross-section (300 × 250 mm) contains four internal steel bars used for post-tensioning, ensuring the column remains in compression without conventional reinforcement. At the same time, the column accommodates rainwater drainage, electrical and data conduits, and structural interface plates. Several rounds of prototyping—including overhang trials up to 60° and experiments with internal stiffening patterns—helped refine the column's geometry and printability. Ultimately, the final configuration was produced as a single monolithic print in under 40 minutes using the accelerated 2K material system.

The canopy's assembly depends on CNC-milled precision joints, combining a long bolted interface with two robust dovetail connections that permit small adjustments during alignment. Early exploration of more intricate "carpentry-style" interlocks revealed issues related to brittleness, complex milling requirements, and tight tolerance demands. These challenges were further confirmed through full-scale mock-ups and structured-light scanning, which showed most deviations within ±2 mm but highlighted sensitivity around joint edges and mating surfaces. The final jointing strategy therefore balances geometric ambition with the practical realities of fabrication accuracy and assembly robustness.

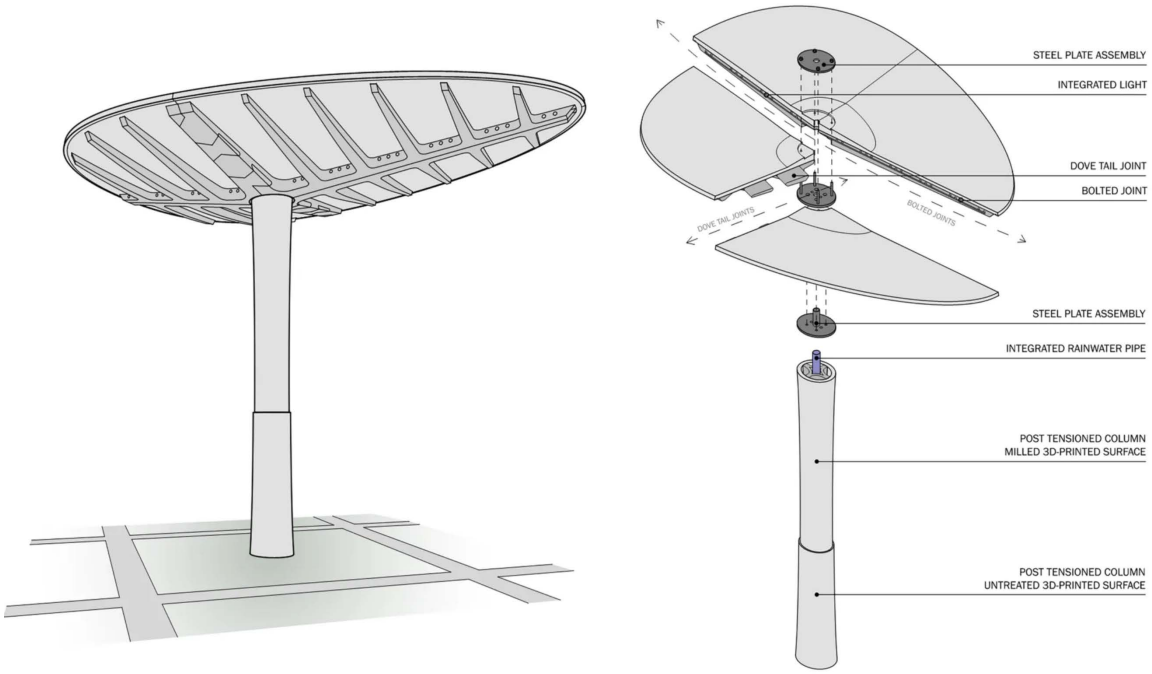

Figure 3.35: The principal assembly components of the canopy section and the column, taken from [70].

The Canopy employs a hybrid fabrication process that integrates all major production stages—former milling, 3D concrete printing, and green-state milling—within a single robotic manufacturing cell. Using an ABB IRB robotic arm with a 2.55 m reach and 185 kg payload, the system can alternate between a 1K batch-mixed printing setup for large, slowly setting panels and a 2K accelerated system for elements requiring rapid vertical build-up, such as the column. Interchangeable milling heads enable precise subtractive shaping while the material remains in its green state. The workflow begins with CNC milling of a foam or timber former, continues with conformal layer-by-layer deposition of concrete and insertion of textile reinforcement, and concludes with green-state milling to achieve the final geometry. This combined sequence allows the production of highly detailed features—tapered ribs, drainage rebates, service channels, and crisp edges—with net-shape accuracy often within ±2 mm of the digital model.

A key challenge in this workflow is managing positional accuracy and tolerance accumulation. Robot positioning errors vary non-linearly across the build platform, necessitating careful calibration, continuous validation, and the use of digital twins to simulate toolpaths and detect potential collisions. Critical joint interfaces were deliberately positioned within the robot's most accurate operating zone to ensure the precision required for the CNC-milled dovetail and bolted connections. These considerations underscore the importance of integrating manufacturing constraints directly into the design workflow—an approach central to both the Canopy and Tor Alva.

Because printed mortar exhibits anisotropic and time-dependent behaviour, the final components underwent extensive structural testing. Staged load tests,

backed by finite-element simulations, confirmed elastic recovery, repeatable load–deformation behaviour, and the structural performance of the post-tensioned joints. Additional tests verified the robustness of integrated systems such as lighting and drainage, as well as the assembly tolerances of the milled interfaces. Long-term monitoring instrumentation was installed to observe environmental effects—moisture, UV exposure, and temperature—transforming the Canopy into a long-term research platform that tracks the durability and behaviour of hybrid-manufactured concrete elements.

Beyond fabrication and structural performance, the Canopy also demonstrates significant sustainability potential. By eliminating traditional formwork, hybrid 3D printing reduces material waste and lowers production costs. Geometric optimisation—evident in the thin shell, hollow column, and ribbed stiffening—ensures material is placed only where structurally necessary. Functional integration, such as built-in cable conduits and drainage channels, further reduces the need for secondary materials or labour. Milling in the green state consumes far less energy than machining hardened concrete, and the project's modular dry-jointed assembly supports disassembly and reuse. Ongoing doctoral research is quantifying the embodied carbon associated with h-3DCP, reinforcing its potential role in advancing net-zero construction.

Ultimately, the Canopy illustrates that digital fabrication is not simply a novel method for shaping concrete. It represents a shift in how architectural components are conceived, manufactured, tested, and sustained over time. Much like Tor Alva, it embodies a new paradigm—one in which lifecycle considerations, precision manufacturing, and digital design merge to support more adaptive, sustainable, and reconfigurable built environments.

Chapter 4

Reinforcement Strategies for Printed Concrete

Digital design and fabrication technologies offer new opportunities to rethink concrete construction. It has the potential to re-establish the unity of material, process, and form by eliminating conventional formwork and enabling fabrication directly from digital models. Within this context, 3DCP introduce an entirely new design space, where material placement can be locally optimised and structural efficiency can be re-evaluated.

Recent technological advances have enabled the construction of demonstrators using unreinforced 3D-printed concrete. Examples include printed houses that replace lightly loaded masonry walls with unreinforced printed concrete designed to carry compression, and 3D-printed bridges that use post-tensioned, unreinforced printed segments assembled into full-scale structures [71, 72]. These developments demonstrate that unreinforced 3DCP can enable new design freedoms and provide opportunities to explore novel structural typologies. While further research is required in this respect, we are commonly used to using concrete together with reinforcement, relying it to control cracking due to restrained deformations, and to comply with established structural safety requirements.

There have been multiple state-of-the-art reports regarding reinforcement strategies in digital fabrication with concrete. Under this chapter we present some of these strategies that are more relevant for 3D concrete printing, including the ones that have been developed at TU/e. For a more detailed and extensive overview please refer to the original state of art reports [73, 74].

Each strategy offers distinct advantages and limitations in terms of structural performance, process compatibility, geometric freedom, and cost. Despite numerous concepts, all techniques remain at relatively low Technology Readiness Levels (TRLs), highlighting the complexity of merging reinforcement with layered manufacturing.

Developing reinforcement for 3DCP requires a dual perspective: (1) understanding the technological constraints of integrating reinforcement into an automated, layer-wise fabrication process, and (2) assessing the structural behaviour of the resulting composite system.

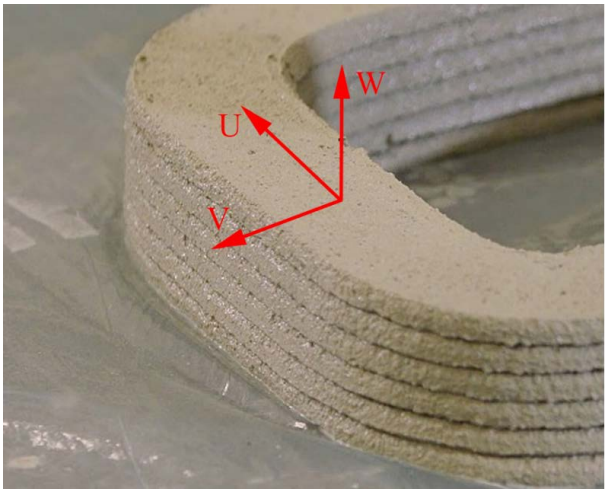

Figure 4.1: Illustration of the u-, v-, and w-directions in extrusion-based 3D printed concrete.

Unlike conventional construction—where reinforcement is first positioned and concrete is subsequently cast—3DCP typically reverses this sequence and places reinforcement after or during extrusion. Concrete layers may be extruded before reinforcement insertion [75], concurrently with it [76], or even around pre-placed reinforcement systems, although the latter approach significantly constrains geometric freedom and often results in uncertain bond behaviour due to limited mechanical interlock. Owing to the continuous, layer-wise nature of extrusion, the printed filament passes through different stages of structuration as the element grows [77]. This creates a time-dependent "window of opportunity" for introducing reinforcement. Within this window, adequate bond and interfacial adhesion must develop between the reinforcement and the evolving concrete microstructure—a process highly sensitive to age-dependent material parameters such as yield stress, elastic modulus, and structural build-up kinetics [78].

Automated reinforcement placement therefore becomes essential—not only to ensure precision, but also to synchronise timing, insertion mechanics, and reinforcement orientation with the evolving concrete state.

Furthermore, the layered nature of 3DCP introduces inherent anisotropy: interfaces between subsequent and adjacent layers exhibit mechanical behaviour that differs markedly from the material deposition direction (Figure 4.1). This anisotropic response does not only affect structural performance—it also fundamentally complicates the integration of reinforcement. Because each principal direction in a printed element exhibits distinct mechanical characteristics, adequate structural performance demands reinforcement in multiple orientations. However, embedding reinforcement systems that effectively address these different directional demands remains a major challenge. While along-layer strategies—such as cable-based reinforcement [76]—show clear promise, providing reliable reinforcement across interlayer interfaces is still largely unresolved [79, 80, 81].

Moreover, the thin-walled structural typologies typical of printed elements require not only primary reinforcement in the dominant load direction but also adequate secondary reinforcement to resist splitting tensile forces and to ensure sufficient struc-

tural cover.

This challenge is illustrated in Figure 4.2. Here, helical (screw-type) reinforcement was used in combination with either strain-hardening cementitious composites (SHCC) or plain mortar. When combined with SHCC, the strategy proved effective: the high tensile capacity of the discrete helical bars was complemented by the ductility and confinement provided by the SHCC matrix, resulting in improved bending performance. Integration of such helical reinforcement using the Automated Screwing Device has also been successfully demonstrated for automated production workflows.

However, when the same helical reinforcement was embedded in plain mortar, the elements exhibited premature splitting failure during bending. The lack of confinement led to abrupt cracking along the screw trajectory, preventing the specimens from reaching their full bending moment capacity. This highlights that reinforcement concepts for 3DCP must be designed as combined material–reinforcement systems, where confinement, bond behaviour, and multiaxial reinforcement needs are addressed simultaneously.

(a) Plain mortar screw (PM-screw).

(b) SHCC Screw (SHCC-screw).

Figure 4.2: Images of staircase step shaped test elements subjected to bending, showing that the combination of screw-type (helical) reinforcement with plain mortar (PM) resulted in premature splitting failure due to insufficient confinement—an issue that was not observed when using strain-hardening cementitious composites (SHCC) mixes.

Taken together, these developments indicate that integrating reinforcement into

3DCP is not simply a matter of transferring existing reinforced concrete practice into a new manufacturing process. Instead, it demands a fundamental reconsideration of how material, process, and force flow interact within digitally fabricated, layered concrete structures—thereby opening new perspectives for form-optimised, structurally efficient reinforced concrete in the age of digital fabrication.

State-of-the-art reviews classify existing reinforcement approaches into three main categories: (1) *Post-installed techniques* (2) *Pre-installed methods* (3) *Process-integrated approaches*

4.1 Post-installed techniques

4.1.1 Grouted bars

Post-installed reinforcement using grouted steel bars is among the earliest and most widely applied reinforcement strategies in extrusion-based 3DCP. After printing the structural shell, vertical or inclined holes are either printed as voids or drilled afterwards, enabling the subsequent insertion of reinforcing bars which are then bonded to the structure using grout or high-performance mortars. This technique closely mirrors conventional reinforced concrete construction and therefore benefits from a high level of technological maturity, predictable structural performance, and straightforward compliance with existing design codes for reinforced concrete.

Early printed houses and demonstration projects—such as those by Apis Cor and WinSun—make extensive use of vertical post-installed bars for columns and wall reinforcement [82, 83], seen on Figure 4.3. These implementations rely on drilling or placing ducts during printing and subsequently grouting the reinforcement into position. The state-of-the-art review by Mechtcherine et al. [74] includes grouted bar systems as part of the post-installed reinforcement category and summarises their main advantages: they satisfy conventional structural requirements (load-bearing capacity, ductility, crack control, robustness) and are immediately compatible with engineering design practice, albeit requiring post-processing steps after printing.

Figure 4.3: From left to right: drilling a hole for chemical anchoring of the rebar; inserting the rebar into the cavity after the structure has been printed; and subsequently casting or grouting the reinforcement to anchor it to the floor. Images taken from a video from Apis Cor homepage [82].

In practice, printed houses routinely rely on this technique: vertical alignment ducts are incorporated into walls during printing, and afterwards reinforcement bars are

inserted and filled with grout to create reinforced wall cores—analogous to reinforced masonry.

This post-installed reinforcement approach is particularly suitable for load-bearing walls and vertical elements such as lintels and columns, ensuring the required tensile capacity and enabling compliance with structural codes. Its main advantages lie in its compatibility with conventional reinforced concrete practice, the robustness and reliability of the bar–concrete bond, and the fact that reinforcement placement is independent of the printing process itself. However, these benefits come at the cost of additional post-processing operations and a reduction in geometric freedom, especially when large bar diameters are required or where grout placement may introduce voids or interface defects.

4.1.2 Post-tensioning

Post-tensioning has emerged as one of the most robust post-installed reinforcement strategies for structural 3D-printed concrete. Instead of embedding reinforcement during printing, printed segments are first fabricated and subsequently assembled and prestressed, enabling continuous tensile capacity along the full structural length. The best-known example is the 3D-printed bicycle bridge in the Netherlands, where six hollow printed segments were joined and prestressed using unbonded steel strands running through internal ducts [67, 84, 85]. This approach demonstrated that printed components can safely transfer prestressing forces and remain structurally intact even under repeated loading cycles. Similarly, the more recent Tor Alva tower showcases how post-tensioning can be integrated into a multi-storey 3D-printed structural system. In this project, top levels of the tower were post-tensioned the printed to their respective end plates, seen on Figure 4.4.

Figure 4.4: On the left the post tensioned bridge elements of the 3D-printed bibycle bridge in the Netherlands. On the right, the columns of the upper levels of the Tor Alva tower are post-tensioned using a central high-tension steel bar (⌀ 12 mm). These bars are greased and housed in plastic sleeves, with their anchorages integrated into the prefabricated concrete elements [86].

A similar strategy was used by TU Gent where combined post-tensioning with topology optimisation to design lightweight printed girders, in which both concrete geometry and tendon trajectories were optimised jointly [87], seen on Figure 4.5 These

studies highlight that post-tensioning is well suited to segmented, assembled 3D-printed structures because it bypasses the need for fresh-state bond, accommodates large-scale load transfer, and imposes almost no constraints on printing direction or filament geometry.

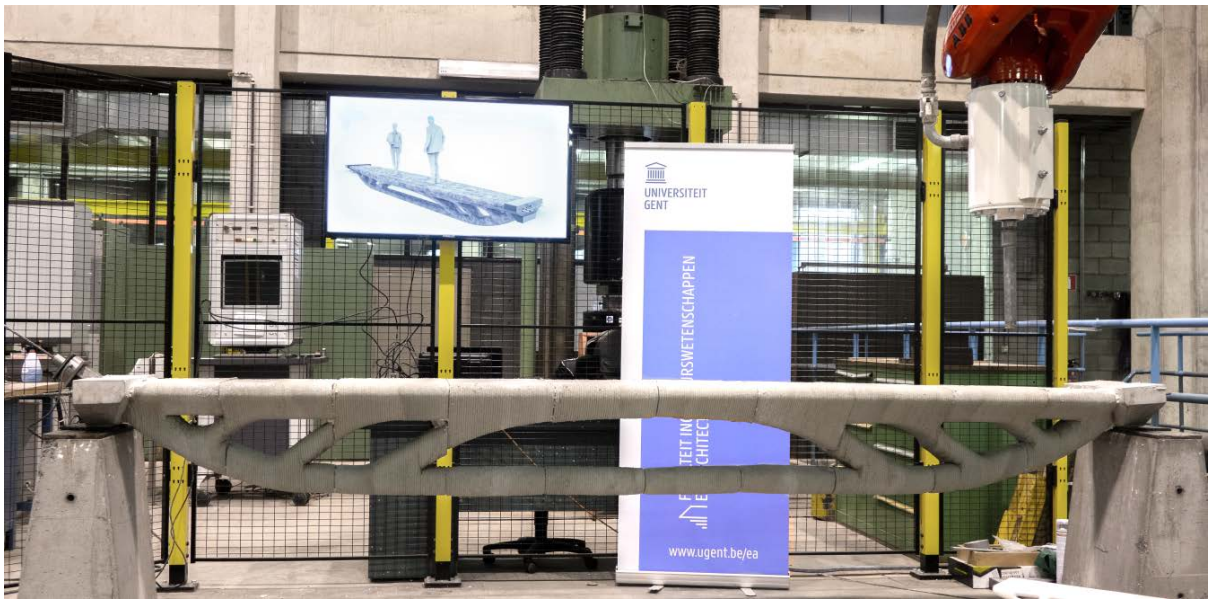

Figure 4.5: Post-tensioned 3D-printed concrete girder demonstrating the integration of topology optimisation and extrusion-based 3D concrete printing to create efficient structural forms, taken from [87].

However, post-tensioning introduces additional process steps—segment fabrication, surface preparation, assembly, duct alignment, and stressing—that are typically carried out after printing and require conventional construction equipment. Full automation has not yet been demonstrated, but the method remains one of the few reinforcement strategies already validated at structural scale.

4.1.3 External reinforcement systems

External reinforcement systems for 3DCP refer to strategies in which reinforcing elements are applied outside the printed concrete rather than embedded within it. Although less frequently explored than other reinforcement classes, several state-of-the-art studies identify external reinforcement as a viable solution particularly for segmental structures, printed trusses, and post-processed load-bearing elements.

A representative example is reported by Asprone et al. [88]: a 3D-printed truss component where diagonal tension members are added after printing, seen on Figure 4.6. In this system, the concrete truss geometry is first printed, and cavities for anchorage are subsequently cast in. Steel bars—acting as external tension ties—are then anchored into these nodes and post-tensioned to stabilise the lightweight printed geometry. This method allows the printed concrete to carry primarily compression, with the external steel resisting tension, thereby extending the structural applicability of unreinforced printed components.

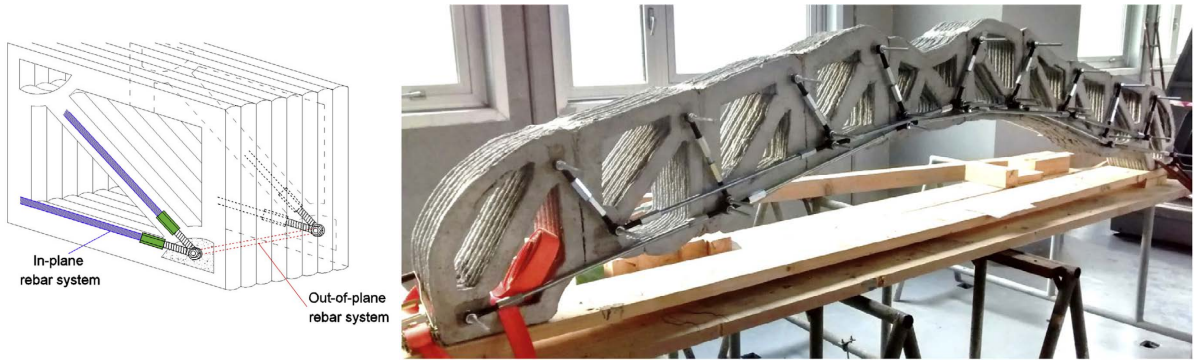

Figure 4.6: External reinforcement strategies for 3D-printed concrete. Left: in-plane and out-of-plane rebar systems that can be attached externally to enhance structural capacity. Right: an optimised 3D-printed beam with a variable cross-section demonstrating how geometry can be tailored to structural demand, taken from [88].

Overall, external reinforcement systems offer several advantages: they do not constrain the extrusion process, they can be installed after hardening, and they enable effective tension-resisting capacity even in highly optimised or porous printed geometries. Their main drawbacks include the requirement for post-processing, dependency on accurate interface preparation, and potential local stress concentrations at anchor points.

4.2 Pre-installed techniques

4.2.1 Print-around existing reinforcement

Printing concrete around pre-installed reinforcement is one of the earliest and most intuitive strategies explored in 3DCP. In this approach, reinforcement cages, meshes, or individual bars are positioned first, after which the printing system deposits concrete around them. This creates a two-step process in which the reinforcement can even act as an internal scaffold of sorts. An example of this approach is from the Dutch company Vertico [89], which performed 3D concrete printing directly onto pre-assembled wire-frame reinforcement structures, seen on Figure 4.7.

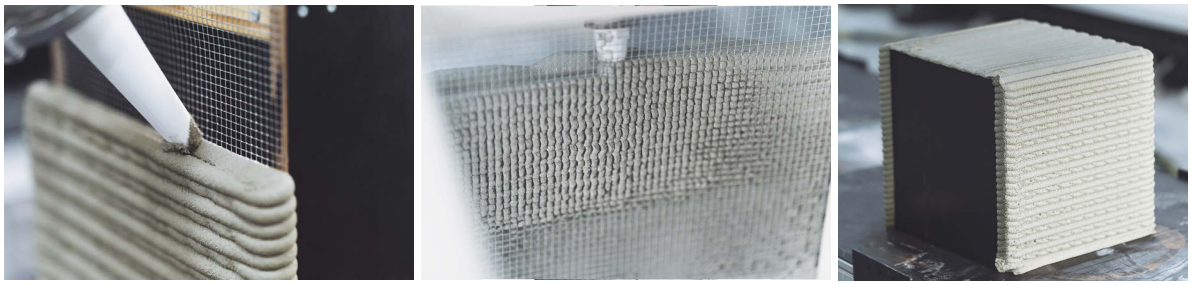

Figure 4.7: 3D concrete printing directly onto pre-assembled wire-frame reinforcement structures by Vertico [89].

Another example, where Huashang Tengda's on-site printing system employed a split nozzle capable of depositing concrete from both sides around vertically

mounted steel meshes, enabling full-height wall construction by stacking successive mesh layers as printing progressed [90]. More advanced strategies, such as the Mesh Mould process developed at ETH Zürich, fabricate complex steel meshes robotically before filling them with concrete, effectively reversing the conventional sequence between reinforcement placement and concrete shaping [91], seen on Figure 4.8. The latter however is mostly used for

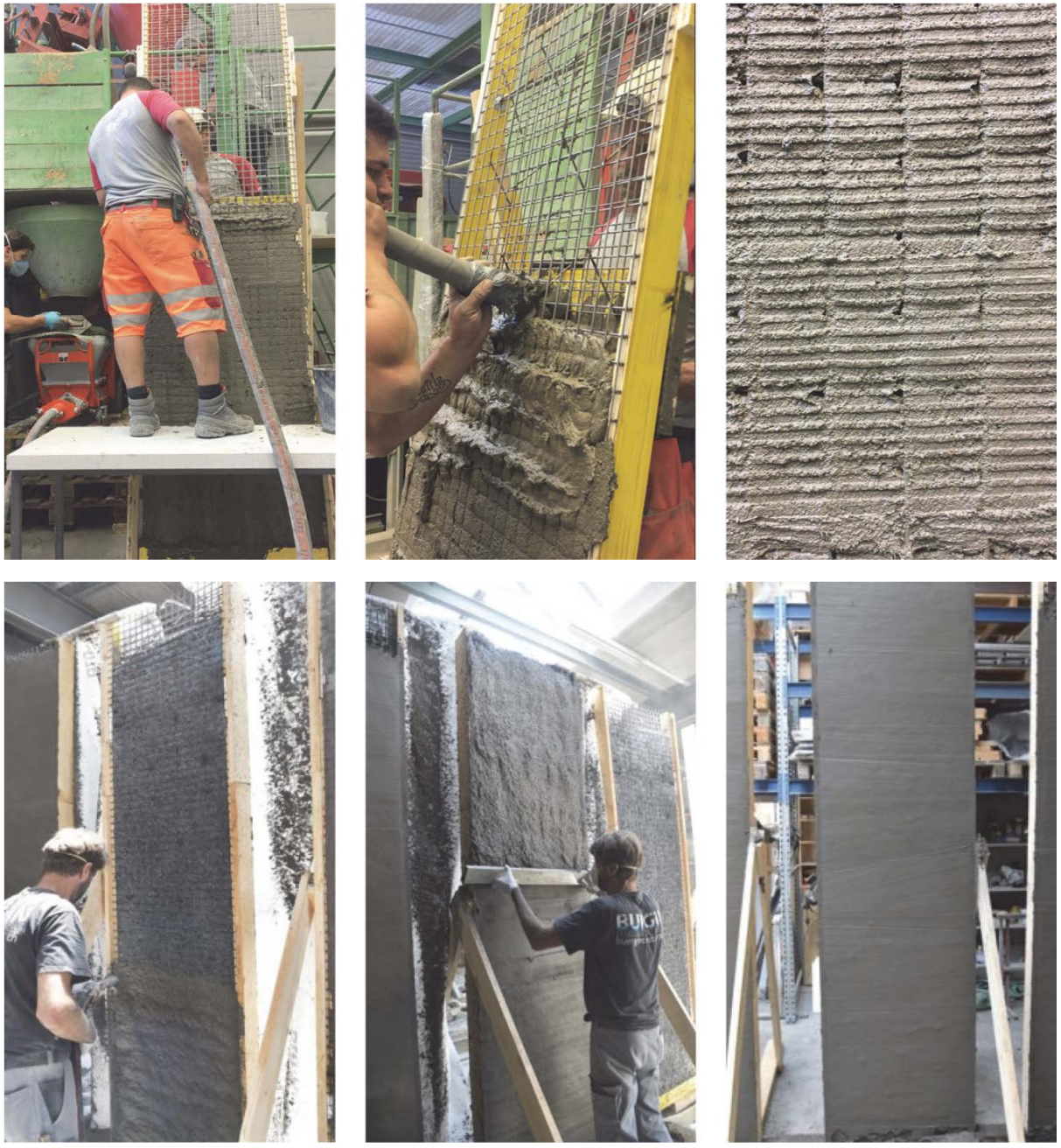

Figure 4.8: Filling process of the mesh prototypes used in the DFAB HOUSE investigations. Concrete is first introduced into the manually assembled steel mesh—tilted by 10° to simulate double-curvature overhangs—and allowed to flow through the interconnected cells. After filling, the mesh surface is covered with a fine cement mortar to create a continuous outer layer prior to subsequent structural testing, taken from [92].

Overall, print-around methods offer robust structural performance using conventional reinforcement layouts and materials, while maintaining compatibility with established design codes. Their primary limitation remains the reduced geometric freedom and increased setup effort associated with placing large reinforcement assemblies before printing.

4.2.2 Pre-assembled reinforcement cages

Pre-assembled reinforcement cages offer a straightforward way to combine conventional reinforced concrete practice with 3D concrete printing. In this approach, the reinforcement is fabricated prior to printing—either as standard steel cages or as customised assemblies—and subsequently encased by the printed material. The printed concrete effectively acts as stay-in-place formwork, or as a shaped cover layer around the cage.

For example work by Gebhard [93], investigated reinforcement strategies for digital fabrication with concrete by developing, fabricating, and experimentally testing structural elements produced with 3D concrete printing. His work included the integration of pre-assembled reinforcement cages into printed geometries, the optimisation of printable structural topologies, and the validation of these systems through full-scale load tests—demonstrating the feasibility and challenges of combining conventional reinforcement with digitally fabricated concrete components. One of these T beams can be seen produced on Figure 4.9.

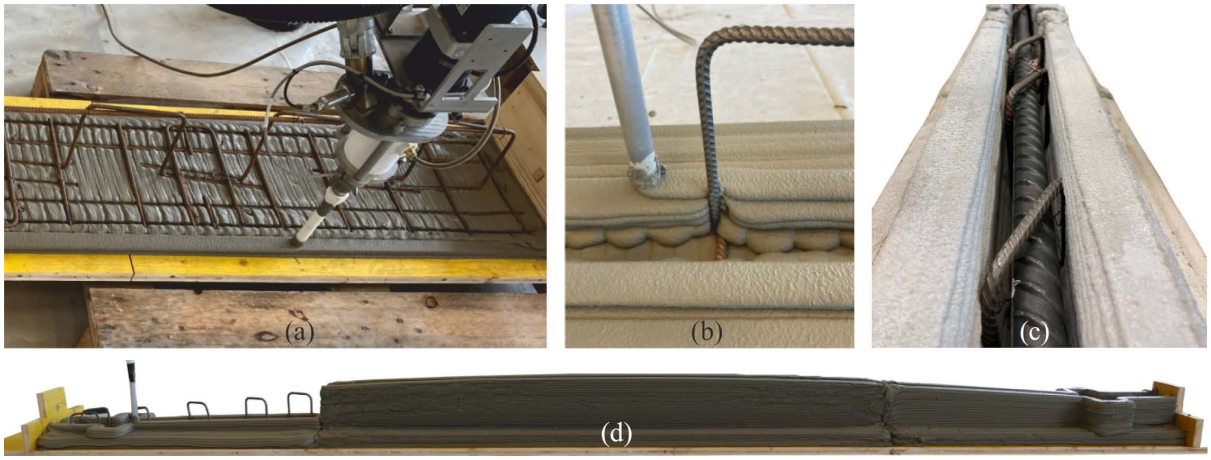

Figure 4.9: Images from the fabrication process: (a) Printing of the second half of the flange after placement of the pre-assembled reinforcement cage; (b) Close-up of the print head passing adjacent to a U-shaped stirrup; (c) View of the web with the installed bending reinforcement prior to grouting; (d) Side view of the full beam during the printing of the final segment., taken from [93]

Another project from TU Darmstadt, seen on Figure 4.10, demonstrates the use of 3D-printed formwork to construct a ribbed slab with an optimised structural topology. The printed formwork not only reproduces the rib geometry but also visually conveys the internal force flow, illustrating how additive manufacturing enables complex shapes that are difficult to achieve with conventional methods. The structural design was developed by students of Technische Universität Darmstadt under the

supervision of Prof. Stefan Schäfer and Nikola Bisevac, with support from the Steel Construction Department and industry partners.

Figure 4.10: Printed formwork demonstrator developed at Technische Universität Darmstadt.

The main advantages of pre-assembled cages are their high structural reliability, continuity of reinforcement in multiple directions, and compatibility with existing design codes. They enable the production of fully reinforced structural elements without requiring in-process placement of bars. However, geometric freedom is constrained by the cage dimensions, and full automation remains challenging, particularly for free-form reinforcement geometries. Advanced robotic concepts such as Mesh Mould partially address this by fabricating freeform cages robotically prior to concreting, but these systems remain at low technological readiness levels [74].

4.3 Process-integrated techniques

4.3.1 Entrainment reinforcement

Process-integrated entrainment refers to the continuous feeding of linear reinforcement directly into the fresh filament during extrusion. This concept was first demonstrated at TU Eindhoven, seen on Figure 4.11, where a high-strength steel cable was mechanically inserted into the filament immediately prior to deposition [94, 74]. The approach enables fully automated placement of reinforcement without interrupting the printing process and preserves the geometric freedom characteristic of extrusion-based 3DCP. Its effectiveness, however, is inherently unidirectional, providing tensile capacity primarily along the printing path. Bond behaviour remains a critical design aspect: experimental work by Bos et al. [95] showed that reliable steel–matrix interaction can be achieved, but performance depends on cable surface chemistry and the rheological behaviour of the matrix around the entrained element.

Figure 4.11: Reinforcement Entrainment Device (RED) developed at TU Eindhoven to add steel cable reinforcement into the printed concrete

An alternative is the use of mineral-impregnated carbon-fibre (MCF) rovings developed at TU Dresden, which were shown to bond more effectively with cementitious matrices than polymer-bound carbon fibres and can be shaped robotically in fresh state [96, 97], see on Figure 4.12. MCF can be inserted either between layers (contiguous placement) or directly through the printhead into the filament, allowing highly flexible reinforcement layouts. While mechanically promising, entrainment methods remain limited to reinforcement aligned with the extrusion direction and therefore typically require complementary strategies to ensure out-of-plane performance.

Figure 4.12: Integration of mineral-impregnated carbon-fibre (MCF) rovings into the extrusion process, taken from [97]

Flow-based pultrusion is an innovative reinforcement method for extrusion-based additive manufacturing in which continuous fibers are impregnated and transported solely by the rheological action of a yield-stress cementitious matrix. Unlike conventional pultrusion, where external pulling mechanisms drive the fibers through a die, this process exploits the flow properties of the fresh material to achieve fiber impregnation and consolidation. The extruded, continuously reinforced filament can then be robotically deposited in space, similar to standard 3D concrete printing. This introduces specific requirements for fresh-state behavior—such as adequate yield

stress, viscosity, and pressure-driven fiber transport—which must align with existing strategies used in unreinforced extrusion processes. The method and its implications for adapting pultrusion to current printing technologies are described by Demont et al. [98], and illustrated on Figure 4.13.

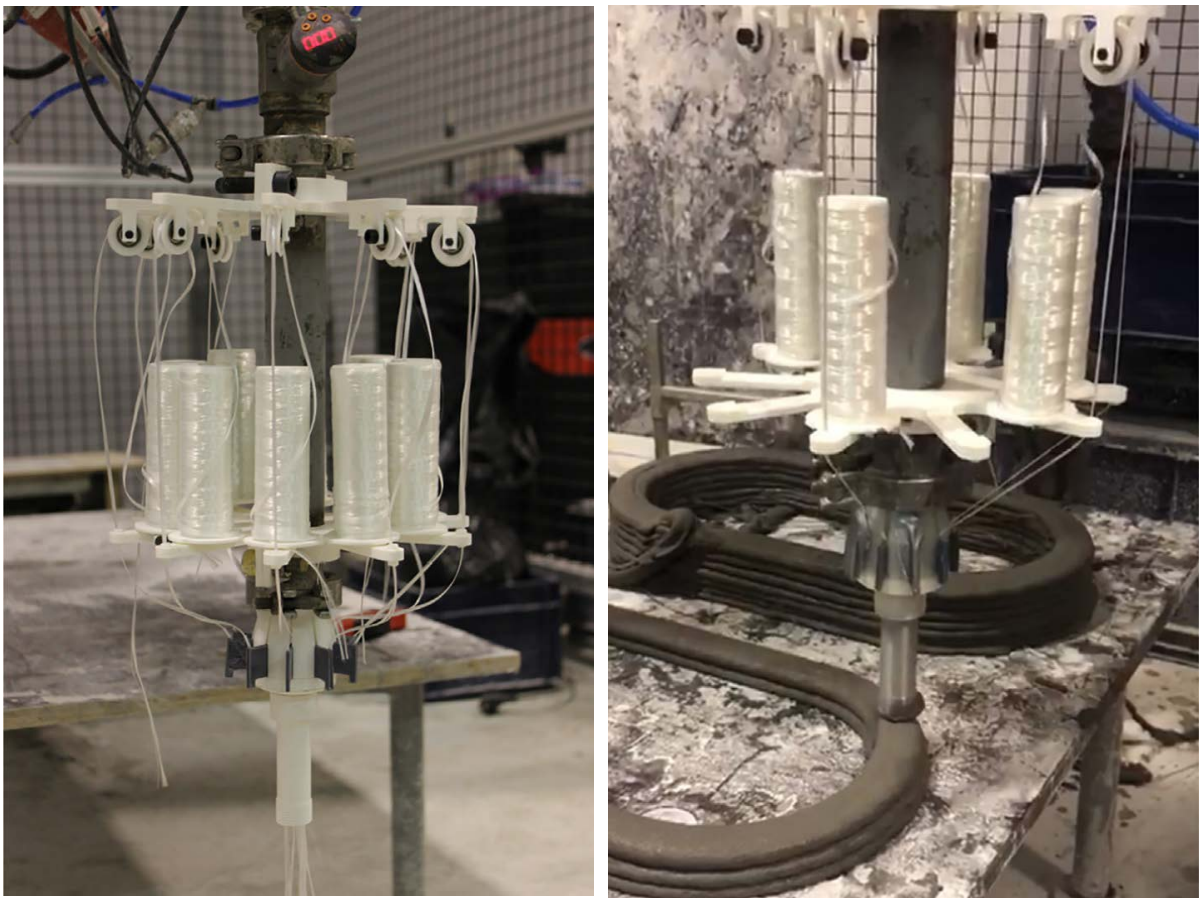

Figure 4.13: Experimental setup of the flow-based pultrusion device, in which continuous fiber rovings are impregnated and transported through by the rheological action of a yield-stress cementitious matrix, taken from [98].

4.3.2 Reinforcement between layers

Another process-integrated strategy is the placement of reinforcement between successive printed layers. This method has been applied using steel bars, metallic meshes, or fibre-based grids and textiles, seen on Figure 4.14. Early work demonstrated manual placement of straight bars between layers, later covered by the subsequent filament [74]. More advanced variants include automated feeders for placing reinforcement directly onto the freshly extruded filament before it is covered by the next layer [96]. These approaches improve tensile capacity within the print plane and can mitigate interlayer weaknesses, particularly when reinforcement crosses or stitches adjacent layers.

Figure 4.14: Examples of reinforcement strategies in extrusion-based 3D concrete printing. (left) Demonstration of placing reinforcement between layers during fabrication at TU Eindhoven, enabling contiguous in-layer strengthening along the printing path; (right) Integration concept illustrated by the V2 Vesta concrete 3D printer, adapted from [99].

Bond behaviour between reinforcement and printed concrete has been studied in several contexts. Baz et al. [100] showed that steel bars embedded in printed elements can achieve bond performance comparable to cast concrete if grouting or high-quality repair mortars are used to compensate for surface irregularities or interlayer voids. This highlights the importance of local matrix quality and interface consolidation in process-integrated reinforcement strategies.

4.3.3 Cross-layer reinforcement

Cross-layer reinforcement refers to techniques that actively penetrate fresh printed layers to provide mechanical continuity across the weak interlayer interfaces characteristic of extrusion-based 3DCP. Unlike reinforcement methods aligned with the print direction, these techniques directly target the v-direction (layer stacking direction), although can be also placed in other directions.

Recent studies demonstrate that inserting discrete elements—such as nails, bars, or screws—into fresh layers can significantly enhance interlayer bond if penetration occurs within an appropriate time window. Early work by Perrot et al. [101] showed that short steel nails driven vertically or at an angle through several freshly printed layers increased flexural capacity by up to 50%, with inclined or crossed configurations outperforming vertical nails. Their results also highlighted the strong influence of penetration orientation and surface condition (smooth vs. rusty) on post-peak behaviour.

Extending this concept, Marchment and Sanjayan [102] examined the bond mechanism of deformed reinforcing bars manually driven through multiple layers. Pull-out tests revealed that bond strength decreases with shallower penetration, as the upper sections of the bar interact with less consolidated material. Deeper penetration tended to restore bond behaviour comparable to cast concrete, although the mechanical disturbance introduced during insertion remains a limiting factor.

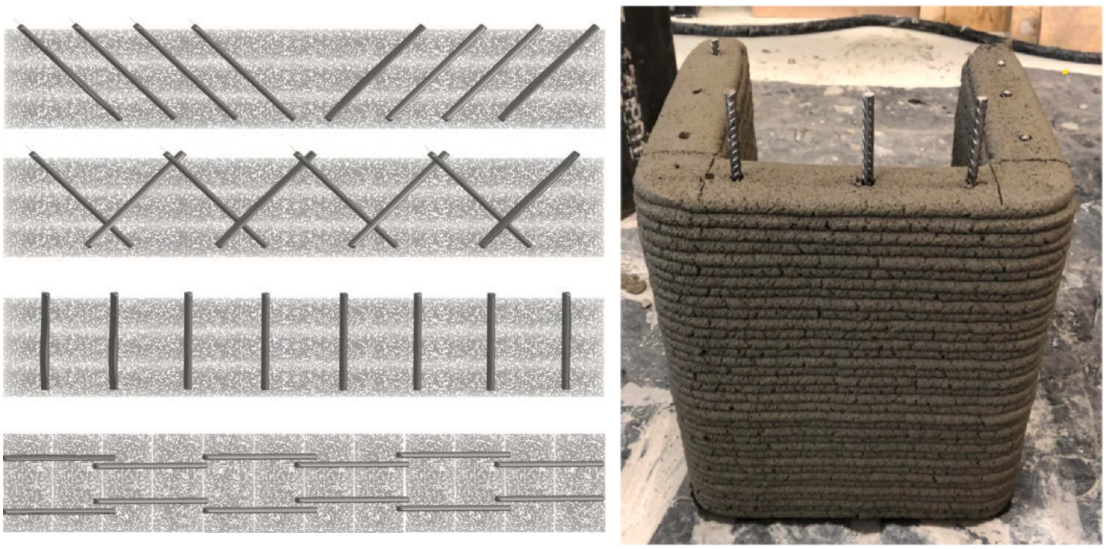

Figure 4.15: Left: Example of nail-type penetration in layered 3D-printed concrete. Right: Vertical bar-penetration reinforcement method, where a deformed steel bar is inserted through freshly printed layers to enable in-process reinforcement placement.

An alternative approach uses screw-type (helical) reinforcement, which is inserted into fresh layers through combined translational and rotational movement. Hass [12] demonstrated that this method produces superior mechanical interlock and avoids the interfacial voids typically associated with simple bar penetration. Pull-out and tension-tie tests demonstrated that the helical reinforcement exhibited substantially higher bond strength than conventional bars, primarily due to the pronounced surface indentation visible in Figure 4.16. Micro-CT scans confirmed the absence of significant voids or cavities around the embedded reinforcement. Conventional bond theory—used to estimate crack spacing and splitting tensile forces—was found to be applicable to this system. Moreover, the reinforcement method shows strong potential for automation through a robotic end-effector, the Automated Screwing Device (Figure 4.17).

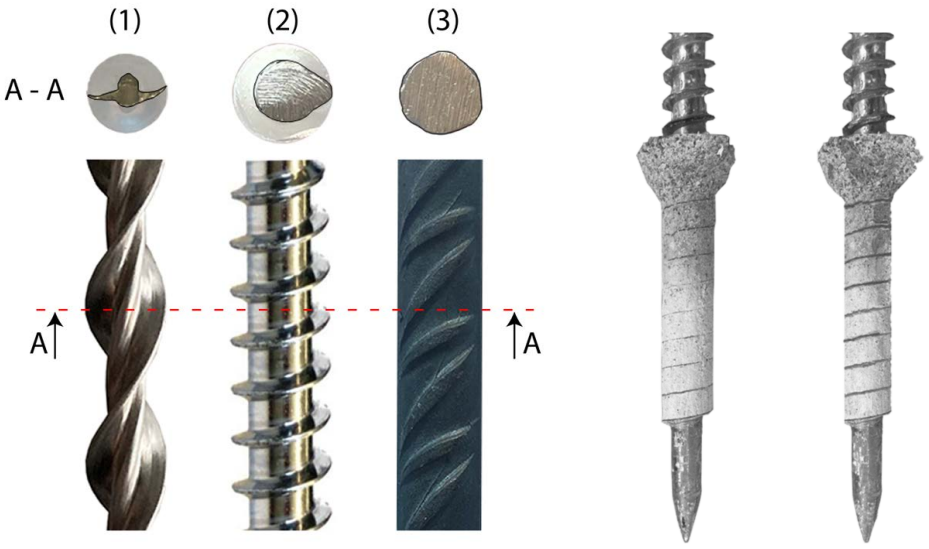

Figure 4.16: (left) illustration of different reinforcement cross section and profile types, all tested in [12], and (right) reinfrocement surface after direct pull-out tests.

Further investigations using vertical insertion of short steel or carbon bars in Shotcrete-3D-Printing (SC3DP) [103] confirm that direct penetration often results in cavities and reduced bond; however, augmenting the process with local grouting or screw-like motion substantially improves the interface quality. CT imaging from these studies reveals that bond behaviour is highly sensitive to the local fresh-state rheology and the insertion kinematics.

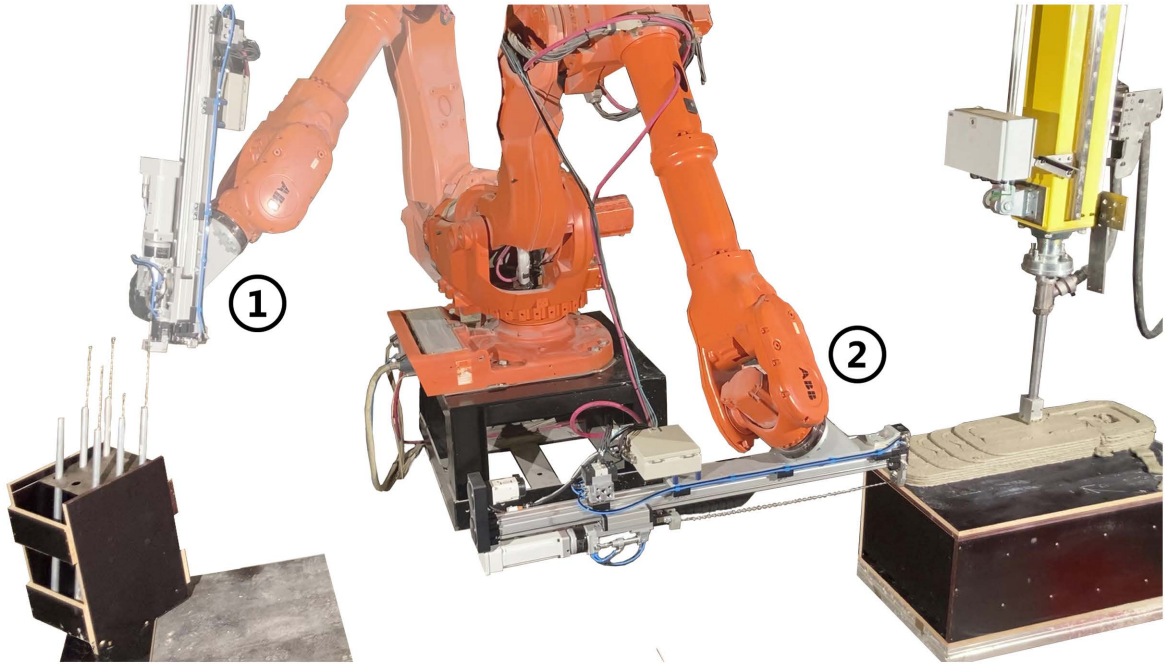

Figure 4.17: Automated Screwing Device during production, illustrating automated pick and placement sequence of helical reinforcement [12]

Taken together, cross-layer reinforcement strategies provide one of the few viable methods for strengthening the inherently weak interlayer direction in 3DCP. Their effectiveness depends on precise timing, control of insertion mechanics, and material properties during early hydration. While promising, these methods currently remain at low to mid TRLs, and their practical implementation will rely on robotic placement systems capable of reliable, defect-free penetration.

4.3.4 Fibre reinforcement

The relevance of fibre reinforcement in 3D concrete printing arises from several intrinsic vulnerabilities of printed structures and from the practical constraints of the printing process itself. As previously discussed, 3D-printed elements are typically thin-walled, filigree, and highly sensitive to shrinkage-induced cracking, with cracks propagating easily through the full section and compromising impact resistance and structural integrity. Conventional printable mortars are inherently brittle and provide almost no post-cracking resistance, while the integration of continuous reinforcement across all directions is severely restricted by the layer-wise deposition process. Tensile stresses—arising from external loading, internal force redistribution, restrained deformations, or shrinkage—are therefore unavoidable, yet cross-layer reinforcement remains difficult to achieve reliably.

Short fibres offer one of the simplest and most widely applicable reinforcement strategies for extrusion-based 3DCP. They can be blended into the dry constituents, added during mixing, or introduced immediately before extrusion, though pumpability and extrudability constraints typically limit fibre length and volume fraction [85]. A wide range of fibres has been used, including steel, carbon, glass, and polymeric fibres such as PVA or PE, each contributing differently to tensile strength, crack control, toughness, and energy absorption. During extrusion, fibres tend to align in the printing direction, producing pronounced anisotropy in the hardened material. This behaviour has been documented for carbon, glass and basalt fibres [104], short straight steel fibres [105], and various UHPFRC/SHCC systems [106, 107]. While this preferential alignment enhances tensile and flexural strength along the filament path, fibres generally do not bridge interlayer interfaces, meaning that out-of-plane reinforcement remains limited unless specialised filament geometries (e.g., tongue-and-groove extrusions) are used [108].

Despite these limitations, fibre reinforcement directly addresses many of the material-scale deficiencies of printable mortars. Even at modest dosages, fibres bridge microcracks, enhance tensile ductility, delay crack localisation, and significantly increase toughness—benefits particularly valuable for thin printed sections where reinforcement placement freedom is highly restricted. Because fibres are distributed throughout the matrix, they also provide crack control in regions where mechanical reinforcement cannot be inserted, supporting early-age stability, transport, and handling. This material-level ductility aligns naturally with the design philosophy increasingly advocated for 3DCP: exploiting compression-dominant geometries while mitigating unavoidable tensile effects through controlled distributed cracking rather than relying solely on discrete reinforcement.

Strain-hardening cementitious composites (SHCC) further extend these advantages.

Their ability to form multiple fine cracks while sustaining load beyond first cracking provides a stabilising mechanism well suited to the anisotropic, layered nature of 3DCP. This was demonstrated at structural scale in the production of spiral staircase elements, where SHCC acted as the primary reinforcement mechanism. These elements exhibited markedly improved bending resistance and ductility compared to conventional printable mortars. Nonetheless, the tensile strength of 3DP-SHCC alone was insufficient for bending-dominated components of this scale, and the anisotropy observed in material testing was reflected in the structural behaviour of the printed elements—necessitating careful design of the print path for structurally active SHCC components.

Beyond its role as primary reinforcement, SHCC also performs effectively as secondary reinforcement. Its distributed fibre network homogenises crack patterns, enhances confinement, and stabilises the structural response when combined with discrete reinforcement. This was demonstrated in the successful combination of helical (screw-type) reinforcement with 3DP-SHCC: the helical reinforcement supplied substantial tensile strength and interlayer anchorage, while SHCC provided ductility, confinement, and distributed crack control. When used synergistically, these two reinforcement mechanisms achieved a significantly higher bending capacity than either system could provide individually, forming a reinforcement strategy that is naturally compatible with the anisotropic and layered architecture of extrusion-based 3DCP.

The practical implementation of SHCC in 3D printing, however, also poses challenges at the process level. In this research, a batch-mixed printing workflow was employed, but several manual steps—such as dosing viscosity-modifying agents and loading the printer reservoir—highlight the limitations of batch mixing for industrial use. While upscaling batch processes is possible, it is likely to remain labour-intensive, costly, and material-specific. Continuous mixing is therefore desirable for industrial application, yet most current 3DCP systems feature small mixing chambers that cannot generate sufficient mixing energy for fibre-rich SHCC mixes. Adaptations to increase mixing energy are required, and alternative pumping technologies such as peristaltic pumps may offer greater compatibility with these mortars than conventional rotor–stator (progressive cavity) pumps, which impose restrictive limits on viscosity and fibre content.

Bibliography

[1] International Energy Agency (IEA). *Global Status Report for Buildings and Construction 2021*. Confirms that total global floor area is projected to double by 2060, driven by urbanisation and population growth. IEA, Global Alliance for Buildings, and Construction, 2021. URL: https://www.iea.org/reports/global-status-report-for-buildings-and-construction-2021.

[2] United Nations Environment Programme (UNEP) and International Energy Agency (IEA). *Towards a Zero-Emission, Efficient and Resilient Buildings and Construction Sector: Global Status Report 2017*. Reports that the world's building floor area is expected to double by 2060, adding over 230 billion m^2. Global Alliance for Buildings and Construction, 2017. URL: https://globalabc.org/resources/publications/global-status-report-2017.

[3] United Nations Department of Economic and Social Affairs. *World Population Prospects 2022: Summary of Results*. Projects that Africa's population will triple by 2100, requiring major expansion of housing, infrastructure, and energy systems. United Nations, DESA, Population Division, 2022. URL: https://population.un.org/wpp/.

[4] McKinsey & Company. *Delivering on Construction Productivity Is No Longer Optional*. Report. McKinsey Global Institute, 2024.

[5] Automotive Online. *Robots on Automotive Assembly Line*. https://www.automotive-online.nl/wp-content/uploads/2019/07/Robots.jpeg. Accessed: 2025-12-09. 2019.

[6] LinkedIn. *LinkedIn Shared Image*. https://media.licdn.com/dms/image/v2/C5112AQEpeiRMr4lR1g/article-cover_image-shrink_600_2000/article-cover_image-shrink_600_2000/0/1576170662086?e=2147483647&v=beta&t=ucwQpW1602COHLY6PGC8ndz8Z_O28GMUfXQH8ExAfUs. Accessed: 2025-12-09. 2020.

[7] T. Wangler et al. "Digital concrete: A review". In: *Cement and Concrete Research* 123 (2019), p. 105780. DOI: 10.1016/j.cemconres.2019.105780.

[8] R.J.M. Wolfs. "The status quo of 3D concrete printing: Are we there yet?" In: *RILEM Technical Letters* 8 (2023), pp. 182–189. DOI: 10.21809/rilemtechlett.2023.197.

[9] CROW, TU Eindhoven, and Witteveen+Bos. *CROW-CUR Richtlijn 5:2023 – 3D-betonprinten*. CROW, Ede, 2024. ISBN: 9789066287112.

[10] D. H. Bos. "Quality Engineering and Control for Digital Fabrication with Concrete". PhD Thesis. Eindhoven University of Technology, 2024.

[11] United Nations Environment Programme. *2023 Global Status Report for Buildings and Construction: Towards a Zero-Emission, Efficient and Resilient Buildings and Construction Sector*. ISBN 978-92-807-4045-1. Nairobi, Kenya: UNEP,

2023. URL: https://www.unep.org/resources/publication/global-status-report-buildings-and-construction-2023.

[12] L. Hass. "Helical Reinforcement in 3D Printed Concrete: Development and Characterization of a Novel Reinforcement Technique". PhD Thesis. Eindhoven University of Technology, 2025.

[13] Arjen Deetman et al. "An in-line dye tracer experiment to measure the residence time in continuous concrete processing". In: *Materials and Structures* 57.104 (2024). Open Access under CC BY 4.0 license, pp. 1–18. DOI: 10.1617/s11527-024-02378-y. URL: https://doi.org/10.1617/s11527-024-02378-y.

[14] Derk H. Bos and Rob J. M. Wolfs. "A Quality Control Framework for Digital Fabrication with Concrete". In: *RILEM Technical Letters* 8 (2023). Open Access under CC BY 4.0 license, pp. 106–112. DOI: 10.21809/rilemtechlett.2023.181. URL: https://doi.org/10.21809/rilemtechlett.2023.181.

[15] Derk Bos et al. "Development of the On-Line Gravity-Induced Compression Test: "The Inverse Slugs Test"". In: *Proceedings of the Fourth RILEM International Conference on Concrete and Digital Fabrication (Digital Concrete 2024)*. Ed. by Dennis Lowke et al. Vol. 53. RILEM Bookseries. Presented at Digital Concrete 2024, RILEM Bookseries Vol. 53. Springer Nature Switzerland, 2024, pp. 166–173. DOI: 10.1007/978-3-031-70031-6_20. URL: https://doi.org/10.1007/978-3-031-70031-6_20.

[16] R. J. M. Wolfs, F. P. Bos, and T. A. M. Salet. "Early age mechanical behaviour of 3D printed concrete: Numerical modelling and experimental testing". In: *Cement and Concrete Research* 106 (Apr. 2018), pp. 103–116. DOI: 10.1016/j.cemconres.2018.02.001.

[17] Y. Jacquet, A. Perrot, and V. Picandet. "Assessment of asymmetrical rheological behavior of cementitious material for 3D printing application". In: *Cement and Concrete Research* 140 (Feb. 2021), p. 106305. DOI: 10.1016/j.cemconres.2020.106305.

[18] *NEN-EN 1015-3: Methods of test for mortar for masonry – Part 3: Determination of consistence of fresh mortar (by flow table)*. Nederlands Normalisatie-instituut, 2020.

[19] R. J. M. Wolfs, F. P. Bos, and T. A. M. Salet. "Triaxial compression testing on early age concrete for numerical analysis of 3D concrete printing". In: *Cement and Concrete Composites* 104 (Nov. 2019), p. 103344. DOI: 10.1016/j.cemconcomp.2019.103344.

[20] L. K. Mettler et al. "Evolution of strength and failure of SCC during early hydration". In: *Cement and Concrete Research* 89 (Nov. 2016), pp. 288–296. DOI: 10.1016/j.cemconres.2016.09.004.

[21] *ASTM D8121: Standard Test Method for Approximating the Shear Strength of Cohesive Soils by the Handheld Vane Shear Device*. West Conshohocken, PA, n.d.

[22] S. Austin, P. J. Robins, and C. Goodier. "Workability, Shear Strength and Build of Wet-Process Sprayed Mortars". In: Accessible via Semantic Scholar CorpusID: 55317708. 1999.

[23] N. Roussel and F. Cussigh. "Distinct-layer casting of SCC: the mechanical consequences of thixotropy". In: *Cement and Concrete Research* 38 (2008), pp. 624–632. DOI: 10.1016/j.cemconres.2007.09.023.

[24] S. N. Ahmed, F. Omran, and Kamal H. Khayat. “Portable vane test to assess structural buildup at rest of self-consolidating concrete”. In: *ACI Materials Journal* 108 (2011). DOI: 10.14359/51683466.

[25] L. Cadling and S. Odenstad. “Vane Borer: An Apparatus for Determining the Shear Strength of Clay Soils Directly in the Ground”. In: *Swedish Geotechnical Institute*. Vol. 2. 1950, p. 100.

[26] L. Demont et al. “Affordable inline structuration measurements of printable mortar with a pocket shear vane”. In: *Construction and Building Materials* 408 (2023), p. 133602. DOI: 10.1016/j.conbuildmat.2023.133602.

[27] R. Wolfs et al. “On-line and in-line quality assessment across all scale levels of 3D concrete printing”. In: *Cement and Concrete Research* 185 (2024), p. 107646. DOI: 10.1016/j.cemconres.2024.107646.

[28] O. Ivanova and V. Mechtcherine. “Possibilities and challenges of constant shear rate test for evaluation of structural build-up rate of cementitious materials”. In: *Cement and Concrete Research* 130 (Apr. 2020), p. 105974. DOI: 10.1016/j.cemconres.2020.105974.

[29] Schleibinger Geräte. *Viskomat XL*. pp. 174–175. n.d. URL: https://www.schleibinger.com/.

[30] V. N. Nerella et al. “Inline quantification of extrudability of cementitious materials for digital construction”. In: *Cement and Concrete Composites* 104 (2019), p. 103340. DOI: https://doi.org/10.1016/j.cemconcomp.2018.09.015.

[31] Arnaud Perrot et al. “Ram extrusion force for a frictional plastic material: model prediction and application to cement paste”. In: *Rheologica Acta* 45.4 (2006), pp. 457–467. DOI: 10.1007/s00397-005-0074-y.

[32] Nicolas Roussel and Philippe Coussot. ““Fifty-cent rheometer” for yield stress measurements: From slump to spreading flow”. In: *Journal of Rheology* 49.3 (2005), pp. 705–718. DOI: 10.1122/1.1879041.

[33] *ASTM C143-90 (1996): Standard Test Method for Slump of Hydraulic Cement Concrete*. West Conshohocken, PA, 1996.

[34] *ASTM C230/C230M-03: Standard Specification for Flow Table for Use in Tests of Hydraulic Cement*. West Conshohocken, PA, 2004.

[35] D. Lootens et al. “Yield stress during setting of cement pastes from penetration tests”. In: *Cement and Concrete Research* 39.5 (2009), pp. 401–408. DOI: 10.1016/j.cemconres.2009.01.012.

[36] L. Reiter et al. “Slow penetration for characterizing concrete for digital fabrication”. In: *Cement and Concrete Research* 157 (2022), p. 106802. DOI: 10.1016/j.cemconres.2022.106802.

[37] A. Szabo et al. “Mastering yield stress evolution and formwork friction for smart dynamic casting”. In: *Materials* 13.9 (2020). DOI: 10.3390/ma13092084.

[38] Derk H. Bos and Rob J. M. Wolfs. “Automated Visual Inspection of Near Nozzle Droplet Formation for Quality Control of Additive Manufacturing”. In: *Proceedings of the Third RILEM International Conference on Concrete and Digital Fabrication (Digital Concrete 2022)*. Ed. by Richard Buswell et al. Vol. 37. RILEM Bookseries. Presented at Digital Concrete 2022, RILEM Bookseries Vol. 37. Springer Nature Switzerland, 2022, pp. 453–459. DOI: 10.1007/978-3-031-06116-5_67. URL: https://doi.org/10.1007/978-3-031-06116-5_67.

[39] A.S.J. Suiker. “Mechanical performance of wall structures in 3D printing processes: Theory, design tools and experiments”. In: *International Journal of Mechanical Sciences* 137 (2018), pp. 145–170.

[40] A.S.J. Suiker et al. “Elastic buckling and plastic collapse during 3D concrete printing”. In: *Cement and Concrete Research* 135 (2020), p. 106016.

[41] R. Nicolas et al. “Assessing the fresh properties of printable cement-based materials: high potential tests for quality control”. In: *Cement and Concrete Research* 158 (2022), p. 106836. DOI: 10.1016/j.cemconres.2022.106836.

[42] A. H. Deetman and A. S. J. Suiker. “Characterization of early-age elastic–plastic properties of 3D printed materials using indentation testing”. In: *International Journal of Mechanical Sciences* (2025). Journal pre-proof (accepted manuscript). DOI: 10.1016/j.ijmecsci.2025.111141.

[43] R. J. M. Wolfs, F. P. Bos, and T. A. M. Salet. “Correlation between destructive compression tests and non-destructive ultrasonic measurements on early age 3D printed concrete”. In: *Construction and Building Materials* 181 (2018), pp. 447–454. DOI: 10.1016/j.conbuildmat.2018.06.060.

[44] J. Versteege, R. J. M. Wolfs, and T. A. M. Salet. “Data-driven additive manufacturing with concrete: Enhancing in-line sensory data with domain knowledge, Part I: Geometry”. In: *Automation in Construction* 172 (2025). Part I: Geometry, p. 106020. DOI: 10.1016/j.autcon.2025.106020. URL: https://doi.org/10.1016/j.autcon.2025.106020.

[45] Timothy Wangler et al. “Residence Time Distributions in Continuous Processing of Concrete”. In: *Rheology and Processing of Construction Materials*. Vol. 23. RILEM Bookseries. Springer, 2019, pp. 448–456. DOI: 10.1007/978-3-030-22566-7_54.

[46] Octave Levenspiel. *Chemical Reaction Engineering*. 3rd ed. New York: John Wiley & Sons, 1999, p. 54. DOI: 10.1021/ie990488g.

[47] J Versteege, RJM Wolfs, and TAM Salet. “Data-driven additive manufacturing with concrete: Enhancing in-line sensory data with domain knowledge, Part II: Moisture and heat”. In: *Automation in Construction* 177 (2025), p. 106327.

[48] Freek Bos et al. “Mechanical properties of 3D printed concrete: a RILEM TC 304-ADC interlaboratory study — approach and main results”. In: *Materials and Structures* 58.5 (July 2025). Peer-reviewed article, p. 183. DOI: 10.1617/s11527-025-02686-x.

[49] Freek Bos et al. *RILEM TC 304-ADC ILS-mech Study Plan*. Study Plan. Forschungsdaten (research data). 2023. DOI: 10.14459/2023mp1705940. URL: https://doi.org/10.14459/2023mp1705940.

[50] Arjen Deetman et al. “A database framework for 3D concrete printing”. In: *Results in Engineering* (2025). Journal pre-proof (open access, CC BY-NC-ND 4.0). DOI: 10.1016/j.rineng.2025.108669.

[51] COBOD International. *BOD2 Modular 3D Construction Printer – Technical Specifications*. https://www.cobod.com. Accessed 2025-03-01. 2023.

[52] Tallinn University of Applied Sciences (TTK). *Betooni 3D Printimise Labor*. https://www.tktk.ee/ettevotjale/laborid/ehitusinstituut/betooni-3d-printimise-labor/. Accessed: 2025-12-09. n.d.

[53] Hyperion Robotics. *Hyperion Robotics*. https://www.hyperionrobotics.com/. Accessed: 2025-12-09. n.d.

[54] Weber Saint-Gobain. *Weber 3D Printing*. https://www.3d.weber/nl. Accessed: 2025-12-09. n.d.
[55] Vertico B.V. *Vertico — 3D Concrete Printing*. https://www.vertico.com/. Accessed: 2025-12-09. n.d.
[56] COBOD International A/S. *COBOD — Construction 3D Printing*. https://cobod.com/. Accessed: 2025-12-09. n.d.
[57] ETH Zürich, Institute of Technology in Architecture (ITA). *Robotic Fabrication Laboratory (RFL)*. https://ita.arch.ethz.ch/archteclab/rfl.html. Accessed: 2025-12-09. n.d.
[58] M. Tho and N. Thinh. "Cable-driven parallel robot for large-scale concrete printing". In: *Proceedings of the 38th ISARC Conference*. 2021, pp. 1201–1208. DOI: 10.22260/ISARC2021/0165.
[59] P. Bosscher et al. "Cable-suspended robotic contour crafting system". In: *Automation in Construction*. Vol. 17. 2007, pp. 45–55. DOI: 10.1016/j.autcon.2007.02.002.
[60] Constructions-3D. *Mobile 3D Concrete Printing Systems – Field Deployment Report*. https://www.constructions-3d.com. Accessed 2025-02-15. 2024.
[61] Rhino 3D. *Learn to use Rhino: Grasshopper Tutorials*. https://www.rhino3d.com/learn. Accessed: 2025-12-04. 2025.
[62] *food4Rhino — Apps for Rhinoceros 3D and Grasshopper*. https://www.food4rhino.com/. Accessed: 2025-12-04.
[63] McNeel. *Grasshopper Learning Resources*. Accessed: 2025-12-29. 2024. URL: https://www.rhino3d.com/learn/?query=kind:%20grasshopper&modal=null.
[64] Arjen Deetman et al. *Salad Slicer: An open-source slicer toolkit for 3D concrete printing*. 2023. DOI: 10.5281/zenodo.7818240. URL: https://doi.org/10.5281/zenodo.7818240.
[65] Arjen Deetman et al. *Robot Components: Intuitive Robot Programming for ABB Robots inside of Rhinoceros Grasshopper*. 2025. DOI: 10.5281/zenodo.15207230. URL: https://doi.org/10.5281/zenodo.15207230.
[66] Shaun Wu, Karamba3D. *Buckling Simulation for 3D Concrete Printing*. https://karamba3d.com/research/buckling-simulation-3d-concrete-printing/. Accessed: December 29, 2025.
[67] T.A.M. Salet et al. "Design of a 3D printed concrete bridge by testing". In: *Virtual and Physical Prototyping* 13.3 (2018), pp. 222–236. DOI: 10.1080/17452759.2018.1476064.
[68] Ana Anton et al. "Tor Alva: A 3D Concrete Printed Tower". In: *Fabricate 2024: Creating Resourceful Futures*. Ed. by Phil Ayres et al. Accessed via JSTOR. UCL Press, 2024, pp. 252–259. URL: https://www.jstor.org/stable/jj.11374766.35.
[69] James Dobrzanski et al. "From digital crafting to digital manufacturing: automated production using hybrid 3D concrete printing". In: *Journal of Building Engineering* 108 (Aug. 2025). Open Access under CC BY license, p. 112640. DOI: 10.1016/j.jobe.2025.112640. URL: https://doi.org/10.1016/j.jobe.2025.112640.
[70] Richard Buswell, Rasti Bartek, and Vera Sehlstedt. *The Story of The Canopy*. Originally written for and published in Concrete Magazine, 6 July 2025. Cun-

dall. 2025. URL: https://www.cundall.com/ideas/blog/the-story-of-the-canopy (visited on 07/06/2025).

[71] Z.Y. Ahmed et al. “A framework for large-scale structural applications of 3D printed concrete: the case of a 29 m bridge in the Netherlands”. In: *Open Conference Proceedings*. Vol. 1. 2022, pp. 5–19.

[72] R. Wolfs, D. Bos, and T. Salet. “Lessons learned of Project Milestone: The first 3D printed concrete house in the Netherlands”. In: *Materials Today: Proceedings* (2023).

[73] H. Kloft et al. “Interaction of reinforcement, process, and form in Digital Fabrication with Concrete”. In: *Cement and Concrete Research* 186 (2024), p. 107640. DOI: 10.1016/j.cemconres.2024.107640.

[74] V. Mechtcherine et al. “Integrating reinforcement in digital fabrication with concrete: A review and classification framework”. In: *Cement and Concrete Composites* 119 (2021), p. 103964.

[75] T. Marchment and J. Sanjayan. “Bond properties of reinforcing bar penetrations in 3D concrete printing”. In: *Automation in Construction* 120 (2020), p. 103394.

[76] F.P. Bos et al. “Experimental exploration of metal cable as reinforcement in 3D printed concrete”. In: *Materials* 10.11 (2017), p. 1314.

[77] T. Wangler et al. “Digital concrete: a review”. In: *Cement and Concrete Research* 123 (2019), p. 105780.

[78] Z.Y. Ahmed et al. “On-demand additive manufacturing of functionally graded concrete”. In: *Virtual and Physical Prototyping* 15.2 (2020), pp. 194–210.

[79] G. De Schutter et al. “Vision of 3D printing with concrete—technical, economic and environmental potentials”. In: *Cement and Concrete Research* 112 (2018), pp. 25–36.

[80] Z. Wu, A.M. Memari, and J.P. Duarte. “State of the art review of reinforcement strategies and technologies for 3D printing of concrete”. In: *Energies* 15.1 (2022), p. 360.

[81] D. Asprone et al. “Rethinking reinforcement for digital fabrication with concrete”. In: *Cement and Concrete Research* 112 (2018), pp. 111–121.

[82] Apis Cor. *3D Printed Homes*. https://www.apis-cor.com/. 2020.

[83] WinSun. *WinSun 3D Printing Construction*. http://www.winsun3d.com/. 2020.

[84] F. Bos et al. “Large scale testing of digitally fabricated concrete (DFC) elements”. In: *RILEM Bookseries*. Springer, 2019, pp. 129–147. DOI: 10.1007/978-3-319-99519-9_12.

[85] V. Mechtcherine et al. “Integrating reinforcement in digital fabrication with concrete: A review and classification framework”. In: *Cement and Concrete Composites* 119 (2021), p. 103964. DOI: 10.1016/j.cemconcomp.2021.103964.

[86] Alejandro Giraldo Soto et al. “Fully load-bearing reinforced 3D printed concrete and its application in Tor Alva, the world-tallest 3D printed concrete tower”. In: *Hormigón y Acero*. Vol. 76. 1. Creative Commons Attribution-NonCommercial-NoDerivatives 4.0 International. June 2025. DOI: 10.3929/ethz-b-000745428. URL: https://doi.org/10.3929/ethz-b-000745428.

[87] G. Vantyghem et al. “3D printing of a post-tensioned concrete girder designed by topology optimization”. In: *Automation in Construction* 112 (2020), p. 103084. DOI: 10.1016/j.autcon.2020.103084.

[88] D. Asprone et al. “3D printing of reinforced concrete elements: Technology and design approach”. In: *Construction and Building Materials* 165 (2018), pp. 218–231. DOI: 10.1016/j.conbuildmat.2018.01.018.

[89] Vertico. *Printing on Frame*. https://www.vertico.com/projects/printing-on-frame. Accessed: 2025-12-04. 2025.

[90] *Chinese construction company 3D prints an entire two-story house on-site in 45 days*. https://3dprint.com/138664/huashang-tengda-3d-print-house/. Accessed 16-Nov-2020.

[91] N. Hack et al. “Mesh Mould: an on-site, robotically fabricated, functional formwork”. In: *Robotic Fabrication in Architecture, Art and Design 2018*. Springer, 2017, pp. 728–737. DOI: 10.1007/978-3-319-92294-2.

[92] Norman Peter Hack. “Mesh Mould: A robotically fabricated structural stay-in-place formwork system”. DISS. ETH NO. 25068. Doctor of Sciences (Dr. sc. ETH Zurich). Zurich, Switzerland: ETH Zurich, 2018.

[93] Lukas Johannes Maximilian Gebhard. “Reinforcement Strategies for Digital Fabrication with Concrete”. Doctor of Sciences (Dr. sc. ETH Zurich). Zurich, Switzerland: ETH Zurich, 2023.

[94] F. P. Bos et al. “Experimental exploration of metal cable as reinforcement in 3D printed concrete”. In: *Materials* 10.11 (2017), p. 1314. DOI: 10.3390/ma10111314.

[95] F. P. Bos et al. “Bond of reinforcement cable in 3D printed concrete”. In: *RILEM Bookseries*. Springer, 2020, pp. 584–600. DOI: 10.1007/978-3-030-49916-7_60.

[96] V. Mechtcherine et al. “Mineral-impregnated carbon fiber composites as novel reinforcement for concrete construction”. In: *Automation in Construction* 110 (2020), p. 103002. DOI: 10.1016/j.autcon.2019.103002.

[97] T. Neef, S. Müller, and V. Mechtcherine. “3D-Druck mit Carbonbeton: Technologie und erste Untersuchungsergebnisse”. In: *Beton- und Stahlbetonbau* 115 (2020), pp. 943–951. DOI: 10.1002/best.202000069.

[98] Léo Demont et al. “Flow-based pultrusion of continuous fibers for cement-based composite material and additive manufacturing: rheological and technological requirements”. In: *Composite Structures* 262 (2021), p. 113564. DOI: 10.1016/j.compstruct.2020.113564.

[99] 3Druck.com Editorial Team. *V2 Vesta Beton-3D-Drucker baut kleines Haus*. Accessed: 13 November 2020. n.d. URL: https://3druck.com/druckerundprodukte/v2-vesta-beton-3d-drucker-baut-kleines-haus-2846225/.

[100] B. Baz et al. “Mechanical assessment of concrete–steel bonding in 3D printed elements”. In: *Construction and Building Materials* 256 (2020), p. 119457. DOI: 10.1016/j.conbuildmat.2020.119457.

[101] A. Perrot et al. “Nailing of layers: a promising way to reinforce concrete 3D printing structures”. In: *Materials* 13.7 (2020), p. 1518. DOI: 10.3390/ma13071518.

[102] T. Marchment and J. Sanjayan. “Bond properties of reinforcing bar penetrations in 3D concrete printing”. In: *Automation in Construction* 120 (2020), p. 103394. DOI: 10.1016/j.autcon.2020.103394.

[103] N. Freund, I. Dressler, and D. Lowke. “Studying the bond properties of vertical integrated short reinforcement in the shotcrete 3D printing process”. In: *RILEM Bookseries*. Springer, 2020, pp. 612–621. DOI: 10.1007/978-3-030-49916-7_62.

[104] M. Hambach and D. Volkmer. “Properties of 3D-printed fiber-reinforced Portland cement paste”. In: *Cement and Concrete Composites* 79 (2017), pp. 62–70. DOI: 10.1016/j.cemconcomp.2017.02.001.

[105] F.P. Bos, E. Bosco, and T.A.M. Salet. “Ductility of 3D printed concrete reinforced with short straight steel fibers”. In: *Virtual and Physical Prototyping* 14.2 (2019), pp. 160–174. DOI: 10.1080/17452759.2018.1548069.

[106] A.R. Arunothayan et al. “Development of 3D-printable ultra-high performance fiber-reinforced concrete for digital construction”. In: *Construction and Building Materials* 257 (2020), p. 119546. DOI: 10.1016/j.conbuildmat.2020.119546.

[107] H. Ogura, V. Nerella, and V. Mechtcherine. “Developing and testing of strain-hardening cement-based composites (SHCC) in the context of 3D-printing”. In: *Materials* 11.8 (2018), p. 1375. DOI: 10.3390/ma11081375.

[108] V.C. Li et al. “On the emergence of 3D printable engineered, strain- hardening cementitious composites (ECC/SHCC)”. In: *Cement and Concrete Research* 132 (2020), p. 106038. DOI: 10.1016/j.cemconres.2020.106038.